Doctoral Dissertation
Doctoral Program in Metrology (36^{th}cycle)

Beating Abbe's diffraction limit in optical microscopy via non classical photon statistics and structured illumination

By

Fabio Picariello

******

Supervisor(s):
Dr. Marco Genovese, Supervisor
Dr. Ivano Ruo Berchera, Co-Supervisor

Doctoral Examination Committee:
Prof. Milena D'Angelo, Università degli Studi di Bari
Prof. Stefano Olivares, Università degli Studi di Milano
Prof. Alessia Allevi, Università degli Studi dell'Insubria
Prof. Francesco Raffa, Politecnico di Torino
Dr. Marco Gramegna, Primo Ricercatore, INRIM

Politecnico di Torino
2024

Declaration

I hereby declare that, the contents and organization of this dissertation constitute my own original work and does not compromise in any way the rights of third parties, including those relating to the security of personal data.

Fabio Picariello
2024

* This dissertation is presented in partial fulfillment of the requirements for **Ph.D. degree** in the Graduate School of Politecnico di Torino (ScuDo).

I would like to dedicate this thesis to my family and friends

Acknowledgements

I would like to thank my supervisor, Dr. Marco Genovese, for giving me the opportunity to perform my research in such an inspiring environment, and to my Co-Supervisor, Dr. Ivano Ruo Berchera, whose advice and assistance were fundamental in pursuing my research goals. I am also grateful to the entire Quantum Optics group at INRiM for all the help and advice I received during my doctoral studies.

I would also like to express my gratitude to the solid-state group of the Physics Department at the University of Turin for their collaboration in the realization of the samples and experimental setup.

Lastly, I would like to thank all those who supported me during this journey, helping me to persevere even in the most challenging moments, and constantly reminding me that I could achieve this goal.

Abstract

Roughly two decades ago, it was demonstrated that the resolution limit posed by diffraction can be overcome, a breakthrough for science and medical research acknowledged by the Nobel Prize for chemistry in 2014 [1, 2, 3]. Since then, super-resolution optical far-field imaging has undergone tremendous evolution, resulting in the development of a wide range of methods especially in fluorescence microscopy. However, most of them require high optical power and are not suited for biological applications [1, 4]. A specific branch of methods that is also biocompatible employs the usage of emitters with either super-Poissonian bunched-light emission due to statistical fluctuations or sub-Poissonian antibunched-light, statistics typical of single photon sources. The ability of these techniques to beat the classical diffraction limit has been demonstrated both in wide-field [5, 6] and confocal microscopy [7], with scaling in the resolution of $\sqrt{j}$ where j is the measured correlation order. Another family of methods that have been demonstrated to achieve super-resolution relies on boosting the frequency information on the image plane. Normally, the total amount of frequency information that can be retrieved by an imaging setup is d_{Abbe}^{-1} where d_{Abbe} is the minimum resolvable distance in classic imaging. The Structured Illumination Microscopy (SIM) technique can overcome this limit by exploiting a sinusoidal light pattern to illuminate the sample, achieving twice the frequency information than a classical imaging setup [8]. The goal of this work is to perform a detailed study on super-resolution obtained by non-Poissonian statistics combining it with the boost on the frequency domain provided by the structured illumination microscopy, providing an overall super-resolution scaling factor of $\sqrt{j}+j$.

Introduction

Precise measurements have always been essential for gaining knowledge and progress in science and technology. However, as technology advanced, the constraints of traditional measuring methods became apparent. Classical-based approaches have inherent accuracy bounds due to fundamental limits such as shot noise and the uncertainty principle.

The increasing demand for high-precision measurements in various scientific and technical fields has led to *quantum metrology* becoming a focus of study and innovation. Quantum metrology utilizes specific properties of states and measurements to enhance measurement accuracy beyond the limitations of classical methods.

An important emerging topic at the forefront of quantum metrology is *quantum imaging*, which utilizes the properties of quantum optical systems to enhance various aspects of imaging, providing unparalleled capabilities in resolution, sensitivity, and information retrieval.

A significant advantage of quantum imaging resides in its capacity for sub-shot-noise sensitivity. In particular, by using quantum phenomena such as squeezing and quantum correlations, quantum imaging approaches may improve the Signal-to-Noise Ratio (SNR) in the estimation of optical parameters (phase, transmittance, polarization) by reducing the effect of the shot-noise [9, 10, 11]. This is especially relevant when reducing the photon dose on the sample is demanded to avoid photodamage or alteration of the processes under study. Furthermore, quantum-enhanced sensing represents a frontier where quantum imaging's capability to refine sensing precision is unparalleled. Quantum properties of photon sources, like Nitrogen-Vacancy centers in diamond (described in Section 1.2.2) can be used as nanoscale sensors for temperature, electric and magnetic fields, and sample's strain measurements, due to variation in their luminescence properties [12, 13, 14, 15].

Another important property of quantum imaging protocols is their robustness in environments with high external noise. An example is given by the quantum illumination scheme, where the correlation between two beams of a bipartite non-classical state of light is used to detect target hidden in a noisy thermal background [16, 17]. Lastly, quantum imaging methods have the potential to go beyond the diffraction limit imposed by traditional optics. Improving the spatial resolution in imaging is an important tool in biological and biomedical research

nowadays, however, spatial resolution was considered to be fixed for long time from the fundamental limitation imposed by the numerical aperture of the objective and the wavelength of light, as noted by Ernst Abbe [18].

Despite its ability to achieve orders of magnitude better resolution, electron microscopy has historically been hampered by challenges in sample preparation, labeling, and identifying particular molecules and structures, as well as a relatively low throughput in optics. As a consequence, scientists looked into methods to overcome the resolution barrier and bridge the gap between light and electron microscopy. Early studies were limited to near-field scanning technologies, which had extremely specialized and limited use in biology. The first fundamental principles for exceeding the optical diffraction limit in far-field fluorescence microscopy were proposed in the early 1990s with the proposal of STED [1], Structured Illumination Microscopy (SIM) [8] and Single Molecule Localization Microscopy (SMLM) [19]. Following the creation of the first super-resolution methods, subsequent improvements were mostly driven by the biologists' requests for super-resolution techniques that allow live cell imaging and require low levels of light to prevent photodamage effects.

Some of the super-resolution techniques suitable for biological applications, rely on the analysis of high-order correlations of non-Poissonian light sources [5, 6, 7]. The analysis of high-order moments offers a powerful approach for achieving super-resolution. Nevertheless, the substantial volume of data and the large amount of time required to compute high-order moments pose challenges when it comes to practical implementation. In recent years, it has been shown that it is feasible to integrate non-Poissonian super-resolution methods with Structured Illumination Microscopy. This integration offers the advantage of achieving a substantial enhancement in super-resolution by focusing on the analysis of a limited number of high-order moments. The practical implementation of the technique exploiting super-Poissonian light sources, known as Super-resolution Optical Fluctuation Imaging - Structured Illumination Microscopy (SOFI-SIM) [20], has been demonstrated. However, the sub-Poissonian counterpart, known as Structured Illumination Quantum Correlation Microscopy (SIQCM) [21], has only been theoretically proposed.

Both SOFI-SIM and SIQCM provide the same scaling in super-resolution of $\sqrt{j}+j$, where j is highest central moment assessed of the detected photon distribution, however, a limitation of SOFI-SIM comes from a large dynamic range due to different fluctuations in the brightness of blinking emitters [22]. On the other hand, SIQCM offers the benefit of operating effectively under low-light conditions and preserving a limited dynamic range.

This thesis aims to provide a comprehensive investigation into super-resolution techniques achieved through non-Poissonian statistics by elaborating a comprehensive quantum model valid for any non-Poissonian photon sources and in every illumination regime. The super-

Poissonian photon statistics super-resolution model proposed in the literature [6] is based on a semi-classical approach that overlooks quantum fluctuations, thereby significantly limiting resolution enhancement in low light conditions. Specifically, in low light scenarios, the quantization of light into photons becomes prominent, and only a fully quantum description can achieve optimal performance in optical imaging. Conversely, the sub-Poissonian super-resolution method reported in the literature relies on a mathematical model valid only with single-photon emitters that emit a single photon [7]. Therefore, a comprehensive quantum description of a generalized non-Poissonian photon statistics super-resolution method is lacking. Developing such a model could greatly impact the advancement of super-resolution quantum microscopes, potentially revolutionizing applications that require low power combined with high SNR and high resolution.

Furthermore, this thesis presents an extensive analysis of the SNR in the context of both sub and super-Poissonian super-resolution methods. The aim is to provide a guide for selecting the most effective detection schemes, photon sources, and experimental parameters, in order to reduce both the total data volume and acquisition time necessary for achieving non-Poissonian super-resolved images. Additionally, the thesis explores the integration of non-Poissonian super-resolution techniques with SIM, focusing on extremely low light levels.

The thesis will be divided into the following chapters:

Chapter 1 gives an insight into single photon emitters, focusing on their emission statistics and covering some examples of bio-compatible emitters used in fluorescence optical microscopy.

Chapter 2 explores the main limits of classical optical imaging and presents bio-compatible super-resolution techniques analyzed in the framework of the thesis.

Chapter 3 gives an insight into detectors used in fluorescence imaging.

Chapter 4 details the experimental setups implemented for the research conducted in this Ph.D. study.

Chapter 5 introduces a generalized quantum model for super-resolution developed in the framework of the Ph.D. and compare its performance with classical analysis reported in the literature.

Chapter 6 presents a detailed study of the SNR of sub and super-Poissonian emitters considering the most common detection schemes employed in biological optical imaging.

Chapter 7 reports simulations and experimental results over the combination of our generalized quantum model for super-resolution and Structured Illumination Microscopy.

Table of contents

List of figures

List of tables

Chapter 1

Single photon sources for quantum imaging

The experimental realization of several quantum imaging protocols relies on the special properties of the single photon emitters. A single photon emitter is a device or system that creates and emits individual photons with well-defined quantum features, one at a time. It is intended to generate photons characterized by specific properties such as wavelength, polarization, and temporal profile.

A single photon emission can be triggered by an optical [23][24] or electrical [25][26] excitation. These emitters exploit distinct quantum processes, such as quantum confinement and energy level quantization, allowing them to emit photons one-by-one with well-defined quantum features such as high purity, and high indistinguishability, properties useful for the encoding, manipulation, and control of quantum information.

In order to characterize the anti-bunching statistics of a photon source, i.e. the emission of individual photons, the second-order correlation function $g^{(2)}(\tau)$ is commonly used as a figure of merit. In the next sections, we will introduce the mathematical definition of the $g^{(2)}(\tau)$ as well as a description of solid-state single photon emitters typically employed in fluorescence optical imaging.

1.1 Second-order correlation function

The second-order correlation function is a statistical measure used to describe the correlation or relationship between two events or observations within a given system. It quantifies how likely it is for two photon-detection events to occur simultaneously compared to what would be expected if the events were statistically independent [27].

This function can be used to describe the statistical properties of an electromagnetic field in the context of classical and quantum optics. Specifically, it provides information about the correlation between the electric field values at two different instants t and $t+\tau$ [28]:

$$g^{(2)}(\tau) = \frac{\langle \hat{E}^\dagger(t)\hat{E}^\dagger(t+\tau)\hat{E}(t)\hat{E}(t+\tau)\rangle}{\langle \hat{E}^\dagger(t)\hat{E}(t)\rangle^2}. \tag{1.1}$$

The operator representing the electric field can be delineated through the decomposition into modes as follows:

$$\hat{E}(t) = \int_{-\infty}^{\infty} \alpha_k \hat{a}_k e^{ikvt} dk, \tag{1.2}$$

$$\hat{E}^\dagger(t) = \int_{-\infty}^{\infty} \alpha_k^* \hat{a}_k^\dagger e^{-ikvt} dk, \tag{1.3}$$

where v is the speed of light in the medium in which the field propagates, α_k are coefficients that reflect the modal structure and normalization, and $\hat{a}_k$ and $\hat{a}_k^\dagger$ are the annihilation and creation operators for a specific mode k, respectively. These operators follow the commutation rule: $[\hat{a}_k, \hat{a}_{k'}^\dagger] = \delta(k-k')$.

The photon statistics of the emitter can be determined by examining the second-order correlation function at zero time delay ($\tau = 0$). For simplicity, let's focus on a single mode field and introduce the number operator $\hat{n} := \hat{a}^\dagger\hat{a}$. With this definition, Equation 1.1 simplifies to:

$$g^{(2)}(0) = \frac{\langle \hat{a}^\dagger\hat{a}^\dagger\hat{a}\hat{a}\rangle}{\langle \hat{n}\rangle^2} = \frac{\langle \hat{a}^\dagger(\hat{a}\hat{a}^\dagger - 1)\hat{a}\rangle}{\langle \hat{n}\rangle^2} = \frac{\langle \hat{n}^2 - \hat{n}\rangle}{\langle \hat{n}\rangle^2}. \tag{1.4}$$

Another way to write Equation 1.4 is in terms of the statistical variance (or second-order central moment) of the number of photons emitted by the source: $\mu_2 = \langle \hat{n}^2\rangle - \langle \hat{n}\rangle^2$, leading to:

$$g^{(2)}(0) = 1 + \frac{1}{\langle \hat{n}\rangle^2}(\mu_2 - \langle \hat{n}\rangle). \tag{1.5}$$

In the context of this study, the relationship between the second-order correlation function and photon statistics is explored using the expression from Equation 1.5 [29].

1. **Poissonian statistics**
   For a light source emitting photons with a Poissonian distribution, such as a laser, the variance μ_2 is equivalent to the mean value of the distribution $\langle \hat{n}\rangle$, resulting in $\mathbf{g^{(2)}(0) = 1}$.

2. **Thermal statistics**
   In the case of thermal light, like sunlight, the variance is given by $\mu_2 = \langle \hat{n}\rangle + \langle \hat{n}\rangle^2$, leading to a correlation function of $\mathbf{g^{(2)}(0) = 2}$.

3. **Single photon emitters**
   An ideal single photon emitter, defined by emitting exactly one photon per excitation cycle, results in a null variance. In this specific scenario, the correlation function at zero time delay is $\mathbf{g^{(2)}(0) = 0}$.

It is observed that for a Fock state $|n\rangle$ (representing a state with precisely n photons), the second-order correlation function is: $g^{(2)}(0) = 1 - 1/\langle\hat{n}\rangle$. When examining light emitted simultaneously from multiple single photon emitters, this relationship provides insights into the number of emitters contributing to the signal. Detecting light from two ideal single photon emitters results in $g^{(2)}(0) = 1/2$.

As the number of single photon emitters becomes very large, the photon statistics approach a Poissonian distribution, $g^{(2)}(0) \sim 1$.

The second-order correlation function is particularly informative in proximity to zero time delay. Regardless of the light source's nature, for $t \gg \tau$, it can be observed that $g^{(2)}(\infty) \sim 1$.

A schematic representation of $g^{(2)}(\tau)$ is presented in Figure 1.1.

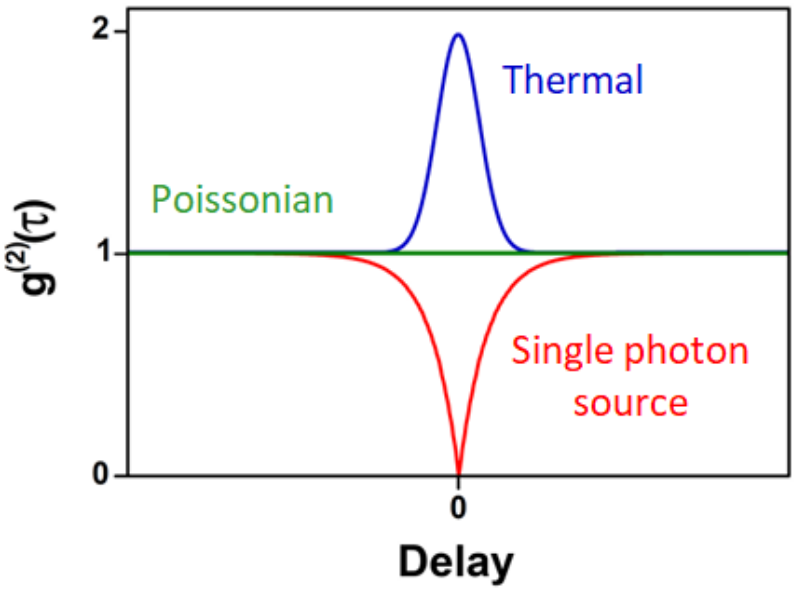

Figure 1.1: $g^{(2)}(\tau)$ *for Poissonian (green), Thermal (blue), and Single Photon Source (red) [29]. The temporal width of* $g^{(2)}(\tau)$ *is related to the temporal coherence of the source, which in turn depends on its modal structure (*α_k *in Equation 1.2). If the emitter predominantly emits in a single mode, the temporal width will be longer (indicating higher coherence), while a multimodal source will show a shorter temporal width.*

The investigation of correlations between two detection events can be broadened to encompass higher orders. Specifically, the formula for a correlation function of photon events of any given order can be articulated using the photon number operator $\hat{n}$ as follows:

$$g^{(j)}(\tau_1 = 0, \tau_2 = 0, \ldots, \tau_{j-1} = 0) = \frac{\left\langle \prod_{i=1}^{j-1} \hat{n}(\hat{n} - i) \right\rangle}{\langle \hat{n} \rangle^j}. \tag{1.6}$$

As outlined in Section 2.2, correlation functions of higher orders are instrumental in enhancing super-resolution imaging techniques. Specifically, for systems utilizing single photon emitters, these higher-order correlation functions also serve to determine the quantity of emitters contributing to the observed intensity signal. In particular, as highlighted earlier, the second-order correlation function for two emitters at $\tau = 0$ is given by $g^{(2)}(0) = 1/2$. Conversely, the third-order correlation function, which corresponds to the likelihood of simultaneous three-photon detection events, is $g^{(3)}(0,0) = 0$. This principle can be generalized to any number of emitters: to determine the number of contributing emitters, one simply needs to evaluate the correlation functions at zero time delay until they all equal 0; for a system comprising j single photon emitters, every correlation function of an order higher than $j+1$ will be identically null.

1.2 Bio-compatible single photon emitters

Optical microscopy is a foundational and invaluable tool in both biology and medicine due to its ability to visualize and analyze biological structures and processes at the cellular and molecular levels. Its usefulness stems from several key factors such as real-time observation of dynamic processes within living cells and organisms, its non-invasive nature, and its ability to enhance specificity and selectivity by using fluorescent labels and dyes. The next sections will present biocompatible photon sources, characterized by non-Poissonian photon statistics, commonly used in fluorescence optical imaging.

1.2.1 Quantum dots

Quantum dots are nanoscale semiconductor structures with unique quantum features owing to their tiny size and constrained electronic states. They are sometimes referred to as artificial atoms because, like atoms, they have distinct energy levels. The characteristics of quantum dots may be carefully tailored by adjusting their size, shape, and composition during synthesis [30, 31, 32, 33].

Quantum dots are often formed of semiconducting materials such as cadmium selenide (CdSe), lead sulfide (PbS), or indium arsenide (InAs). Their small size, measured in nanometers,

confines electrons and holes within their borders. This confinement produces separate energy levels, giving birth to unique optical and electrical features (see Figure 1.2). In particular, the energy levels of a cubic quantum dot with length L will be:

$$E_{n,o,p} = \frac{h\pi}{4m^* L^2}(n^2 + o^2 + p^2), \tag{1.7}$$

with $n, o, p \in \mathbb{N}$ and m^* referring to the isotropic effective mass of electrons and holes [34].

One of the most notable characteristics of quantum dots is their size-dependent bandgap, as represented in Figure 1.2. As the size of a quantum dot drops, so does its bandgap energy, resulting in an adjustable range of light absorption and emission [33]. Because of their unique properties, quantum dots have found uses in a variety of sectors, including optoelectronics, display technologies, biological imaging, and quantum information technology [35].

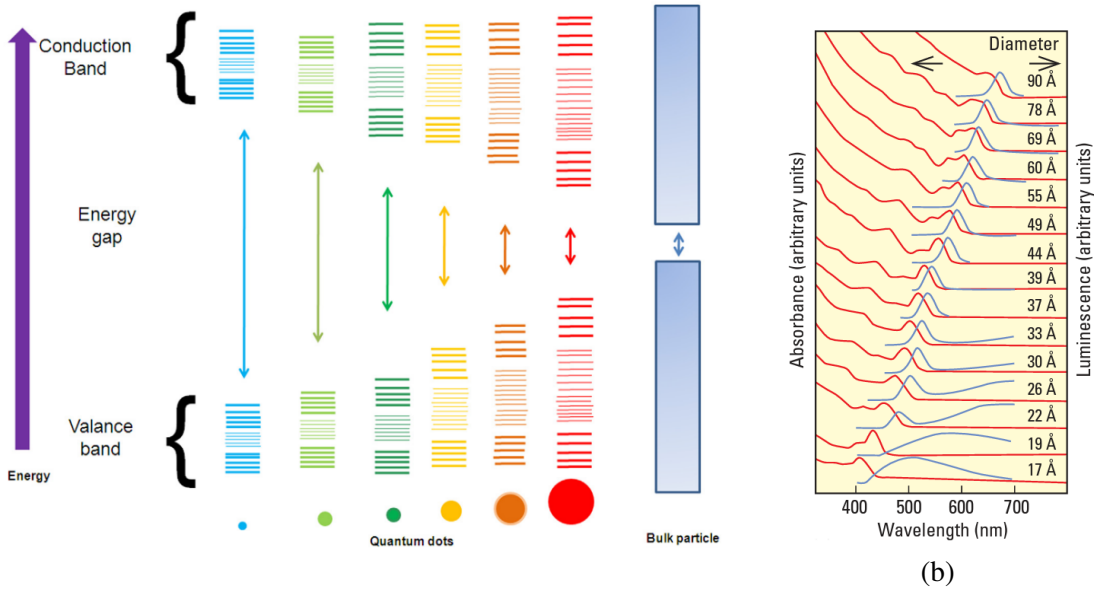

(a) (b)

Figure 1.2: *Energetic properties and optical responses of size-tunable quantum dots. Panel (a): schematic representation of energetic levels in size-tunable quantum dots [35]. Panel (b): absorption (red) and photoluminescence (blue) spectra as a function of quantum dots diameter [33].*

A peculiar characteristic of quantum dots is their occasional switching on and off of their fluorescence or luminescence, phenomena known as blinking [36, 37, 38] and reported in Figure 1.3. A complicated interaction of numerous elements causes blinking in quantum dots. The existence of surface imperfections or traps inside the quantum dot structure is one of the primary reasons. These flaws have the ability to capture and release charge carriers (electrons and holes) involved in the light-emitting process. When a trapped carrier is released,

it recombines with its counterpart, emitting a photon. The observed fluorescence is the result of this recombination event.

However, after the carrier is released and recombined, it may get trapped again, briefly preventing additional recombination processes and causing the quantum dot to look dark or "Off" at these times. This carrier trapping and release may occur at random and stochastically, resulting in the intermittent blinking characteristic of quantum dots.

Other elements that may impact blinking include the quantum dot's size and composition, as well as the surrounding environment. Surface ligands or molecules, for example, may influence charge carrier dynamics, resulting in changes in blinking behavior.

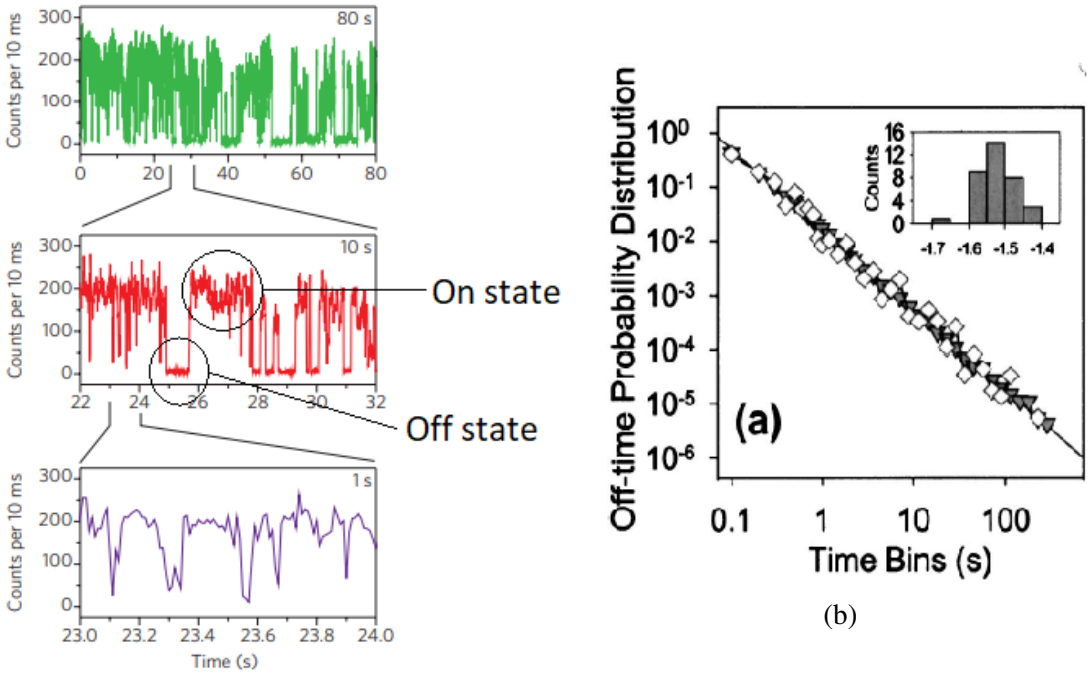

Figure 1.3: *Dynamic behavior and statistical analysis of quantum dot blinking. Panel (a): time trace of a single quantum dot blinking over a sequence of three expanded timescales [36]. Panel (b): normalized off-time probability distribution for CdSe quantum dots [37].*

Quantum dots, due to their ability to emit single photons can be exploited in sub-Poissonian super-resolution techniques [5]. However, their peculiar blinking phenomena can be used to perform super-Poissonian super-resolution methods, as discussed in Section 2.2.2.

1.2.2 Crystal defects

The presence of impurities in the lattice is a natural occurrence in every crystalline solid, as it is energetically favorable for the system to introduce point defects during the formation process, such as vacancies and substitutional defects, rather than creating an extremely ordered crystalline structure [34]. Defects can also be introduced after the synthesis process, using for instance, ion implantation. Irradiating the material with ions having energies ranging from MeV to keV, it is possible to introduce both impurities and create interstitial defects due to the damage to the crystalline matrix [39, 40, 41].

Some defects give rise to discrete levels or sub-bands within the material's energy gap, as schematically illustrated in Figure 1.4.

Typically, these substructures are generated in semiconductors with high energy gaps, such as diamond [39, 40, 42, 43] ($E_{\text{gap}} = 5.5\,\text{eV}$) or silicon carbide [44, 45] ($E_{\text{gap}} = 2.86\,\text{eV}$), but color centers have been observed in low-energy gap semiconductors, such as silicon [46, 47, 48] ($E_{\text{gap}} = 1.12\,\text{eV}$). The chemical species and structures that give rise to these levels are still under study, although different ones have been observed, particularly within diamond.

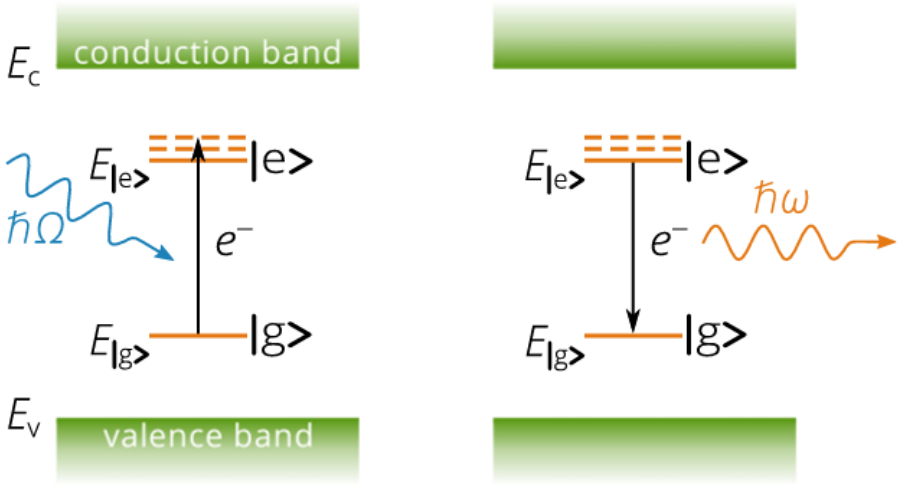

Figure 1.4: *Schematic representation of photoluminescence in high band gap semiconductor [49].*

Diamond is a biocompatible material commonly used for biological applications due to it reduced toxicity and its robustness to harsh biological circumstances as high temperatures and acidic environments [42, 50, 51, 52]. One of the most common optically active defect in diamond, due to its peculiar spin property and natural abundance, is the Nitrogen-Vacancy (NV) color center, which find an important role in imaging and sensing [53, 54, 55]. The electronic structure of the NV center is defined by six electrons: two from the nitrogen atom and three from the carbon atoms adjacent to the vacancy [56]. An additional electron is acquired from the

lattice, usually from nitrogen donors, leading to a predominant negative charge state NV^-. This structure results in the electron density primarily being distributed in a plane perpendicular to the NV axis, concentrating around the carbon atoms and the vacancy site. The NV center exists in multiple charge states, but NV^- is the primary focus of research due to its magneto-optical activity, which is not present in the neutral NV^0 or positively charged NV^+ states [57]. NV center's optical features are represented by a simplified energy-level model, illustrating three key electronic states: the ground state ($|g\rangle$), an excited state ($|e\rangle$), and a metastable singlet state ($|s\rangle$). These states, mainly comprising spin triplets, are responsible for the NV center's emission in the 630 nm to 800 nm range, predominantly appearing as vibrational sidebands after the 638 nm zero-phonon line, with a spin state-dependent quantum yield, defined as the ratio of the number of photons emitted to those absorbed, of approximately $70-80\%$ [58].

In terms of spin characteristics, the *NV* center is marked by its triplet ground state, divided into three levels with $m_S = \pm 1$ states being energetically equivalent and the $m_S = 0$ state being of lower energy [59]. Application of a magnetic field removes this degeneracy, a feature crucial for magnetic sensing technologies. Importantly, optical transitions within these states preserve spin, enabling magneto-optical phenomena [60, 61].

A schematic representation of the structure of the NV, the energy-level diagram of NV^- and the typical emission band of ensembles of NV centers is reported in Figure 1.5.

One way to employ diamond color centers for biological imaging is by the functionalization of diamond nanoparticles. In particular, nanodiamonds can be synthesized in numerous ways [62], but the most common method relies on crushing micron-sized diamonds formed under high pressure and temperature in a hydraulic press [63].

Nanodiamond particles present numerous advantages over bulk samples when dealing with biological sensing and imaging. In particular, their small size, even on the nanometer scale, allows for easy penetration into cells, tissues, and even subcellular structures, offering their utilization as nanometric sensors capable of detecting changes in physiological parameters and other biological substances. Furthermore, nanodiamonds have a strong and chemically active surface that can easily changed with different functional groups. This allows biomolecules such as proteins, nucleic acids, and antibodies to be attached, making them valuable instruments for targeted medicine administration [52].

Due to these peculiar properties, color centers in diamonds and other biocompatible semiconductors, in general, are critical for biological sensing and imaging. Nitrogen-Vacancy centers embedded in nanodiamonds, in particular, provide a reliable single photon source that can be used in sub-Poissonian super-resolution techniques, as well as a dedicated tool for nanometric environmental sensors.

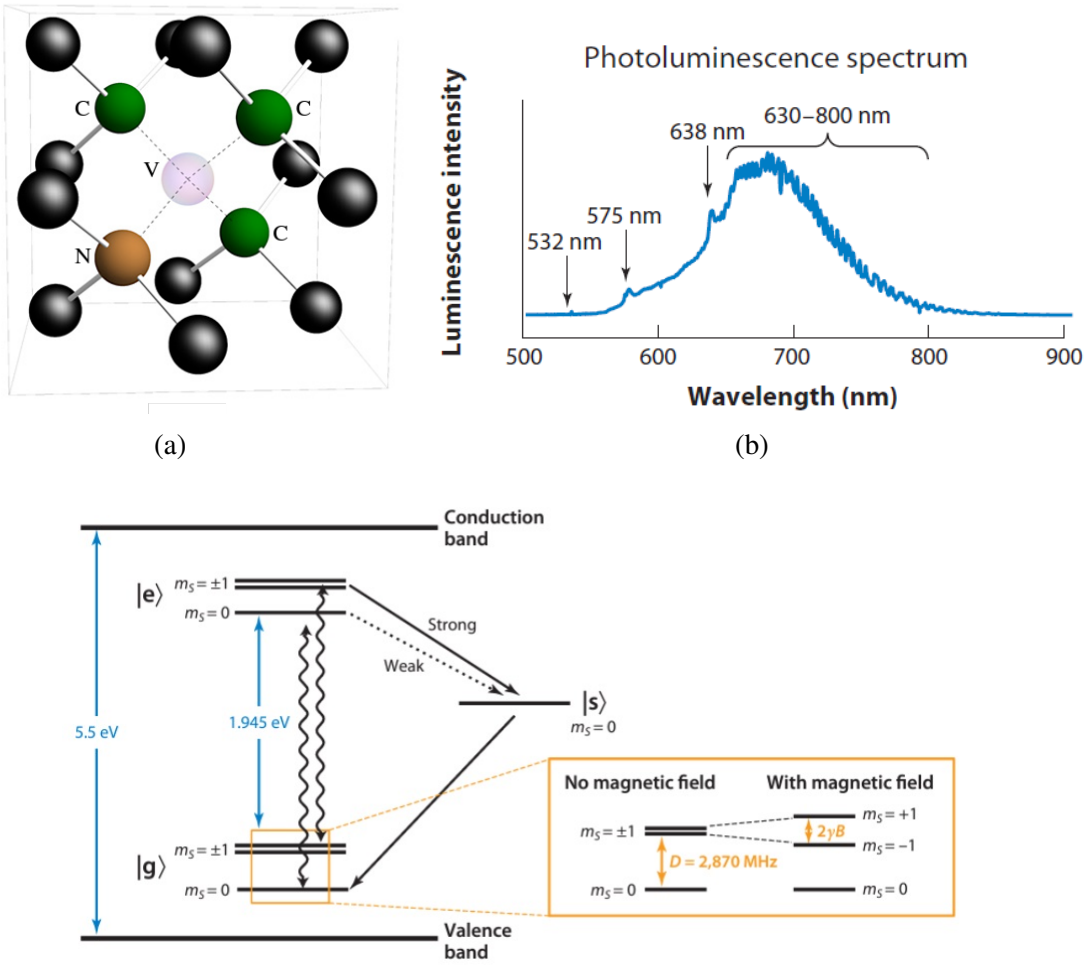

Figure 1.5: *Overview of the Nitrogen-Vacancy Center: structure, photoluminescence spectra, and energy levels. Panel (a): structure of a Nitrogen-Vacancy center in diamond [58]. Panel (b): typical photoluminescence spectra of Nitrogen-Vacancy centers [42] showing excitation laser 532 nm, the NV^0 zero phonon line (575 nm), the NV^- zero phonon line (638 nm), and NV^- vibrational side bands (630 nm - 800 nm). Panel (c): energy-level arrangement for NV^-, indicating $|g\rangle$ as the electronic ground state, $|e\rangle$ as the electronic excited state, and $|s\rangle$ as the metastable singlet state. The diagram uses squiggly arrows to denote radiative transitions and solid arrows for depicting the magnitude of non-radiative decay through the singlet state. An inset reveals the trio of spin sublevels for $m_S = 0$ and $m_S = \pm 1$, observable in both absence and presence of a magnetic field B. Here, D denotes the zero-field splitting, while $2\gamma B$ illustrates the Zeeman splitting, where γ is the electron gyromagnetic ratio. By convention, the lower energy transition is identified with $m_S = -1$ [42].*

1.3 Other sources of single photon

For completeness, this section will briefly cover few other single-photon sources that are used in quantum-related applications.

Isolated atoms

The simplest form of an ideal single-photon emitter is an isolated atom, as it inherently cannot emit more than one photon per excitation cycle. In recent years, several attempts to trap single atoms in optical cavities have been proposed and implemented using both optical and magnetic traps [64, 65, 66]. Once trapped, the atom can be excited by a laser pulse, resulting in the emission of a single photon. A schematic of the working principle is reported in Figure 1.6. While this method theoretically offers the purest generation of single photons, the practical challenges in setting up such systems and the difficulties associated with their scalability limit their range of applications [67, 68].

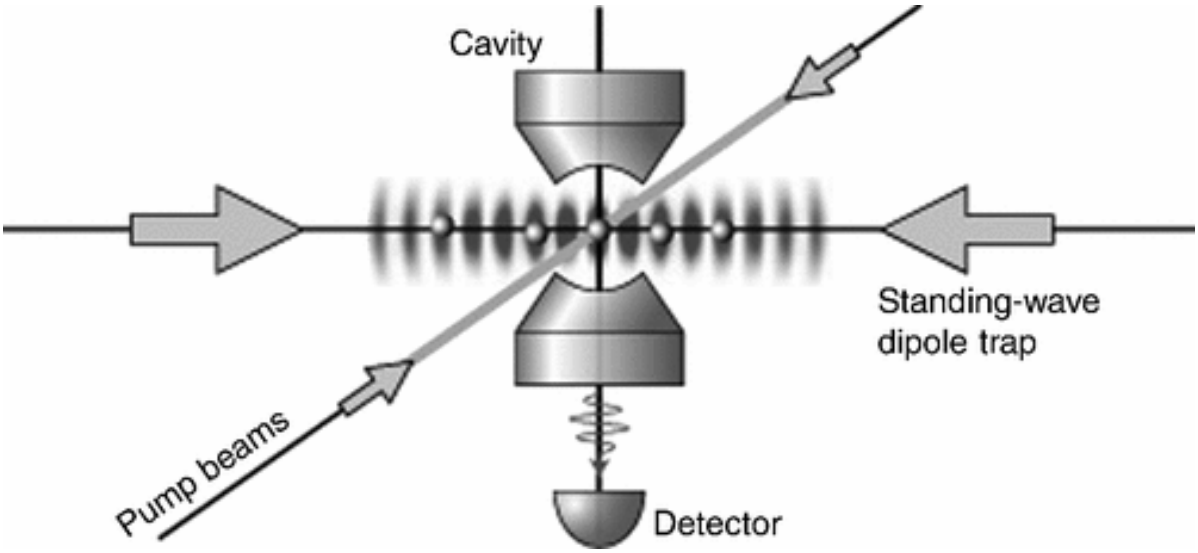

Figure 1.6: *Scheme of functioning of a trapped atom system: The atom is trapped inside the cavity through an opto-magnetic trap and subsequently excited through pump beams. The emitted radiation from the atom is subsequently collected by a single-photon detector. [69]*

Non-linear photon generation processes

Both solid-state single-photon emitters and isolated atoms can be considered deterministic single-photon sources due to their ability to emit a single photon upon each excitation pulse. In contrast, other single-photon sources depend on probabilistic processes that utilize the

nonlinear properties of specific materials, such as Beta Barium Borate (BBO), Potassium Titanyl Phosphate (KTP), and Lithium Niobate ($LiNbO_3$). In particular, in these materials, the polarization response is not directly proportional to the intensity of the incident light, giving rise to second and third order processes.

Specifically, an incoming pump beam interacting with a nonlinear crystal can generate pairs of entangled photons through second-order nonlinear processes such as Spontaneous Parametric Down Conversion (SPDC) and third order ones like Spontaneous Four Wave Mixing (SFWM) [70, 71].

In SPDC, a photon from the pump beam is annihilated, producing a pair of photons while conserving energy and momentum. SFWM, on the other hand, involves the annihilation of two pump photons to generate a pair of entangled photons. These processes are schematically illustrated in Figure 1.7.

When photon pairs are produced, they are emitted simultaneously (within a few fs). The detection of one photon, known as *idler*, heralds the presence of the second photon known as *signal*, which can then be used as a single photon in quantum systems [72]. Although heralded sources are inherently probabilistic because they depend on spontaneous processes and cannot produce photons on demand, their efficiency can be enhanced. One method is through spatial multiplexing, which involves combining photons from different spatial modes enhancing the heralded single-photon efficiency of the system [73]. Furthermore, these single-photon devices can be easily integrated with standard integrated CMoS technology. This, and their ability of tailoring photon wavelengths, enables flexible and scalable solutions for advanced quantum technologies [74, 75, 76].

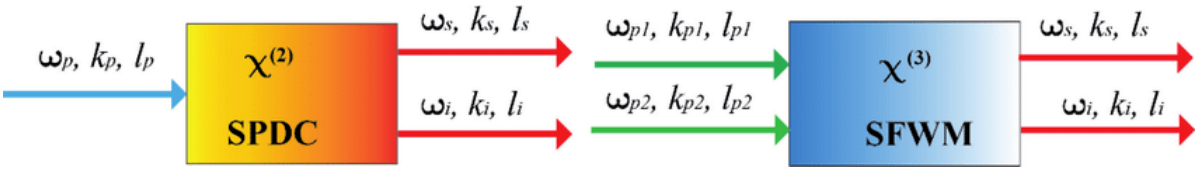

Figure 1.7: *Schematic representation of the second-order nonlinear process SPDC (left) and the third-order nonlinear process SFWM (right). In both processes, energy (ω), linear momentum (k), and angular momentum (l) are conserved. [77].*

Chapter 2

Overview of imaging techniques

This chapter will briefly present some basic concepts of classical optical imaging and its physical resolution limits. Subsequently, some super-resolution methods suitable for biological applications will be discussed. In particular, it will be presented two types of techniques; the first one relies on achieving super-resolution by harnessing the photon statistics of non-Poissonian light sources, while the second one relies on increasing the maximum spatial frequency information achievable by exploiting structured light illumination.

2.1 Point Spread Function and diffraction limit

The response of a focused optical imaging system to a point source or point object is described by the Point Spread Function (PSF). In many cases, the PSF may be viewed as an extended spot in the image plane representing a single-point object that is considered a spatial impulse (see Figure 2.1). The analytical expression of the PSF is related to the Bessel Function of order one J_1:

$$PSF(\mathbf{r}) \propto \frac{J_1(\mathbf{r})^2}{\mathbf{r}^2}, \tag{2.1}$$

where $\mathbf{r}$ refers to the radial distance from the optical axis. However, it is more practical to ignore the relatively small high-order maximum of the Bessel function and to approximate the central lobe with a Gaussian profile [78] as shown in Figure 2.2.

The degree of blurring of an image is related to the spatial width of the PSF and is a measure of the imaging system's quality. The image creation process in non-coherent imaging systems, such as fluorescence microscopes, telescopes, or optical microscopes, is linear in image intensity and is represented by a linear system theory.

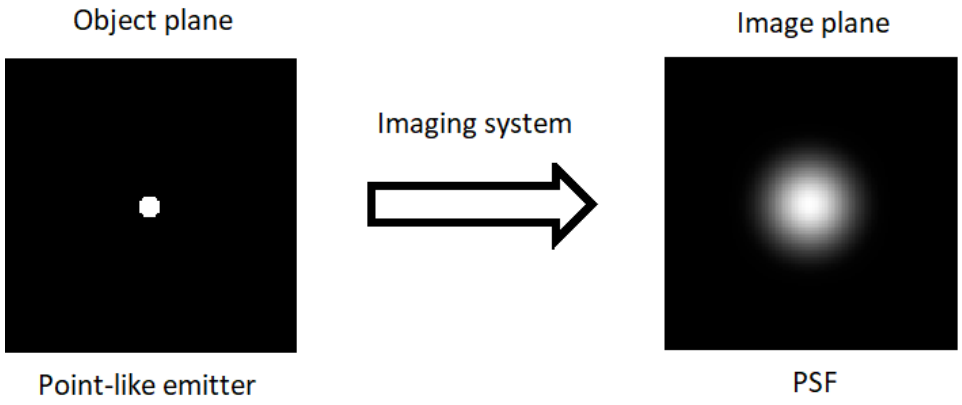

Figure 2.1: *Schematic representation of the effect of imaging systems on point-like emitters.*

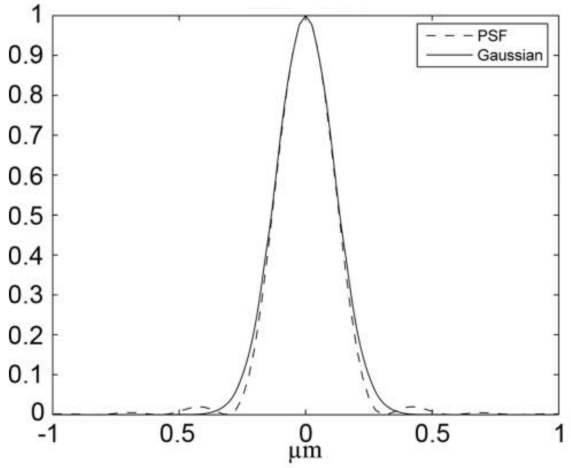

Figure 2.2: *Cross-section through the PSF (dashed curve) and its Gaussian profile approximation (solid curve) [78].*

In a non-coherent imaging system, the image of two objects A and B is equal to the independent sum of the two images as taken separately [79]. In other words, since the photon coming from the two points does not have a definite phase relation, there are no interference effects, and imaging of A is unaffected by imaging of B and vice versa. The image of a complex object is thus the convolution of that object and the PSF in space-invariant systems, i.e. those in which the PSF is the same everywhere in the imaging space.

Variables such as lens flaws or misalignment may limit the resolution of an optical imaging instrument such as a microscope, telescope, or camera. The physics of diffraction, on the other hand, puts a basic limit on the resolution of any optical system when direct intensity measurement at the detection plane is performed.

The smallest resolvable features in a microscope are determined by Abbe's diffraction limit (see Figure 2.3). The lowest resolvable distance (d_{Abbe}) between two points in an image,

according to Abbe's diffraction limit, is equal to half the wavelength of light (λ) divided by the numerical aperture (NA) of the objective lens [80]:

$$d_{\text{Abbe}} = \frac{\lambda}{2NA}. \tag{2.2}$$

An objective lens' numerical aperture is a measurement of its ability to collect light and discern tiny details. NA can be expressed through the relation:

$$NA = n\sin(\theta), \tag{2.3}$$

where n is the index of refraction of the medium through which the lens operates and θ is the half-angle of the widest cone of light that can pass through the lens. A big numerical aperture means that a wide light cone enters the objective lens, allowing for better resolution. The wavelength λ utilized in the imaging process is also important in determining resolution. Smaller wavelengths of the electromagnetic spectrum, such as those in the ultraviolet or blue ranges, allow for greater resolution imaging than longer wavelengths, such as those in the red or infrared spectrum.

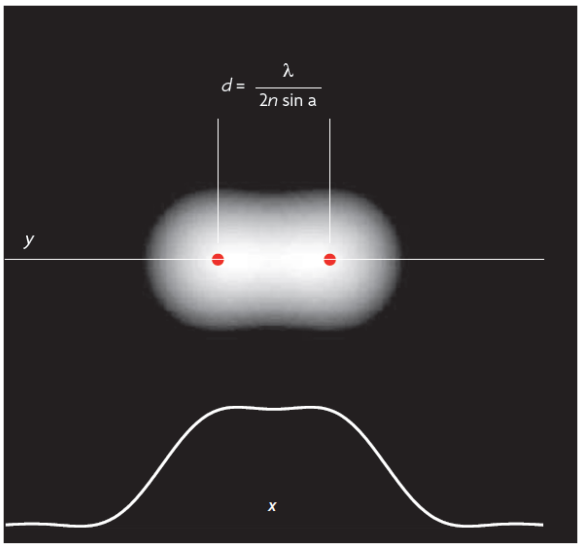

Figure 2.3: *An image of two points blurred by diffraction can be resolved only at distances $d \geq d_{Abbe}$. In the bottom part of the image is displayed the brightness in the direction of the separation [81].*

2.2 Super-resolution with non-Poissonian light sources

As previously discussed, the image of a point-like emitter is blurred in the image plane due to diffraction phenomena that can be approximated by a Gaussian profile:

$$PSF(\mathbf{r}) \propto e^{-\frac{(\mathbf{r}-\mathbf{r_0})^2}{2\sigma^2}}, \tag{2.4}$$

where $\mathbf{r_0}$ is the position of the emitter and σ is the spatial standard deviation of the PSF.

The spatial standard deviation of the approximated PSF can be linked to the minimum resolvable distance, d_{Abbe}. Specifically, the relationship is given by: $d_{Abbe} = \sigma/0.42$ [78]. This implies that, according to the definition of Abbe's limit, two emitters can be spatially resolved if the distance between them is greater than $\sigma/0.42$.

Performing the k-th power of the Point Spread Function will cause the PSF to shrink by a factor of $\sqrt{k}$, retrieving a narrower image spot. However, in the presence of multiple emitters closer in the image plane by a distance less than the minimum resolvable one, performing the k-th power of the fluorescence signal will not provide better resolution due to cross-term contributions.

Consider a general case of a random distribution of N_c single photon emitters in the object plane $S(\mathbf{r}) = \sum_{\alpha=1}^{N_c} \delta(\mathbf{r}-\mathbf{r}_\alpha)$ where $\delta(\mathbf{r}-\mathbf{r}_\alpha)$ represents the Dirac delta function. The intensity recorded in the image plane will be:

$$D(\mathbf{r}) \propto PSF(\mathbf{r}) * S(\mathbf{r}) = \sum_{\alpha=1}^{N_c} PSF(\mathbf{r}-\mathbf{r}_\alpha), \tag{2.5}$$

$$D^k(\mathbf{r}) \propto \sum_{\alpha=1}^{N_c} PSF^k(\mathbf{r}-\mathbf{r}_\alpha) + c.t. \tag{2.6}$$

The symbol $*$ denotes the spatial convolution.

To achieve a super-resolved image, a correction for the cross-terms must be applied; in particular, it has been demonstrated that analyzing the photon distribution of sub-Poissonian [5, 7] or super-Poissonian [6] light sources can be effective. These super-resolution methods are ideal for biological applications because they operate efficiently without requiring high excitation power or special label preparation.

A visualization of how increasing the exponentiation of the PSF introduce super-resolution is reported in Figure 2.4.

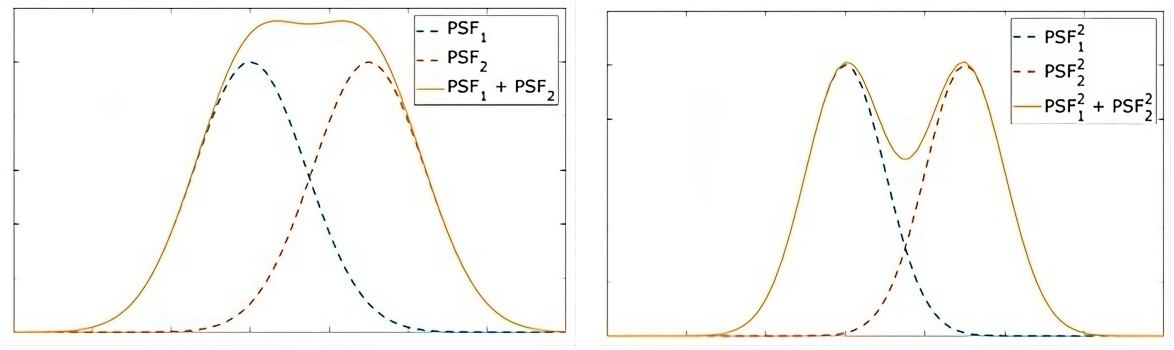

(a) (b)

Figure 2.4: *Resolution enhancement through PSF shrinking. (a) Sum of two PSFs closer than the minimum resolvable distance. (b) Sum of the square of the PSFs makes a dip appearing, highlighting the presence of the internal structure.*

2.2.1 Super-resolution via sub-Poissonian statistics

Super-resolution using sub-Poissonian light sources can be achieved by reconstructing the second-order correlation image of a sample of single-photon emitters [5, 7]. Let's consider a specimen with N_c ideal single photon sources randomly distributed and excited by a single laser pulse. Each emitter will be characterized by a density matrix:

$$\hat{\rho}_\alpha(\mathbf{r}) = \eta_\alpha(\mathbf{r})|1\rangle\langle 1| + [1-\eta_\alpha(\mathbf{r})]\,|0\rangle\langle 0|, \tag{2.7}$$

where $\eta_\alpha(\mathbf{r})$ represents the probability of detecting a single photon (considering all optical losses and the effect of the PSF) at position $\mathbf{r}$ on the detector plane.

Since all emitters are independent, the total density matrix for the entire system is given by $\hat{\rho}(\mathbf{r}) = \otimes_{\alpha=1}^{N_c}\hat{\rho}_\alpha(\mathbf{r})$.

Defining the number of detected photons from the system of single-photon emitters as:

$$\hat{N}(\mathbf{r}) = \sum_{\alpha=1}^{N_c} \hat{a}_\alpha^+(\mathbf{r})\hat{a}_\alpha(\mathbf{r}) = \sum_{\alpha=1}^{N_c} \hat{n}_\alpha(\mathbf{r}), \tag{2.8}$$

yields:

$$\langle\hat{N}(\mathbf{r})\rangle = \mathrm{Tr}[\hat{\rho}(\mathbf{r})\hat{N}(\mathbf{r})] = \sum_{\alpha=1}^{N_c}\langle\hat{n}_\alpha(\mathbf{r})\rangle = \sum_{\alpha=1}^{N_c}\eta_\alpha(\mathbf{r}) = D(\mathbf{r}). \tag{2.9}$$

The final equality coincide with the expression presented in Equation 2.5, where the sum of the α-th PSFs results in the classical mean intensity image $D(\mathbf{r})$.

Squaring Equation 2.9 results in a sum of PSF with spatial variance reduced by a factor of 2 and cross-terms given by the sum of the product of PSF of different emitters:

$$\langle \hat{N}(\mathbf{r}) \rangle^2 = \sum_{\alpha=\alpha'}^{N_c} \langle \hat{n}_\alpha(\mathbf{r}) \rangle^2 + \sum_{\alpha \neq \alpha'}^{N_c} \langle \hat{n}_\alpha(\mathbf{r}) \rangle \langle \hat{n}_{\alpha'}(\mathbf{r}) \rangle. \tag{2.10}$$

The cross terms can be expressed using the second-order correlation function, as described in Section 1.1:

$$\langle \hat{N}(\mathbf{r}) \rangle^2 g^{(2)}(0,\mathbf{r}) = \langle \hat{N}^2(\mathbf{r}) - \hat{N}(\mathbf{r}) \rangle = \sum_{\alpha=\alpha'}^{N_c} \langle \hat{n}_\alpha^2(\mathbf{r}) \rangle + \sum_{\alpha \neq \alpha'}^{N_c} \langle \hat{n}_\alpha(\mathbf{r}) \hat{n}_{\alpha'}(\mathbf{r}) \rangle - \sum_{\alpha=1}^{N_c} \langle \hat{n}_\alpha(\mathbf{r}) \rangle. \tag{2.11}$$

Since the emission of two different emitters is uncorrelated, the term $\sum_{\alpha \neq \alpha'}^{N_c} \langle \hat{n}_\alpha(\mathbf{r}) \hat{n}_{\alpha'}(\mathbf{r}) \rangle$ can be written as $\sum_{\alpha \neq \alpha'}^{N_c} \langle \hat{n}_\alpha(\mathbf{r}) \rangle \langle \hat{n}_{\alpha'}(\mathbf{r}) \rangle$, which is precisely the cross term in Equation 2.10. Therefore, we obtain:

$$\langle \hat{N}(\mathbf{r}) \rangle^2 = \sum_{\alpha=\alpha'}^{N_c} \langle \hat{n}_\alpha(\mathbf{r}) \rangle^2 + \langle \hat{N}(\mathbf{r}) \rangle^2 g^{(2)}(0,\mathbf{r}) + \sum_{\alpha=1}^{N_c} \langle \hat{n}_\alpha(\mathbf{r}) \rangle - \sum_{\alpha=\alpha'}^{N_c} \langle \hat{n}_\alpha^2(\mathbf{r}) \rangle. \tag{2.12}$$

Given that the emitters are single photon sources, the quantities $\langle \hat{n}_\alpha(\mathbf{r}) \rangle = \langle \hat{n}_\alpha^2(\mathbf{r}) \rangle$ are equal. Therefore, the terms $\sum_{\alpha=1}^{N_c} \langle \hat{n}_\alpha(\mathbf{r}) \rangle$ and $\sum_{\alpha=\alpha'}^{N_c} \langle \hat{n}_\alpha^2(\mathbf{r}) \rangle$ cancel out. Rearranging Equation 2.12 leaves the expression for the second-order super-resolved map with sub-Poissonian light (labeled $SR_{sub}^{(2)}(\mathbf{r})$):

$$SR_{sub}^{(2)}(\mathbf{r}) = \sum_{\alpha=1}^{N_c} \eta_\alpha^2(\mathbf{r}) = \langle \hat{N}(\mathbf{r}) \rangle^2 [1 - g^{(2)}(0,\mathbf{r})]. \tag{2.13}$$

Here, $\eta_\alpha^2(\mathbf{r}) = \langle \hat{n}_\alpha(\mathbf{r}) \rangle^2$.

This analysis can be extended to an arbitrary k-th power of the signal. For example, the third-order power will be:

$$SR_{sub}^{(3)}(\mathbf{r}) = \sum_{\alpha=1}^{N_c} \eta_\alpha^3(\mathbf{r}) = \langle \hat{N}(\mathbf{r}) \rangle^3 [1 - \frac{3}{2} g^{(2)}(0,\mathbf{r}) + \frac{1}{2} g^{(3)}(0,0,\mathbf{r})]. \tag{2.14}$$

The general expression for an arbitrary k-th power can be written as:

$$SR_{sub}^{(k)}(\mathbf{r}) = \sum_{\alpha=1}^{N_c} \eta_\alpha^k(\mathbf{r}) = \langle \hat{N}(\mathbf{r}) \rangle^k \sum_{i}^{i_{max}} \gamma_i \beta_i, \tag{2.15}$$

where γ_i are multiplicative coefficient and β_i represents terms like $g^{(j_1)}(\tau_1 = 0, \ldots, \tau_{j_1-1} = 0, \mathbf{r}) \ldots g^{(j_l)}(\tau_1 = 0, \ldots, \tau_{j_l-1} = 0, \mathbf{r})$ and i_{max} is the number of possible (ordered) combinations, satisfying the condition $\sum_{p=1}^{l} j_p = k$ [7].

In Figure 2.5 is reported a sub-Poissonian super-resolution obtained exploiting by the anti-bunching of single Nitrogen-Vacancy centers in diamond in a confocal microscopy setup.

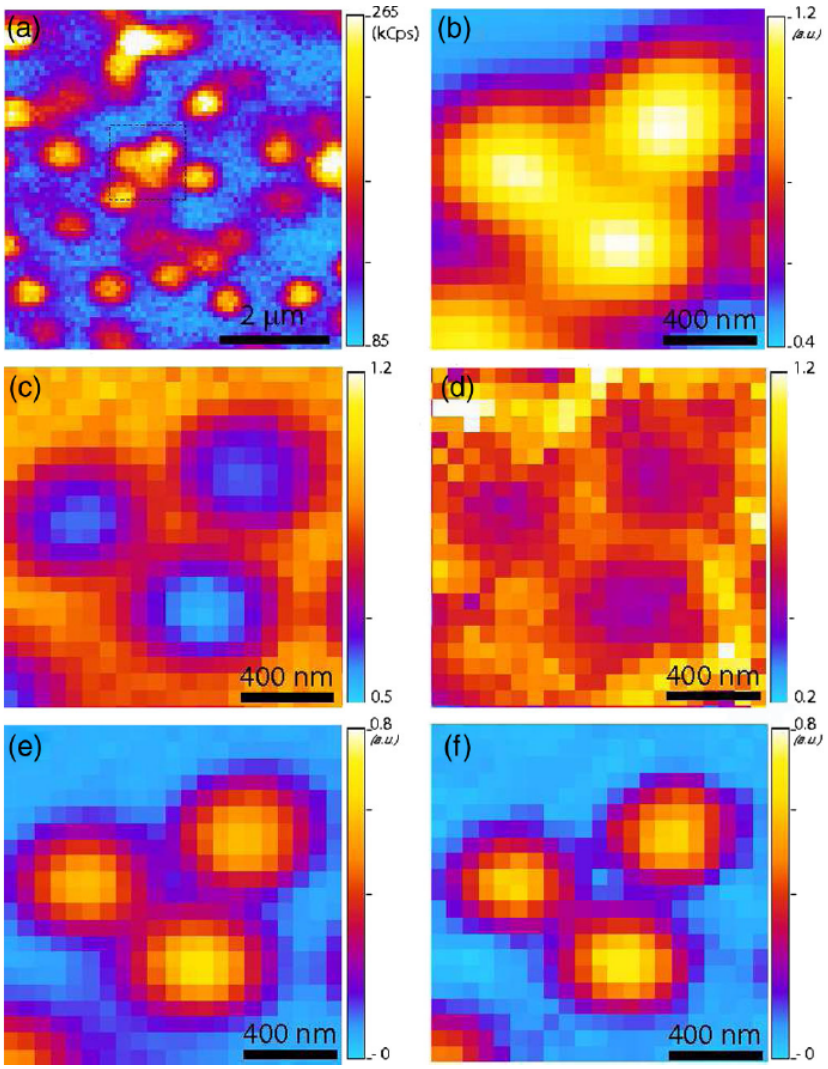

Figure 2.5: *Example of the super-resolution technique applied to a cluster of Nitrogen-Vacancy centers. (a) Scan on a region of the sample obtained collecting the signals emitted by each center on a pixel-by-pixel basis via a single-photon sensitive confocal microscope. (b) Magnification of the area of interest. (c) $g^{(2)}(0)$ map. (d) $g^{(3)}(0,0)$ map. (e) Second-order super-resolved map. (f) Third-order super-resolved map [7].*

2.2.2 Super-resolution via super-Poissonian statistics

As discussed in Section 1.2.1, quantum dots blinking leads the emitter to an "Off" state. Since this process is associated with charge carrier traps inside individual quantum dots, the blinking mechanism is independent for each emitter. This phenomenon can be exploited to achieve super-resolution, using a technique known as Super-resolution Optical Fluctuation Imaging (SOFI) [6] here briefly presented.

Usually, SOFI is described by a classical model in the literature. In this section we will present this approach, although a more rigorous quantum description will be presented in Chapter 5. Here, the signal from each emitter is assumed as time dependent statistical variable. As before, the fluorescence image $F(\mathbf{r},t)$ at position $\mathbf{r}$ on the detector plane at a specific time t from a sample of N_c emitters is given by the convolution of the distribution of emitters and the PSF, i.e. the function $\eta(\mathbf{r}-\mathbf{r}_\alpha)$:

$$F(\mathbf{r},t) = \sum_{\alpha=1}^{N_c} \eta(\mathbf{r}-\mathbf{r}_\alpha)\varepsilon_\alpha s_\alpha(t) = \sum_{\alpha=1}^{N_c} \eta_\alpha(\mathbf{r})\varepsilon_\alpha s_\alpha(t). \tag{2.16}$$

Here, ε_α represents the mean brightness of the center, while $s_\alpha(t)$ represents the time-dependent part. The temporal mean value ($D(\mathbf{r})$) and variance ($\mu_2(\mathbf{r})$) of the fluorescence image are:

$$D(\mathbf{r}) = \langle F(\mathbf{r},t)\rangle, \tag{2.17}$$

$$\mu_2(\mathbf{r}) = \langle F^2(\mathbf{r},t)\rangle - \langle F(\mathbf{r},t)\rangle^2. \tag{2.18}$$

Substituting $F(\mathbf{r},t)$ with its expression and dividing the sum into components $\alpha = \alpha'$ and $\alpha \neq \alpha'$ yields:

$$\begin{aligned}\mu_2(\mathbf{r}) = &\sum_{\alpha=\alpha'}^{N_c} \eta_\alpha^2(\mathbf{r})\varepsilon_\alpha^2\langle s_\alpha^2(t)\rangle + \\ &\sum_{\alpha\neq\alpha'}^{N_c} \eta_\alpha(\mathbf{r})\eta_{\alpha'}(\mathbf{r})\varepsilon_\alpha\varepsilon_{\alpha'}\langle s_\alpha(t)s_{\alpha'}(t)\rangle - \\ &\sum_{\alpha=\alpha'}^{N_c} \eta_\alpha^2(\mathbf{r})\varepsilon_\alpha^2\langle s_\alpha(t)\rangle^2 - \\ &\sum_{\alpha\neq\alpha'}^{N_c} \eta_\alpha(\mathbf{r})\eta_{\alpha'}(\mathbf{r})\varepsilon_\alpha\varepsilon_{\alpha'}\langle s_\alpha(t)\rangle\langle s_{\alpha'}(t)\rangle.\end{aligned} \tag{2.19}$$

Since the fluctuation in the emission of different emitters is uncorrelated, the two terms with $\alpha \neq \alpha'$ will cancel each other, leaving the expression for the second-order super-resolved map exploiting super-Poissonian statistics (labeled $SOFI^{(2)}$):

$$SOFI^{(2)}(\mathbf{r}) = \mu_2(\mathbf{r}) = \sum_{\alpha=\alpha'}^{N_c} \eta_\alpha^2(\mathbf{r})\varepsilon_\alpha \left(\langle s_\alpha^2 \rangle - \langle s_\alpha \rangle^2\right). \tag{2.20}$$

This approach can be extended to a generic k-th power of the fluorescence image. In this case, we must consider the cumulant of order k, c_k, a quantity used to characterize the behavior of a probability distribution or a stochastic process.

Cumulants are a combination of central moments of a given distribution $P(n)$ and can be derived starting from the cumulant-generating function:

$$\mathscr{C}(t) = \log\left(\sum_{n=0}^{\infty} e^{tn} P(n)\right). \tag{2.21}$$

In particular the k-th order cumulant can obtained by performing the k-th derivative of $\mathscr{C}(t)$ evaluated in $t = 0$:

$$c^{(k)} = \frac{d\mathscr{C}}{dt}(t)|_{t=0}. \tag{2.22}$$

In SOFI, it is stated that a super-resolved map can be obtained by evaluating the k-th order cumulant of the detected photon distribution [6]:

$$c^{(k)}(\mathbf{r}) = \sum_{\alpha=1}^{N_c} \eta_\alpha^k(\mathbf{r})\varepsilon_\alpha^k b_\alpha. \tag{2.23}$$

Here, b_α is a correlation-based weighting function, depending on the specific fluctuation properties of each emitter. The exact expression for b_α depends on the order of the cumulants. It's worth noting that a challenge associated with this super-resolution technique is its dynamic range; if there are multiple emitters closer than the minimum resolvable distance, high-order cumulants will enhance the information of those with a higher blinking rate, as shown in Figure 2.6.

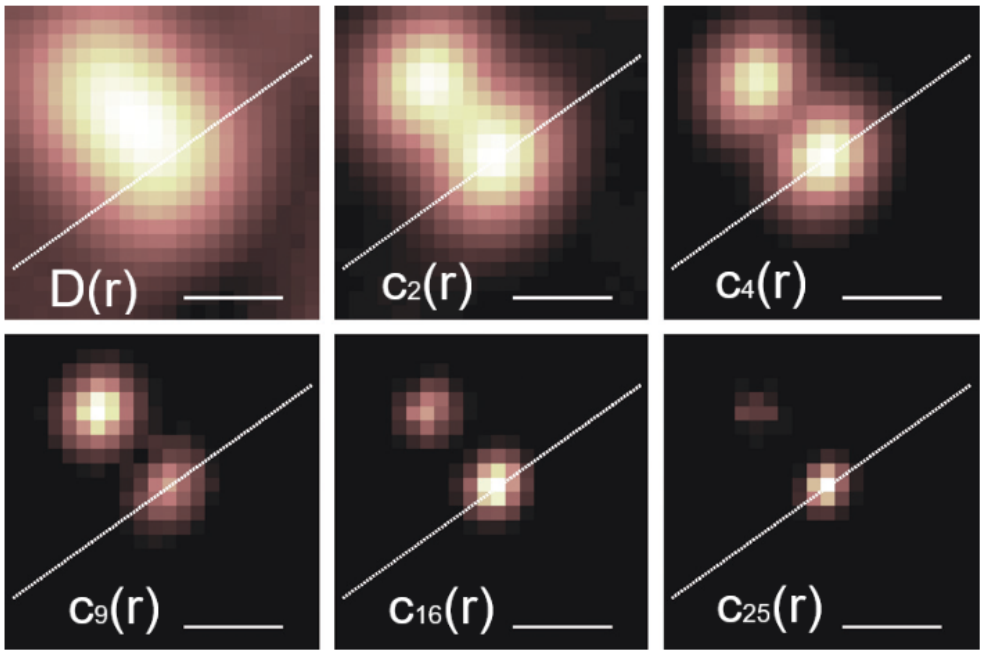

Figure 2.6: *Wide-field image of two different quantum dots (first panel) and increasing high order cumulants (2,4,9,16,25). Note that the relative intensities of the two quantum dots vary depending on the specific blinking behavior of each emitter, effect enhanced with higher order cumulants [6].*

2.3 Structured Illumination Microscopy

As discussed in Section 2.1, the image of a point-like emitter is distorted due to the inevitable diffraction in the imaging setup, resulting in a non-point-like PSF. Considering this effect from a frequency domain perspective, the blurring induced by the imaging setup can be viewed as a low-pass filter. To achieve super-resolution, it is essential to recover high-frequency information.

Structured Illumination Microscopy (SIM) is a super-resolution microscopy technique that has demonstrated the capability to enhance the high-frequency components of a specimen [8].

SIM operates by illuminating the sample with a patterned light source, typically a grid or a sequence of parallel lines. This structured light interacts with the sample, generating Moiré-like interference patterns [82], as depicted in Figure 2.7. High-frequency information is extracted by acquiring a series of images with varying phases and orientations of the patterned lighting.

This super-resolution method work without prior knowledge of the nature of the emitters and can be operated at low excitation power, making it a biocompatible super-resolution technique.

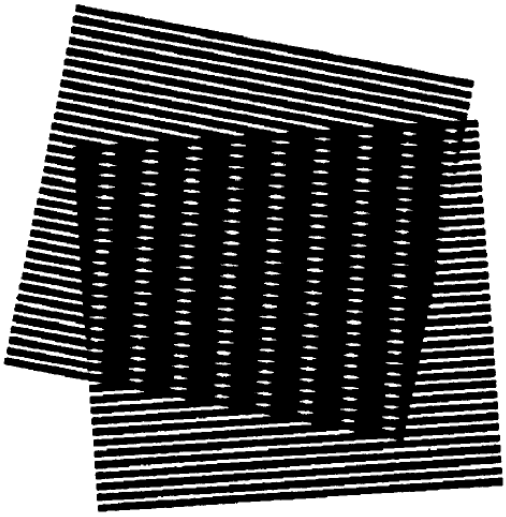

Figure 2.7: *Moirè fringes formation. Two high frequency patterns are superimposed, creating a low-frequency spatial pattern [8].*

Computational procedures are employed to combine these high-frequency images into the final super-resolved image. These algorithms analyze the spatial frequency content of the images and use the known lighting pattern to reconstruct a higher-resolution image with enhanced spatial details. This approach effectively surpasses the diffraction limit, providing an improvement in resolution by up to two times.

The fundamental principle of SIM involves using a non-Gaussian beam as an excitation source. In practice, a typical Gaussian laser beam is directed at a diffraction grating, from which the first two diffraction maxima are selected. These two maxima then interfere on the sample surface, resulting in an excitation profile given by:

$$I_{\theta,\phi}(\mathbf{r}) = \frac{I_0}{2}\left[1 - \cos(2\pi \mathbf{p}_\theta \cdot \mathbf{r} + \phi)\right]. \tag{2.24}$$

Here, I_0 represents the peak illumination, $\mathbf{r}$ is the spatial position vector, ϕ is the phase of the illumination pattern, and $\mathbf{p}_\theta$ is the illumination frequency vector in reciprocal space.

Considering a random distribution of emitters $S(\mathbf{r})$, the observed distribution through the optical system is [83]:

$$D_{\theta,\phi}(\mathbf{r}) = \left[S(\mathbf{r}) I_{\theta,\phi}(\mathbf{r})\right] * \eta(\mathbf{r}). \tag{2.25}$$

Exploiting the convolution theorem, the Fourier transform of the signal will be:

$$\tilde{D}_{\theta,\phi}(\mathbf{k}) = \left[\tilde{I}_{\theta,\phi}(\mathbf{k}) * \tilde{S}(\mathbf{k})\right] \tilde{\eta}(\mathbf{k}), \tag{2.26}$$

where $\tilde{\eta}(\mathbf{k})$ denotes the Fourier transform of the product between the transmission efficiency of the setup and the PSF, also known as Optical Transfer Function (OTF). Writing the intensity profile in terms of complex exponential and using the convolution theorem leads to:

$$\tilde{D}_{\theta,\phi}(\mathbf{k}) = \frac{I_0}{2}\left[\tilde{S}(\mathbf{k}) - \frac{1}{2}\tilde{S}(\mathbf{k}-\mathbf{p}_\theta)e^{-i\phi} - \frac{1}{2}\tilde{S}(\mathbf{k}+\mathbf{p}_\theta)e^{i\phi}\right]\tilde{\eta}(\mathbf{k}). \tag{2.27}$$

The Fourier transform of the observed emission distribution is a linear combination of three frequency contents inside three circular sections of specimen $\tilde{S}(\mathbf{k})$: one centered at the origin, and two centered respectively at $-\mathbf{p}_\theta$ and $+\mathbf{p}_\theta$. The component $\tilde{S}(\mathbf{k})\tilde{\eta}(\mathbf{k})$ is the frequency component achievable with conventional illumination profiles, however, due to the sinusoidal light pattern exploited, a greater region in the reciprocal space (along the direction given by the angle θ) is reconstructed. A graphic representation is reported in Figure 2.8.

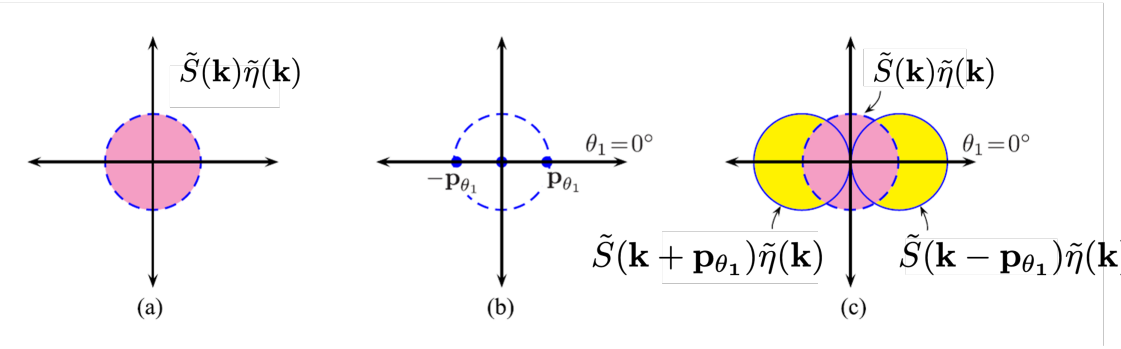

Figure 2.8: *Frequency components in Structured Illumination Microscopy. (a) Observable frequency component limited by the optical system. (b) Position in the reciprocal space of the vector p_{θ_l} and $-p_{\theta_l}$ ($\theta_l = 0$) with respect to the observable frequency components. (c) Observed frequency content exploiting structured illumination for a specific value of $\theta_l = 0$ [83].*

Equation 2.27 alone does not provide sufficient information to discern the three circular regions. To separate all the components, it is necessary to capture three distinct images with the same θ but varying ϕ and construct the system of equations presented in Equation 2.28.

$$\begin{bmatrix} \tilde{D}_{\theta,\phi_1}(\mathbf{k}) \\ \tilde{D}_{\theta,\phi_2}(\mathbf{k}) \\ \tilde{D}_{\theta,\phi_3}(\mathbf{k}) \end{bmatrix} = \frac{I_0}{2}\mathbf{M}\begin{bmatrix} \tilde{S}(\mathbf{k})\tilde{\eta}(\mathbf{k}) \\ \tilde{S}(\mathbf{k}-\mathbf{p}_\theta)\tilde{\eta}(\mathbf{k}) \\ \tilde{S}(\mathbf{k}+\mathbf{p}_\theta)\tilde{\eta}(\mathbf{k}) \end{bmatrix}, \tag{2.28}$$

where:

$$\mathbf{M} = \begin{bmatrix} 1 & -\frac{1}{2}e^{-i\phi_1} & -\frac{1}{2}e^{i\phi_1} \\ 1 & -\frac{1}{2}e^{-i\phi_2} & -\frac{1}{2}e^{i\phi_2} \\ 1 & -\frac{1}{2}e^{-i\phi_3} & -\frac{1}{2}e^{i\phi_3} \end{bmatrix}. \tag{2.29}$$

As the quantities of interest are $\tilde{S}(\mathbf{k})\tilde{\eta}(\mathbf{k})$, $\tilde{S}(\mathbf{k}-\mathbf{p}_\theta)\tilde{\eta}(\mathbf{k})$, and $\tilde{S}(\mathbf{k}+\mathbf{p}_\theta)\tilde{\eta}(\mathbf{k})$, we need to invert Equation 2.28:

$$\begin{bmatrix} \tilde{S}(\mathbf{k})\tilde{\eta}(\mathbf{k}) \\ \tilde{S}(\mathbf{k}-\mathbf{p}_\theta)\tilde{\eta}(\mathbf{k}) \\ \tilde{S}(\mathbf{k}+\mathbf{p}_\theta)\tilde{\eta}(\mathbf{k}) \end{bmatrix} = \frac{2}{I_0}\mathbf{M}^{-1} \begin{bmatrix} \tilde{D}_{\theta,\phi_1}(\mathbf{k}) \\ \tilde{D}_{\theta,\phi_2}(\mathbf{k}) \\ \tilde{D}_{\theta,\phi_3}(\mathbf{k}) \end{bmatrix}. \tag{2.30}$$

To span double the radius in reciprocal space that is usually accessible with standard illumination, it is essential to conduct acquisitions at varying θ values, as depicted in Figure 2.9. Following this, the procedure outlined earlier must be replicated for each unique value of θ.

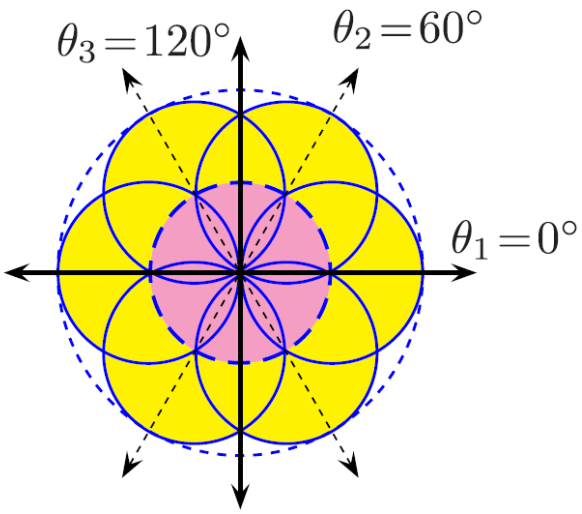

Figure 2.9: *Merging all the frequency information acquired with the three different values of θ is possible to cover twice the specimens frequency information [83].*

The minimum number of orientations θ required to achieve a super-resolved map is three (0°, 60°, 120°). Nevertheless, increasing the number of orientations will result in a less noisy super-resolved image.

2.3.1 Combining SIM with non-Poissonian light

Non-Poissonian super-resolution and Structured Illumination Microscopy in principle can be performed independently [20, 21]: while the first relies on the analysis of the photon statistics of the source, the latter exploits a peculiar way of illuminating the specimen.

A super-resolved map obtained by analyzing the non-Poissonian statistics of the emitters excited by structured illumination (labeled $SR^{(2)}_{\theta,\phi}(\mathbf{r})$) can be written as:

$$SR^{(2)}_{\theta,\phi}(\mathbf{r}) = \left[S(\mathbf{r})I^2_{\theta,\phi}(\mathbf{r})\right] * \eta^2(\mathbf{r}). \tag{2.31}$$

Performing the Fourier transform of the second-order super-resolved image and exploiting the convolution theorem it is obtained:

$$\tilde{SR}^{(2)}_{\theta,\phi}(\mathbf{k}) = \left[\tilde{I}^2_{\theta,\phi}(\mathbf{k}) * \tilde{S}(\mathbf{k})\right] \tilde{\eta}_2(\mathbf{k}). \tag{2.32}$$

Here, $\tilde{\eta}_2(\mathbf{k})$ refers to the Fourier transform of $\eta^2(\mathbf{r})$. We can write the square of the structured illumination profile as [21]:

$$\begin{aligned} I^2_{\theta,\phi}(\mathbf{r}) &= \frac{I_0^2}{4}\left[1-\cos(2\pi\mathbf{p}_\theta\cdot\mathbf{r}+\phi)\right]^2 \\ &= \frac{I_0^2}{4}\left[1+\cos^2(2\pi\mathbf{p}_\theta\cdot\mathbf{r}+\phi)-2\cos(2\pi\mathbf{p}_\theta\cdot\mathbf{r}+\phi)\right] \\ &= \frac{I_0^2}{4}\left[1+\frac{1}{2}+\frac{1}{2}\cos(4\pi\mathbf{p}_\theta\cdot\mathbf{r}+2\phi)-2\cos(2\pi\mathbf{p}_\theta\cdot\mathbf{r}+\phi)\right] \\ &= \frac{I_0^2}{4}\left[\frac{3}{2}+\frac{1}{2}\cos(4\pi\mathbf{p}_\theta\cdot\mathbf{r}+2\phi)-2\cos(2\pi\mathbf{p}_\theta\cdot\mathbf{r}+\phi)\right] \\ &= \frac{I_0^2}{4}\left[\frac{3}{2}+\frac{1}{4}e^{i(4\pi\mathbf{p}_\theta\cdot\mathbf{r}+2\phi)}+\frac{1}{4}e^{-i(4\pi\mathbf{p}_\theta\cdot\mathbf{r}+2\phi)}-e^{i(2\pi\mathbf{p}_\theta\cdot\mathbf{r}+\phi)}-e^{-i(2\pi\mathbf{p}_\theta\cdot\mathbf{r}+\phi)}\right]. \end{aligned} \tag{2.33}$$

Executing its Fourier transform and substituting it into Equation 2.32 yields to:

$$\begin{aligned} \tilde{SR}^{(2)}_{\theta,\phi}(\mathbf{k}) = \frac{I_0^2}{4}\Bigg[&\frac{3}{2}\tilde{S}(\mathbf{k})-\tilde{S}(\mathbf{k}-\mathbf{p}_\theta)e^{-i\phi}+\frac{1}{4}\tilde{S}(\mathbf{k}-2\mathbf{p}_\theta)e^{-2i\phi} \\ &-\tilde{S}(\mathbf{k}+\mathbf{p}_\theta)e^{i\phi}+\frac{1}{4}\tilde{S}(\mathbf{k}+2\mathbf{p}_\theta)e^{2i\phi}\Bigg]\tilde{\eta}_2(\mathbf{k}). \end{aligned} \tag{2.34}$$

In Equation 2.34, the terms $\tilde{S}(\mathbf{k})\tilde{\eta}_2(\mathbf{k})$, $\tilde{S}(\mathbf{k}-\mathbf{p}_\theta)\tilde{\eta}_2(\mathbf{k})$, and $\tilde{S}(\mathbf{k}+\mathbf{p}_\theta)\tilde{\eta}_2(\mathbf{k})$ signify the circular areas recoverable through the SIM technique, in addition to yielding a broader OTF owing to the reduced PSF size. Moreover, the squared nature of the excitation profile enables the capture of extra frequency content as indicated by the terms $\tilde{S}(\mathbf{k}-2\mathbf{p}_\theta)\tilde{\eta}_2(\mathbf{k})$ and $\tilde{S}(\mathbf{k}+2\mathbf{p}_\theta)\tilde{\eta}_2(\mathbf{k})$.

Similarly to classical SIM, Equation 2.34 alone is insufficient to recover all the obtainable frequency information along the direction θ. Instead, five second-order super-resolved images with different values of ϕ must be acquired:

$$\begin{bmatrix} \tilde{SR}^{(2)}_{\theta,\phi_1}(\mathbf{k}) \\ \tilde{SR}^{(2)}_{\theta,\phi_2}(\mathbf{k}) \\ \tilde{SR}^{(2)}_{\theta,\phi_3}(\mathbf{k}) \\ \tilde{SR}^{(2)}_{\theta,\phi_4}(\mathbf{k}) \\ \tilde{SR}^{(2)}_{\theta,\phi_5}(\mathbf{k}) \end{bmatrix} = \frac{I_0^2}{4}\mathbf{M_2} \begin{bmatrix} \tilde{S}(\mathbf{k})\tilde{\eta}_2(\mathbf{k}) \\ \tilde{S}(\mathbf{k}-\mathbf{p}_\theta)\tilde{\eta}_2(\mathbf{k}) \\ \tilde{S}(\mathbf{k}-2\mathbf{p}_\theta)\tilde{\eta}_2(\mathbf{k}) \\ \tilde{S}(\mathbf{k}+\mathbf{p}_\theta)\tilde{\eta}_2(\mathbf{k}) \\ \tilde{S}(\mathbf{k}+2\mathbf{p}_\theta)\tilde{\eta}_2(\mathbf{k}) \end{bmatrix}, \tag{2.35}$$

with:

$$\mathbf{M_2} = \begin{bmatrix} \frac{3}{2} & -e^{-i\phi_1} & \frac{1}{4}e^{-2i\phi_1} & -e^{i\phi_1} & \frac{1}{4}e^{2i\phi_1} \\ \frac{3}{2} & -e^{-i\phi_2} & \frac{1}{4}e^{-2i\phi_2} & -e^{i\phi_2} & \frac{1}{4}e^{2i\phi_2} \\ \frac{3}{2} & -e^{-i\phi_3} & \frac{1}{4}e^{-2i\phi_3} & -e^{i\phi_3} & \frac{1}{4}e^{2i\phi_3} \\ \frac{3}{2} & -e^{-i\phi_4} & \frac{1}{4}e^{-2i\phi_4} & -e^{i\phi_4} & \frac{1}{4}e^{2i\phi_4} \\ \frac{3}{2} & -e^{-i\phi_5} & \frac{1}{4}e^{-2i\phi_5} & -e^{i\phi_5} & \frac{1}{4}e^{2i\phi_5} \end{bmatrix}. \tag{2.36}$$

By inverting Equation 2.35, it becomes possible to derive all the components that recover frequency information along the θ direction, achieving up to $\sqrt{2}+2$ times the resolution attainable with classical microscopy:

$$\begin{bmatrix} \tilde{S}(\mathbf{k})\tilde{\eta}_2(\mathbf{k}) \\ \tilde{S}(\mathbf{k}-\mathbf{p}_\theta)\tilde{\eta}_2(\mathbf{k}) \\ \tilde{S}(\mathbf{k}-2\mathbf{p}_\theta)\tilde{\eta}_2(\mathbf{k}) \\ \tilde{S}(\mathbf{k}+\mathbf{p}_\theta)\tilde{\eta}_2(\mathbf{k}) \\ \tilde{S}(\mathbf{k}+2\mathbf{p}_\theta)\tilde{\eta}_2(\mathbf{k}) \end{bmatrix} = \frac{4}{I_0^2}\mathbf{M_2^{-1}} \begin{bmatrix} \tilde{SR}^{(2)}_{\theta,\phi_1}(\mathbf{k}) \\ \tilde{SR}^{(2)}_{\theta,\phi_2}(\mathbf{k}) \\ \tilde{SR}^{(2)}_{\theta,\phi_3}(\mathbf{k}) \\ \tilde{SR}^{(2)}_{\theta,\phi_4}(\mathbf{k}) \\ \tilde{SR}^{(2)}_{\theta,\phi_5}(\mathbf{k}) \end{bmatrix}. \tag{2.37}$$

To achieve a complete coverage of the reciprocal space and ensure uniform super-resolution across all directions, it is necessary to acquire multiple second-order super-resolved maps with different values of θ.

Using five distinct values of θ would be adequate for complete coverage; however, due to the expanded OTF resulting from second-order super-resolution via non-Poissonian statistics, four orientations will be sufficient. This implies a total of twenty independent acquisitions to generate a complete super-resolved map.

A visual representation of the observable region in the frequency domain, achievable through the combination of SIM and second-order super-resolution via non-Poissonian statistics, is illustrated in Figure 2.10.

The combination of non-Poissonian light statistics super-resolution and SIM can be extended to higher correlation orders. The generalization for an arbitrary correlation order m of Equation 2.32 is [21]:

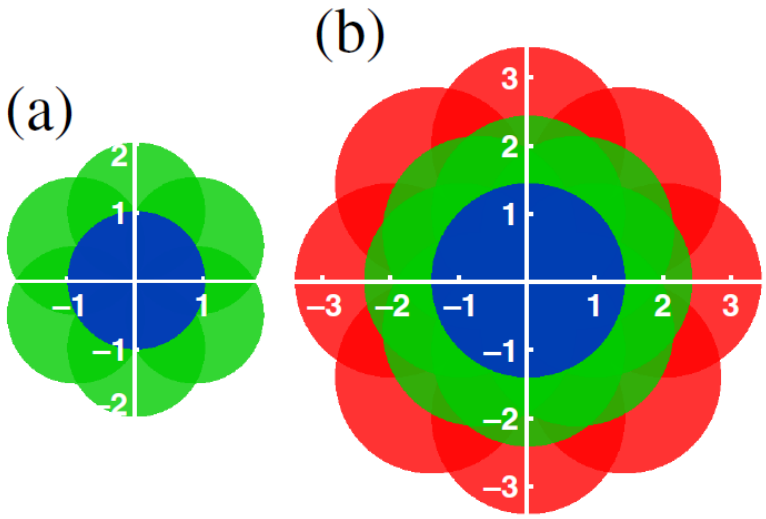

Figure 2.10: *Frequency components in traditional Structured Illumination Microscopy and when combined with non-Poissonian photon statistics. Observable region in OTF units for (a) classic SIM and (b) SIM combined with a second-order non-Poissonian super-resolution technique. The radius of the OTF in (b) is increased by a factor* $\sqrt{2}$ *due to the shrinking of the PSF, bringing an overall increase in super-resolution of* $2+\sqrt{2}$ *[21].*

$$\tilde{SR}^{(m)}_{\theta,\phi}(\mathbf{k}) = \left[\tilde{I}^{m}_{\theta,\phi}(\mathbf{k}) * \tilde{S}(\mathbf{k})\right] \tilde{\eta}_m(\mathbf{k}). \tag{2.38}$$

In this context, the size of the OTF radius will increase by a factor equal to $\sqrt{m}$, and the Fourier transform of the excitation profile raised to the power of m will include frequency components ranging from $-m|\mathbf{p}_\theta|$ to $+m|\mathbf{p}_\theta|$. The overall enhancement in super-resolution will grow proportionally to $m+\sqrt{m}$, offering the possibility of theoretically unlimited optical super-resolution. Nevertheless, this advantage is accompanied by the requirement of capturing a total of $5(2m+1)$ super-resolved images, which increases the total acquisition time.

Chapter 3

Image sensors

This chapter, structured into two main parts, will introduce the principal detectors utilized in both traditional and quantum optical imaging. The initial section will discuss detectors that exhibit a linear response to incident light, enabling their use as photon number resolving (PNR) detectors, at least in regimes where the equivalent detector noise can be neglected. This discussion will primarily center on Charge-Coupled Devices (CCDs), Complementary Metal-Oxide-Semiconductor (CMOSs) and Superconducting transition-edge sensors (TESs). The subsequent section will cover detectors noted for their exceptional single-photon sensitivity but non-linear response, which limits their use to distinguishing the mere presence or absence of photons, often referred to as "On-Off" detectors. Specifically, this part will focus on Electron Multiplying CCDs (EM-CCDs), Single Photon Avalanche Diodes (SPADs) and Superconducting Nanowire Single-Photon Detectors (SNSPDs), highlighting their main noise sources and operational principles.

3.1 Linear detectors

High-efficiency and low-noise linear detectors represent a critical advancement in imaging technology. The noise level can be, in some cases, so low that they offer the unique ability to approximately discern and count the number of photons hitting the detector. This capability is crucial for a wide range of applications, from quantum computing and cryptography to advanced microscopy and astronomical observation.

In the context of imaging and optical detection, a linear response implies that the detector's output is directly proportional to the intensity of the incoming light or radiation, i.e. the number of incident photons. This linear relationship is characterized by a constant sensitivity across a range of signal intensities.

This linearity simplifies the interpretation of the detector's output and allows for straightforward calibration and quantification of the measured signal.

Subsequently, three main classes of linear detectors are discussed: CCDs and CMOSs, which are commonly used in imaging, and TESs, which are currently being explored for potential imaging applications.

3.1.1 Charge-Coupled Devices

Charge-Coupled Devices (CCDs) are a cornerstone of modern imaging technology, widely utilized across various fields for their unparalleled ability to capture images with high fidelity.

CCDs operate on the principle of charge transfer. Light photons striking the sensor are converted into electrical charges at the pixel level. These charges are then transferred through the chip and read out at one corner of the array. A visual representation of the function of a CCD sensor is reported in Figure 3.1.

At its core, the architecture of a CCD involves a sequence of electrodes arranged over a semiconductor base, separated by a slim layer of insulating oxide. Applying voltage to these electrodes generates a depletion zone right below, essentially creating a storage space for charge packets. Through timely pulsing of these electrodes, this charge can be moved across the semiconductor. Incorporating additional circuits allows for the charge packets to be inserted and detected, effectively creating a shift register [84].

The fundamental design of a CCD sensor includes a grid of electrodes atop several discrete charge transfer paths. These electrodes are typically grouped in pairs or sets of three or four, and activating these groups forms a matrix of separate storage spots, or pixels, for the electrons produced by photons. After capturing an image, the electrodes in the imaging area are activated in sequence to move the captured charge pattern through the array line by line. The last line of the array is then shifted into a serial output register, which is clocked at a faster rate to sequentially read out each pixel via a charge detection amplifier. This process repeats until the entire image has been processed.

The architecture detailed above is known as a full-frame CCD array, favored for its application in scientific imaging within both space exploration and terrestrial astronomy. A challenge with this setup is the potential for image blurring during readout if the CCD is exposed to light, especially when the readout duration is a substantial portion of the exposure time. Solutions include the use of a mechanical shutter to block light during readout, or the addition of a protected storage array for transferring the captured image before reading it out in the dark. A design commonly used in CCD cameras for scientific applications is the frame-transfer design, that situates the storage array below the imaging area with the cost of doubling the chip size.

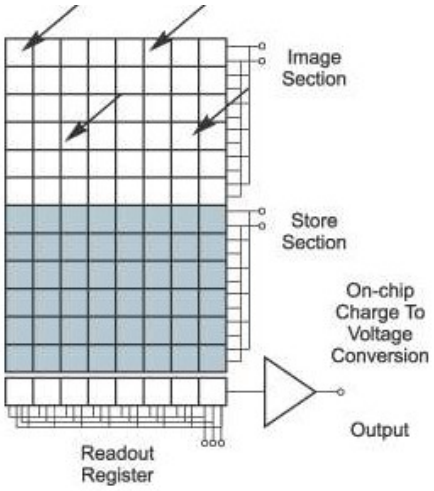

Figure 3.1: *Schematic of the CCD sensor in the frame transfer design [85].*

The spectral response of CCD detectors is optimized for the visible region of the electromagnetic spectrum, exhibiting peak quantum efficiencies between 70% and 95% in the wavelength range of 600–900 nm [86, 87].

This type of detector possesses different inherent sources of noise, in particular, thermal noise and readout noise. Thermal noise arises from the random generation of electrons within the silicon substrate of the CCD, independent of any incident light, and increases with temperature, as well as from the exposure time. However, this source of noise is efficiently reduced with cooling the CCD sensor, enhancing the SNR in low-light conditions or long-exposure applications [88]. On the other hand, readout noise is generated from the electronics associated with reading the charge from the CCD's pixels and does not depend on the exposure time of the frame or on the light intensity. This includes the on-chip amplifier and the analog-to-digital conversion process. Since the read noise is related to the readout process, it is a fundamental limit to the sensor's low-light capabilities [88]. In particular, state of the art CCDs sensors possess readout noise ranging from 1 to $3\,e^{-}/\text{pixel}/\text{frame}$ [89, 90].

A phenomenon that can occur in CCD detectors is the lack of charge carriers during the charge transfer process. As electrons are shifted through the substrate to the readout register, some may spill into adjacent pixel wells, especially if the wells are overfilled, (blooming) [91]. This phenomenon, known as cross-talk, can degrade image quality and, especially in quantum imaging applications, can furnish fake adjacent pixel correlations that alter the value of the correlation function evaluated at a specific position in the detector plane. In order to mitigate this effect, a control of the charge capacity of each pixel and the usage of anti-blooming structures that drain off excess charge can be applied.

3.1.2 CMOS sensors

Complementary Metal-Oxide-Semiconductor (CMOS) sensors represent a significant evolution in imaging technology. CMOS sensors use the same advanced silicon technology found in computer processors, allowing for the integration of millions of transistors on a single chip. This advancement facilitates the creation of an extensive pixel array where each pixel, equipped with its own photodiode and associated transistors, operates alongside necessary electronics for managing the array, buffering the analog signal, and converting it into digital format for further processing or display.

A basic CMOS pixel, for example, includes a photodiode connected to three transistors responsible for pre-charging the photodiode, sensing the signal, and selecting the pixel row. However, this setup can lead to variations in transistor performance, causing inconsistencies in pixel output across the sensor. Pixel arrays are typically organized in an x-y grid controlled by shift registers, though some designs allow for direct pixel selection through address decoders, enabling the reading of pixels in a specified row one at a time and then column by column. The signal from these pixels can be directed through various pathways, such as a multiplexer to an analog output, a single analog-to-digital converter (ADC), or multiple ADCs aligned with the columns [84].

A visual representation of the function of CMOS detectors is presented in Figure 3.2.

This pixel-level processing capability of CMOS sensors enables functionalities, such as noise reduction algorithms and variable sensitivity to light, directly on the imaging chip, which are not as readily achievable with CCD technology [92]. The operational spectral range of CMOS sensors is similar to that of CCD sensors, functioning within the visible spectrum and achieving peak quantum efficiencies between 70% and 90% [93, 94].

CMOS offers the possibility to perform complex processing functions, such as motion detection and image stabilization, directly on the sensor chip due to the integration of sensor arrays with on-chip processing circuitry, making them suitable for applications as live cells imaging [95]. Furthermore, due to the individual transistors and circuitry for each pixel and the possibility of incorporating isolation techniques, the cross talk effect present in CCD detectors is highly mitigated [96].

Despite the advantages, CMOS sensors historically lagged behind CCDs in terms of image quality, mainly due to higher noise levels and lower sensitivity. However, continuous advancements in CMOS technology, including the development of back-illuminated sensors and improvements in noise reduction techniques, have significantly narrowed this gap. In particular, modern CMOS sensors can be considered almost PNR detectors, due to their low readout-noise of $\simeq 0.3\,\mathrm{e}^{-}/\mathrm{pixel}/\mathrm{frame}$ [97, 98].

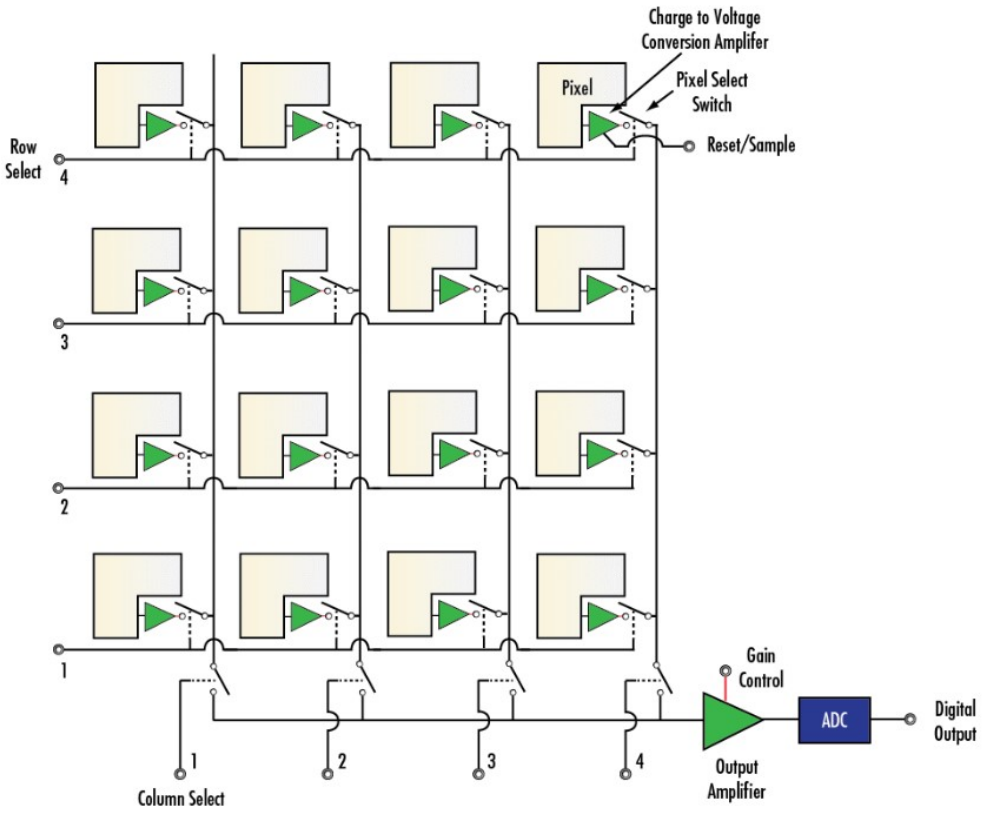

Figure 3.2: *Schematic of a CMOS sensor [99].*

3.1.3 Superconducting transition-edge sensors

Superconducting transition-edge sensors (TESs) operate at low temperatures and are renowned for their high-efficiency detection of single photons, low dark count rates and robust PNR capabilities.

The sensor element in a TES is a superconducting film positioned at the brink of transitioning from the superconducting state, where slight temperature variations lead to significant resistance changes. The capture of a photon increases the device's temperature, triggering a voltage-biased detector to generate a current measured by a readout circuitry. The magnitude of this signal correlates with the photon's energy or, for photons of a consistent wavelength, the number of photons [100].

A visual representation of a TES is reported in Figure 3.3.

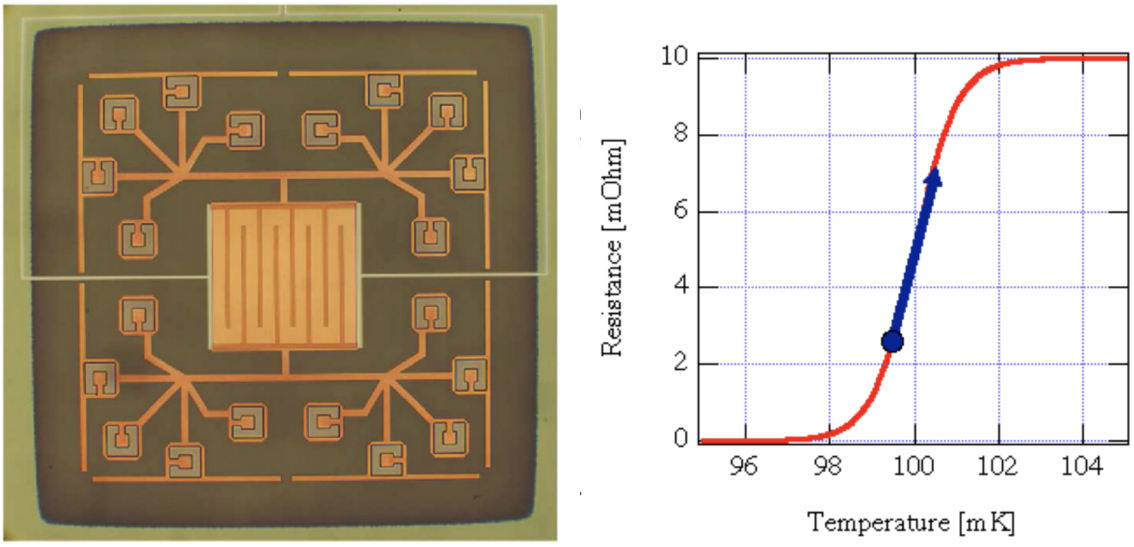

(a) (b)

Figure 3.3: *(a) Micrograph of a TES for gamma-ray spectroscopy. Superconducting molybdenum leads contact the left and right sides of a molybdenum-copper bilayer TES at the center. [101]. (b) Resistance vs temperature graph of a TES. Operating on the verge of a phase transition, the detector registers each incoming photon as a temperature rise, which is reflected as an increase in resistance. The energy captured in a single detection event reveals the energy of the absorbed photon. Furthermore, when dealing with monochromatic sources, it is possible to determine the count of photons detected based on the energy measured [102].*

These devices require operation at an approximate temperature of 100 mK, demanding advanced cooling techniques. Detectors made of tungsten exhibit a 20% detection efficiency [103], which can escalate to 95% at 1550 nm when incorporated within an optical cavity and over 80% at 850 nm [104], while maintaining minimal dark counts [105]. However, effective dark count rates might increase due to ambient blackbody radiation at room temperature, a challenge that can be somewhat addressed through filtering at the expense of detection efficiency [106].

Despite their high efficiency, TES detectors' timing accuracy is relatively low, with dead times, i.e. the period following an event during which the detector is unable to record another event, typically around 1 µs. Furthermore, TESs possess an intrinsic variability in the timing accuracy of detecting photons, resulting in fluctuations in the precise moment a photon is registered by the sensor, on the order of 100 ns , phenomenon known as jitter.

This variability means that even if photons arrive at the sensor at regular intervals, the recorded times of their arrival might differ due to the sensor's inability to consistently register each photon at the exact moment it interacts with the sensor. In practical terms, this leads to a spread in the detection times around the actual arrival time of each photon, complicating the

interpretation of fast temporal sequences of photons and affecting applications that rely on precise timing information, such as quantum cryptography or high-speed quantum communication systems. Jitter emerges from a combination of influences, each contributing to the variability in detection timing.

Thermal noise, for instance, can cause fluctuations in the sensor's temperature, affecting the consistency of the superconducting-to-normal transition. Electronic noise from the readout circuitry adds another layer of timing uncertainty. The intrinsic process of photon absorption and subsequent energy conversion to heat within the TES varies slightly with each event, impacting the uniformity of response times. Lastly, fluctuations in thermal conductance between the TES and its thermal bath can lead to variable cooling times post-detection, influencing the detector's readiness for subsequent photons detection. Together, these factors interplay to cause jitter in TES sensors, presenting challenges in applications demanding high temporal precision.

These detectors have proven their effectiveness in quantum optics and long-distance quantum key distribution [106, 107]. More recently, the development of arrays of TES sensors has laid the foundation for their use in imaging applications [108, 109].

3.2 On-Off detectors

On-Off detectors, characterized by their non-linear response to incoming signals, represent a distinct category of photon detection technology. Unlike linear detectors, where output directly correlates with the input signal, On-Off detectors show a more complex relationship between input light and output signal. This non-linear behavior is primarily used to identify the presence or absence of photons without quantifying their number. Consequently, these detectors are pivotal in contexts where precision in detecting photon arrival rather than counting them is crucial, necessitating advanced calibration and data analysis methods.

Such detectors are particularly beneficial in applications where their unique attributes are most needed. For example, in environments where light is scarce, the exceptional sensitivity of non-linear detectors like Electron Multiplying Charge-Coupled Devices (EM-CCDs), Single Photon Avalanche Diodes (SPADs) and Superconducting nanowire single-photon detectors (SNSPDs) is vital.

3.2.1 EM-CCD

At the heart of an EM-CCD's functionality is the electron multiplication (EM) process, which significantly amplifies the signal before it encounters the readout noise barrier. This amplification is achieved through a specialized structure within the CCD, known as the EM register,

which facilitates the multiplication of electrons generated by photon interactions in the sensor's silicon. This process, reliant on impact ionization, enables the detection of exceedingly faint signals, effectively bringing single-photon detection within reach. The unique architecture of EM-CCDs allows for the manipulation of the multiplication gain, providing flexibility in balancing between signal amplification and the associated increase in noise [110]. A visual representation of a structure of an EM-CCD camera is reported in Figure 3.4.

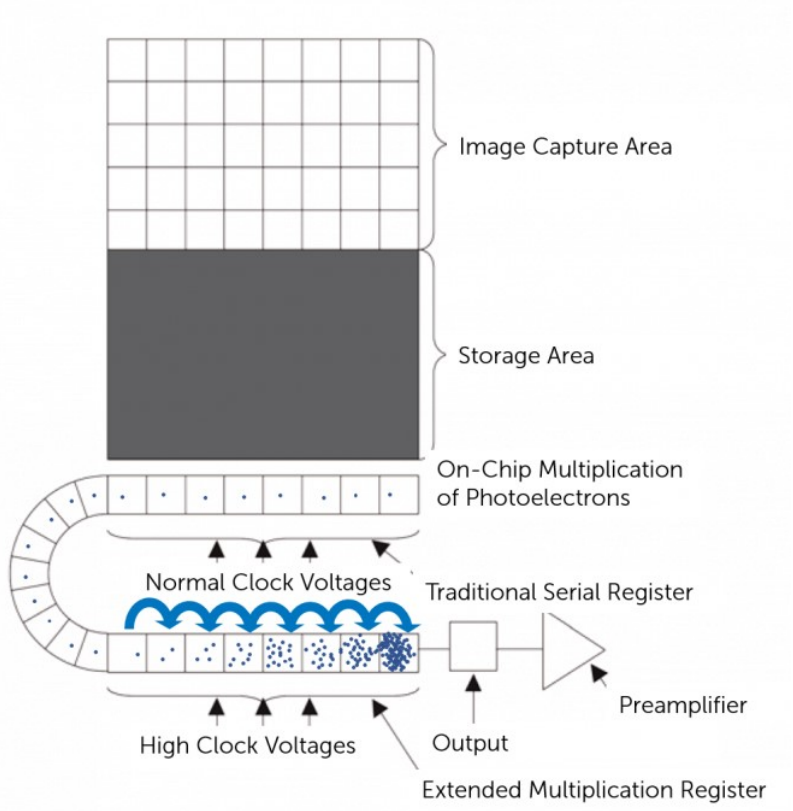

Figure 3.4: *Schematic of the EMCCD sensor [111].*

Despite their high sensitivity, EM-CCDs are not immune to noise. In particular, the main source of noise that arises when operating with low light level conditions is the Clock-Induced-Charged (CIC) noise. CIC noise is produced as the charge is transferred through the device during readout, with the potential for additional charges being generated by the high-voltage clock pulses used to drive the electron multiplication process. These spurious charges are indistinguishable from real photo-generated charges, thereby contributing to the background noise and affecting the detector's ability to accurately count photons. Efforts to mitigate CIC noise focus on optimizing the clocking schemes and the physical structure of the EM-

CCD. Precise tuning of both parallel and serial clock waveforms is essential to minimize the generation of CIC, as well as the careful control of clock amplitudes and device temperature.

Advanced EM-CCD designs and operating strategies have been developed to reduce CIC levels, up to $7 \cdot 10^{-4}\,\mathrm{e}^{-}/\mathrm{pixel}/\mathrm{frame}$ [112] enhancing the capability for photon counting and improving the overall performance of EM-CCDs in low-light imaging applications.

Another important source of noise in EM-CCD detector is the multiplication noise. This type of noise is inherent to the gain mechanism within the EM register of an EM-CCD. As electrons are accelerated through the high-voltage environment of the EM register, they collide with the silicon lattice, generating secondary electrons in a process known as impact ionization. This multiplication process is inherently random, leading to variations in the amount of gain applied to different signal electrons. As a result, even if two photoelectrons enter the EM register with identical initial conditions, the final number of electrons output from the EM register can vary, introducing noise into the amplified signal.

The presence of multiplication noise affects the optimal operation of EM-CCDs, particularly in low-light applications where the goal is to maximize the SNR. While the multiplication gain allows for the detection of single photons by amplifying the signal above the readout noise, the accompanying multiplication noise limits the achievable SNR. Specifically, EM-CCD technology is unsuitable for use as PNR detectors due to the fact that multiplication noise introduces uncertainty in the relationship between the output signal and the initial number of photo-electrons, especially when dealing with more than one photon. This trade-off between signal amplification and noise increase necessitates careful optimization of the EM gain setting to balance the benefits of signal amplification against the detrimental effects of noise [113].

After amplification, the signal is contaminated with various noise sources, such as CIC, dark current, and multiplication noise. To differentiate actual photon events from noise artifacts, a method of thresholding is applied. Nonetheless, altering the threshold value of the output signal also affects the quantum efficiency of the detector, consequently, comprehensive calibration is required to optimize it. This is exemplified in Figure 3.5, where it is shown the efficiency's dependency on the threshold value.

After carefully selecting the threshold value of the system, any signal exceeding the threshold is considered a photon detection event, while signals below the threshold are treated as noise. The threshold level is crucial for the performance of the EM-CCD as a single-photon detector. Setting the threshold too low increases the risk of false positives from noise, while setting it too high may result in missed photon events.

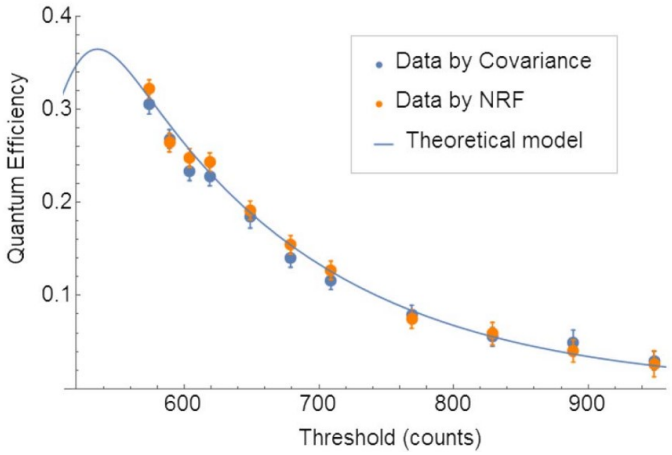

Figure 3.5: *Quantum efficiency as a function of the threshold in a EM-CCD camera [114].*

3.2.2 Single-Photon Avalanche Diodes

Single-Photon Avalanche Diodes (SPADs) are highly sensitive semiconductor devices that can detect single photons. SPADs function based on a unique principle compared to conventional photodetectors, referred to as Geiger mode.

When the diode is biased beyond its breakdown voltage, it enters a state of high sensitivity where the absorption of just one photon can initiate an avalanche multiplication process. This results in a detectable current pulse generated from a single-photon event. This avalanche is self-sustaining and continues until the bias voltage is reduced below the breakdown voltage, a process known as quenching. After quenching, the SPAD is reset, and it is ready to detect another photon.

The peak acquisition rate of SPADs is limited by the quenching process, requiring a period of inactivity known as dead time, during which the detector is unable to detect incoming photons. Specifically, contemporary SPADs feature a dead time of approximately a few nanoseconds, restricting their acquisition rates to the hundreds of MHz range [115]. The operation of SPADs highlights their non-PNR characteristic: the output signal from an avalanche triggered by a single photon is indistinguishable from that triggered by multiple photons. This is because the detection of even a single photon can initiate the avalanche that saturates the diode. A representation of the function of SPADs is reported in Figure 3.6.

Along with the thermal noise, typical for all the semiconductor detectors, a peculiar noise that arises in SPADs is the After-Pulse noise, a phenomenon where trapped carriers from a previous avalanche are released, causing subsequent avalanches unrelated to photon detections, affecting the accuracy and reliability of photon counting and timing measurements. After-

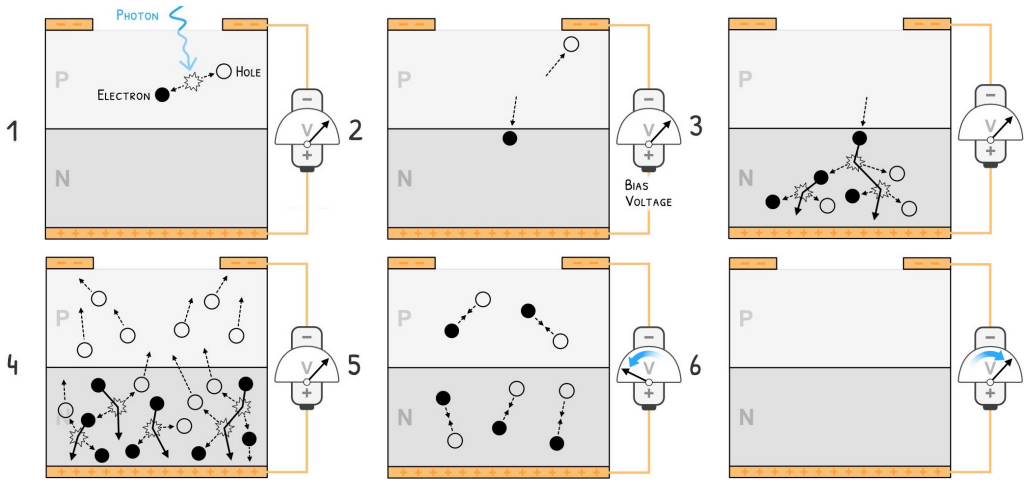

Figure 3.6: *Scheme of functioning of a SPAD. 1) Absorption of a photon and creation of a electron-hole pair. 2) Acceleration of the electron and hole by the bias voltage. 3) The accelerated electron knocks other electrons loose, creating an avalanche of carrier pairs. 4) Production of a rapidly growing current across the junction, which can be detected. 5) The bias voltage is then lowered, "quenching" the semiconductor to remove the existing carrier pairs. 6) The bias voltage is raised back to its initial state, resetting the device [116].*

pulsing is particularly critical in SPADs due to their operation in the high field regime, which enhances the probability of carrier trapping and release [117, 118].

SPADs excel in timing resolution due to their single-photon sensitivity and the discrete nature of their detection mechanism. When a photon triggers an avalanche in a SPAD, it generates a sharp, easily discernible signal, allowing for precise timing of photon arrival. The timing resolution of SPADs can be as low as a few picoseconds, limited by its intrinsic temporal variability, making them perfect for different applications in which knowing the arrival time of different photons is demanded, like fluorescence lifetime imaging microscopy [119], remote sensing [120] and quantum key distribution [121].

Jitter in SPADs originates the inherent stochastic nature of the photon absorption process, where the precise instant of photon interaction leading to an electron-hole pair varies unpredictably. Additionally, the physical attributes of the detector, including the geometry and material properties of the semiconductor junction, influence the signal propagation speed, thereby contributing to jitter. Specifically, in SPADs, the time required for the avalanche of charge carriers to reach a detectable magnitude can fluctuate.

While SPADs are noted for their rapid response and lower noise, their operational spectral range is primarily restricted to the visible portion of the electromagnetic spectrum, with peak quantum efficiencies ranging from 50% to 70% in the $500 - 700$ nm wavelength range [122, 123].

3.2.3 Superconducting Nanowire Single-Photon Detectors

Superconducting Nanowire Single-Photon Detectors (SNSPDs) stand at the forefront of quantum optics and photonics, offering unparalleled sensitivity and timing resolution for single-photon detection. These devices operate on the principle of superconductivity, employing ultra-thin films of superconducting materials, such as niobium nitride (NbN) [124] or molybdenum silicide (MoSi) [125], which are cooled below their critical temperatures to achieve a superconducting state. The nanowires, typically only a few nanometers thick and hundreds of nanometers wide, are configured in a meandering pattern to maximize the active detection area while maintaining a compact footprint.

When a photon interacts with the nanowire, it imparts sufficient energy to break Cooper pairs, the electron pairs that form the basis of superconductivity, creating a localized region, known as hotspot, where superconductivity is suppressed. This event generates a transient resistive state, causing a brief interruption in the superconducting current that flows through the nanowire. This change is detected as an electrical signal, marking the arrival of a photon. Events involving multiple photons cannot be distinguished from the detection of a single photon; both scenarios result in the creation of a hotspot, therefore suppressing superconductivity. A visual representation of SNSPDs functioning is reported in Figure 3.7.

As SPADs and TESs, also SNSPDs are characterized by the presence of jitter, in particular, the precise instant of photon interaction leading to the disruption of Cooper and the dynamics of hotspot formation characterize an high variability in the detected arrival time of photons. Furthermore, physical attributes of the detector, including the geometry and material properties of the nanowire, influence the signal propagation speed.

The unique architecture of SNSPDs enables them to exhibit extremely low dark count rates ($10^{-2} - 10^{-1}$ count/s [126, 127]) and rapid recovery times ($1 - 10$ ps [128, 129]), making them highly effective for a wide spectrum of photon-starved applications. Moreover, SNSPDs feature an operational wavelength range extending from UV to 10 µm, achieving quantum efficiencies near unity across a wide wavelength spectrum [130].

This exceptional quantum efficiency, particularly within the IR spectrum, renders SNSPDs more favorable than SPADs for applications such as remote sensing and quantum key distribution and, in recent years, there have been developments in the creation of arrays of SNSPDs, which have shown potential for imaging applications [131, 132]. Nonetheless, the necessity for cryogenic temperatures for their operation poses a significant challenge, requiring advanced cooling systems.

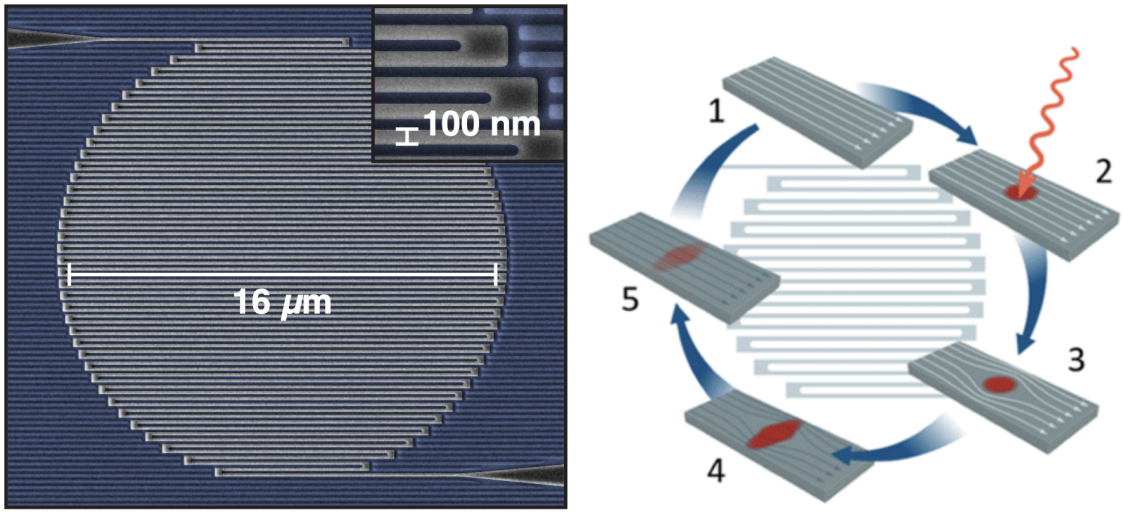

(a) (b)

Figure 3.7: *(a) Image of a single-pixel SNSPD designed to couple to light from a single-mode fiber [133]. (b) Functioning scheme of a SNSPD. 1) The SNSPD is cooled below its superconducting transition temperature and biased with a constant current. 2) When a photon is absorbed in the material, Cooper pairs are broken, resulting in a localized non-superconducting region called hotspot. 3) - 4) The hotspot grows until it covers the entire width of the nanowire, causing its resistance to increase to several kΩ on a timescale of picoseconds. 5) The nanowire cools off, returning to the superconducting state, and current rebuilds in the nanowire on a time scale of 10 ns. At this stage, the device is ready to count another photon. [130].*

Chapter 4

Experimental setup

In this Chapter is presented a detailed description of the experimental apparatus utilized in the framework of my Ph.D. thesis work, for both the realization of non-Poissonian super-resolution and its combination with Stuctured Illumination Microscopy.

4.1 Description of the optical setup

The experimental setup, reported in Figure 4.1, comprises an excitation source, specifically a 532 nm continuous-wave (CW) laser, which interacts with a Spatial Light Modulator (SLM) (Hamamatsu LCOS-SLM model X10468). The SLM first imposes a spatially varying phase shift onto the incoming wavefront of light, with each pixel on the SLM being individually controlled to adjust the phase of the light passing through it. The phase shift is determined using a grayscale image generated by a MATLAB script, which has the same pixel count as the SLM. The gray level of each pixel in the image specifies the degree of phase shift applied to the incoming wavefront by the corresponding pixel on the SLM. Subsequently, the phase shifted wavefront propagates through free space towards a lens.

This lens crucially performs an optical Fourier transform on the incoming wavefront, effectively converting the spatial phase modifications introduced by the SLM into amplitude variations at the focal plane. As a result, an interference pattern forms in the far field, which corresponds to the Fourier transform of the phase pattern applied by the SLM. The capability to control phase shift at the pixel level enables the creation of various interference patterns in the far field by simply generating different grayscale images.

From the interference beam, the two first maxima are selected through a mask, collimated by another lens and directed through a dichroic mirror with a cutoff wavelength of 550 nm.

Subsequently, the beam is focused on the surface of a glass sample, using a 100$\times$ air objective, containing a toluene solution of CdSe/ZnS colloidal quantum dots deposited via

spin-coating. The fluorescence emitted by the quantum dots, centered at 620 nm with a Full Width at Half Maximum (FWHM) of 20 nm, is captured by the objective and transmitted through the dichroic mirror. This radiation is further filtered by a 600 nm long-pass filter and a 700 nm short-pass filter, and finally collected by a low-noise CMOS camera.

It is important to note that in the experimental realization of non-Poissonian super-resolution images, as discussed in Section 5.2, the SLM is employed merely as a mirror and does not generate a diffraction pattern.

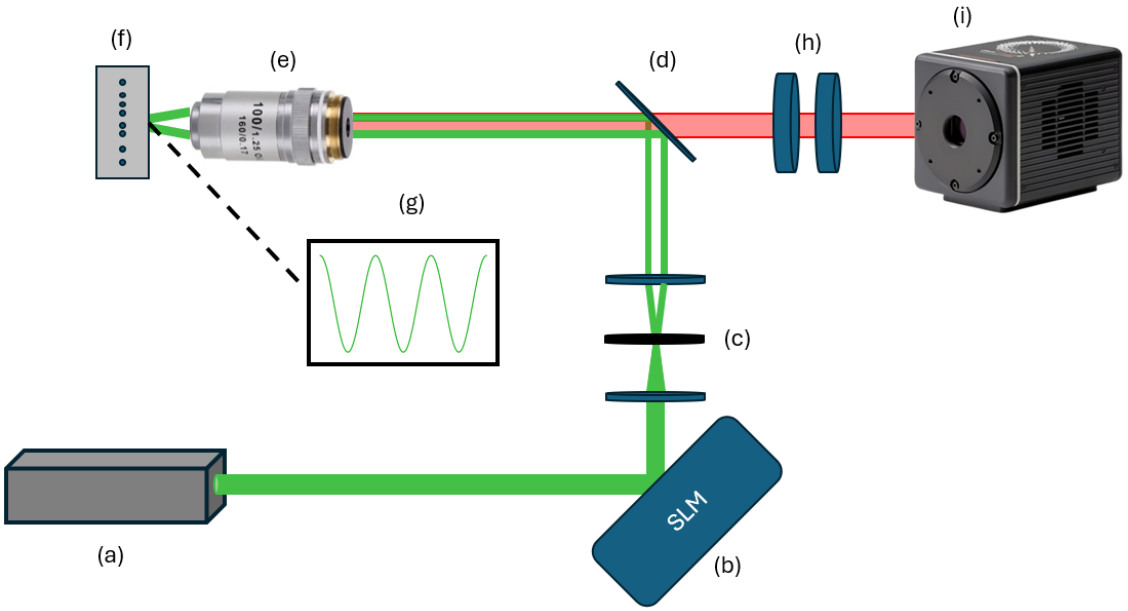

Figure 4.1: *Schematic of the experimental setup. (a) 532 nm continuous wave (CW) laser source. (b) Spatial Light Modulator (SLM). (c) Collimation lenses and a mask (in black) employed to isolate the first two interference maxima. (d) Dichroic mirror. (e) 100x air objective. (f) CdSe/ZnS quantum dots sample. (g) Structured illumination pattern, exciting the quantum dot sample, created by the interference of the two first orders of diffraction of the laser incident on the sample surface. (h) Optical filters comprising a 600 nm long-pass filter and a 700 nm short-pass filter. (i) Low-noise CMOS camera.*

4.2 CMoS camera

The CMoS camera utilized is an ORCA-QUEST C15550-20UP from Hamamatsu, characterized by a nominal low value of readout noise RMS (Root Mean Square) of $0.23\,e^{-}$.

The camera incorporates a back-illuminated sensor design in which the light hits the photodiode layer without having to pass through the electronic circuitry first, enhancing camera sensitivity and efficiency, especially in low light conditions. The quantum efficiency of the camera, reported in Figure 4.2, peaking at 85% at 460 nm, makes it suitable for visible light applications.

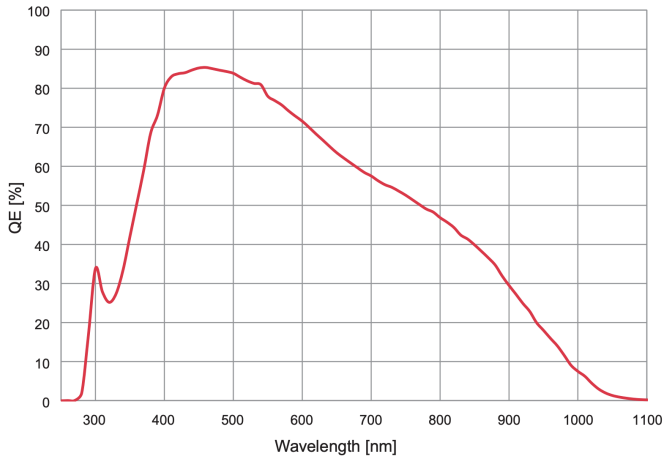

Figure 4.2: *Quantum Efficiency (QE) of the Hamamatsu ORCA-QUEST C15550-20UP as a function of wavelength λ [134].*

In a CMOS camera sensor, each pixel's output is given as a count value, C, which indirectly measures the photo-electrons, n_{pe}, generated during the exposure time. The relation between the count value and the actual number of photo-electrons is governed by a conversion factor, G, as expressed by the equation:

$$C = Gn_{pe}, \tag{4.1}$$

where G represents the amplification factor intrinsic to the pixel's electronic circuitry.

To accurately determine the conversion factor G of the sensor, a series of experimental acquisitions were conducted using a Poissonian light source. During these experiments, the light intensity was systematically varied, and the inherent bias count of each pixel was subtracted to isolate the effect of the light alone.

The mathematical relationship between the mean number of counts, $\langle C \rangle$, and its variance, $\mathrm{Var}(C)$, can be represented as follows:

$$\langle C \rangle = G\mu_{pe}, \tag{4.2}$$

$$\mathrm{Var}(C) = G\langle C \rangle + \mathrm{Var}(N). \tag{4.3}$$

In these equations, μ_{pe} is the mean number of photo-electrons, which, in a Poisson distribution, is equal to its variance. Additional noise, denoted as N, contributes to the variance, altering its estimation.

By plotting the variance of the counts against their mean, as shown in Figure 4.3, and applying a linear fit to these data, the conversion factor was determined. The analysis yielded a conversion factor $G = 9.4 \pm 0.2$ Counts/pe, which was utilized in the experiments discussed in subsequent sections. Furthermore, considering that in silicon, for wavelengths greater than 400 nm, only one electron-hole pair is generated per photon [135, 136], the actual number of photons detected at a specific position on the detector plane, denoted as $N(\mathbf{r})$, in experiments involving the use of quantum dots is estimated as:

$$N(\mathbf{r}) = \frac{Counts(\mathbf{r})}{G}. \tag{4.4}$$

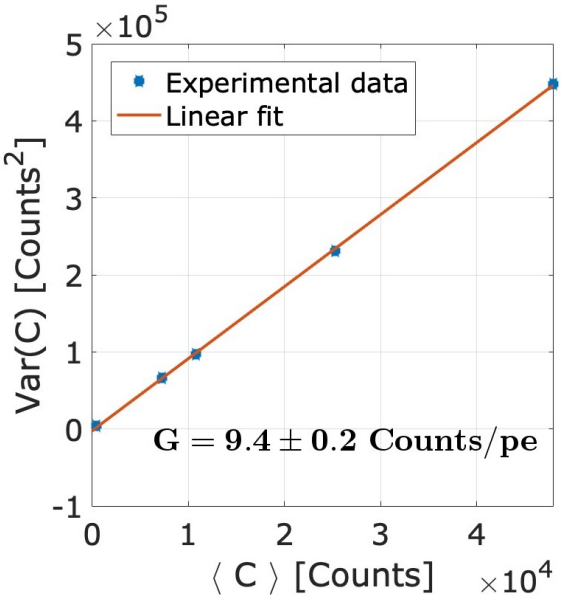

Figure 4.3: *Plot of the variance of the camera counts versus the mean number of counts, featuring a linear regression line. The slope of the line represents the conversion factor G between counts and photo-electrons.*

An analysis was performed to assess the readout-noise RMS of the camera, aiming to verify the effective low-noise characteristics of the sensor. An acquisition was made with only the presence of environmental stray light where the bias count of each pixel was subtracted from its total counts. These adjusted counts were then converted to photo-electrons using the previously determined conversion factor. The mean photo-electron value for each pixel is depicted in Figure 4.4a.

Subsequently, a histogram of the overall acquisition was created, correctly normalized to represent a probability distribution of photo-electrons, depicted in Figure 4.4b.

As described in Section 3.1.2, a typical CMOS camera is characterized by readout noise, which can be modeled as a Gaussian distribution [137]. Consequently, the overall distribution of photo-electrons is represented by the convolution of the Poisson distribution, which describes the photo-electrons generated during the integration time, and the Gaussian distribution with mean value $\mu_{RN} = 0$ and standard deviation RMS, which characterizes the readout noise.

A fitting of the convoluted distribution was executed, depicted by a continuous line in Figure 4.4b. From this analysis, the mean value of the Poissonian distribution was determined as $\mu_{pe} = 0.06 \pm 0.03$ pe, and the standard deviation of the Gaussian, representing the readout-noise level, was found to be RMS $= 0.23 \pm 0.01$ pe, compatible with the nominal value of RMS $= 0.23$ pe. This low value of readout noise confirms the camera's capability to discern single photon events in low-light conditions.

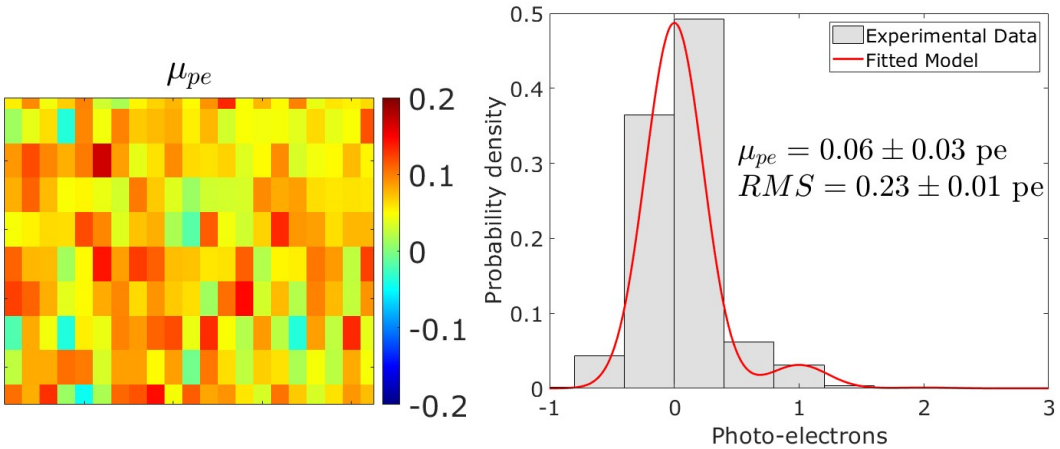

(a) (b)

Figure 4.4: *Characterization of the readout noise in the Hamamatsu ORCA-QUEST C15550-20UP camera. (a) Distribution of average photo-electron counts across pixels. (b) Observed probability distribution of photo-electrons (histogram) and the fitted probability distribution (red line) derived from a convolution of Poisson ($\mu_{pe} = 0.06 \pm 0.03$ pe) and Gaussian (centered at 0 and with standard deviation RMS $= 0.23 \pm 0.01$ pe), illustrating the noise characteristics of the sensor.*

4.3 CdSe/ZnS quantum dots

The emitters utilized in both non-Poissonian statistics super-resolution microscopy and their integration with Structured Illumination Microscopy are commercial colloidal CdSe/ZnS quantum dots with nominal quantum yield exceeding 70%, ensuring significant brightness of the emissions.

The quantum dot sample was prepared by depositing a toluene solution containing the quantum dots onto a glass slide, subsequently diluted with an isopropyl alcohol solution to reduce the concentration of the deposited quantum dots.

To ensure a uniform distribution of the emitters, the sample was subjected to spin coating, a technique used to apply uniform thin films to substrates. It involves depositing a liquid solution onto the center of a substrate and then spinning it at high speeds. The centrifugal force generated by the spinning spreads the solution evenly across the surface and expels excess liquid from the edges, leaving a thin film on the substrate. The thickness and uniformity of the film can be regulated by modifying the rotation speed and duration of the spin-coating process. In particular, the quantum dots sample was spin coated for 60 s at 100 rps.

Each quantum dot emitter exhibits independent blinking photon statistics, as delineated in Section 1.2.1, even under equal excitation conditions. To demonstrate this independence, photon statistics from two proximate emitters were analyzed. The mean photon count map from these emitters is shown in Figure 4.5a. Figures 4.5d and 4.5e illustrate the temporal profiles of the photon emissions from the regions circumscribing each emitter. Additionally, the experimental photon statistics Probability Density Functions (PDFs) for each emitter are presented in Figures 4.5b and 4.5c, respectively.

Both emitters display distinct 'On' and 'Off' states, but the overall blinking probability b, defined as the ratio of the time spent in the 'Off' state to the total acquisition time, varies between the emitters.

This variability is attributed to specific physical characteristics of the emitters, such as their size and shape. These results underscore that, even under identical excitation and detection conditions, adjacent emitters maintain independent photon statistics, thereby ensuring unique emission profiles.

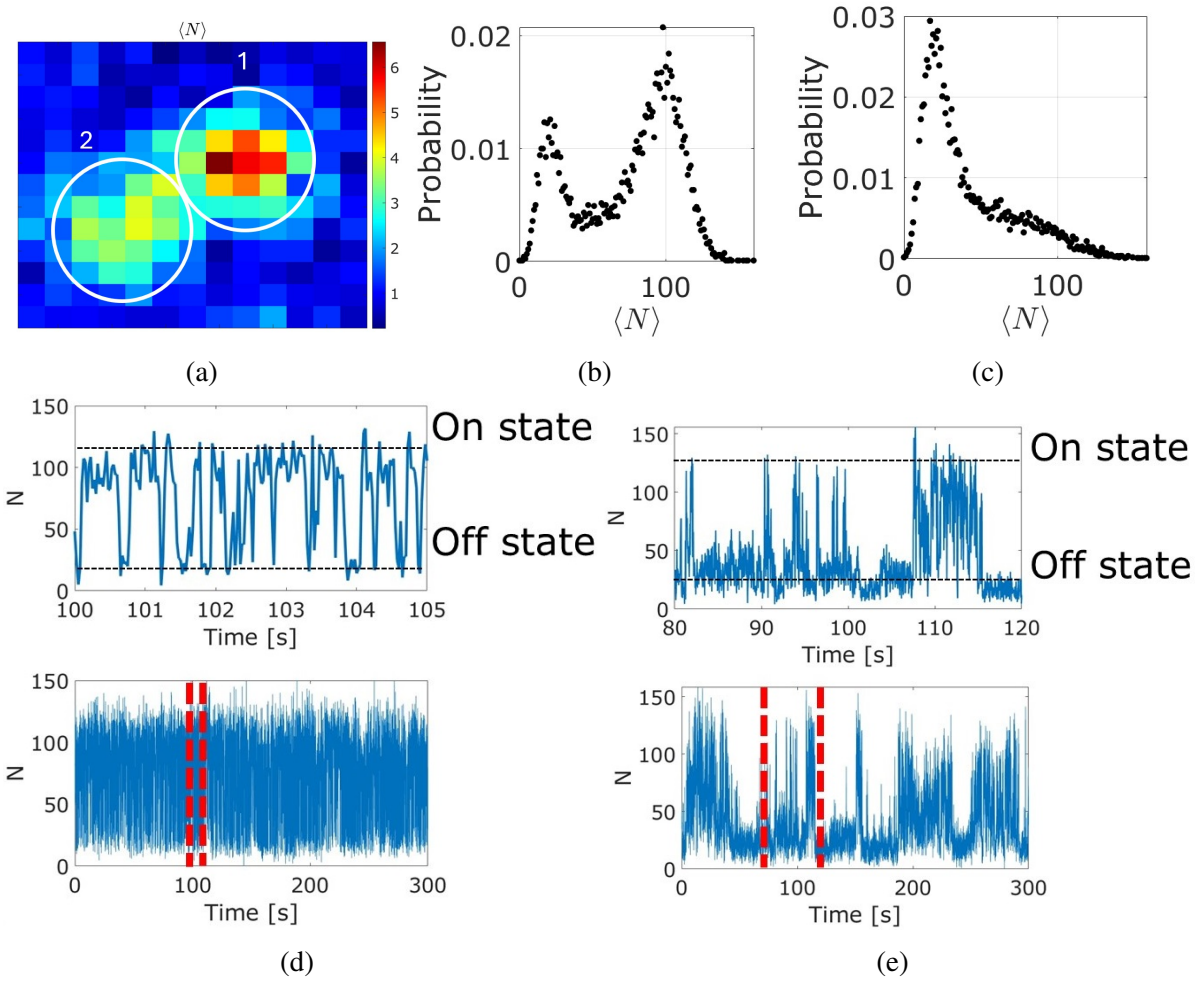

Figure 4.5: *Illustration of independent photon statistics for two closely positioned quantum dots, labeled as 1 and 2. Panel (a) shows the mean photon map, highlighting the emitters. Panels (b) and (c) present the experimental PDFs for emitters 1 and 2, respectively. Panels (d) and (e) display the temporal profiles of the sum of detected photons in the highlighted regions for centers 1 and 2, respectively. To emphasize the distinct On and Off states of the emitter a zoom on a small region is displayed for both the emitters. Data acquisition was performed using a 25 ms exposure time and a 3.6 mW laser power at the objective, with a total of* $12 \cdot 10^3$ *frames stacked.*

Chapter 5

Generalized quantum model of super-resolution

As discussed in Sections 2.2.1 and 2.2.2, super-resolution can be achieved by exploiting sub- and super-Poissonian emitters. However, the mathematical model has been developed only for a limited class of photon sources. In particular, a proper quantum model taking into account the discrete nature of the photons has been developed only for single photon emitters (see Section 2.2.1). For super-Poissonian emitters, used within SOFI, the existing model is classical and fails to incorporate various stochastic fluctuations such as shot noise. This chapter introduces a generalized quantum model developed within the framework of this Ph.D. work, valid for any non-Poissonian emitters, called *Quantum Super-resolution Imaging by Photon Statistics (QSIPS)*. A comparative analysis between QSIPS and the traditional SOFI technique is presented, illustrating the limitations of SOFI and the significant improvements in resolution and stability achieved by the quantum approach, especially in scenarios characterized by low photo-counts per pixel.

5.1 Mathematical Model

Consider N_c photon sources exhibiting uncorrelated emissions and independent temporal statistical fluctuations. Each emitter α-th possesses a probability distribution $P_\alpha(m)$ for emitting m photons within the detector's integration time. Furthermore, let $PSF_\alpha(\mathbf{r}-\mathbf{r}_\alpha) := \eta_\alpha(\mathbf{r})$, representing the probability of detecting a photon emitted by the α-th source at position $\mathbf{r}$ on the detector plane.

The probability $\mathscr{P}_\alpha(n,\mathbf{r})$ of detecting n photons is expressed as follows:

$$\mathscr{P}_\alpha(n,\mathbf{r}) = \sum_{m=n}^{\infty} P_\alpha(m) \binom{m}{n} \eta_\alpha^n(\mathbf{r})[1-\eta_\alpha(\mathbf{r})]^{(m-n)}. \tag{5.1}$$

Given the distributions $P_\alpha(m)$ and $\mathscr{P}_\alpha(n,\mathbf{r})$, we can derive the cumulant generating function, as described in Section 2.2.2, denoted as $\mathscr{C}_\alpha(t)$ and $\mathscr{C}_{\alpha,\eta}(t,\mathbf{r})$, for emitted and detected photons, respectively:

$$\mathscr{C}_\alpha(t) = \log\left(\sum_{m=0}^{\infty} e^{tm} P_\alpha(m)\right), \tag{5.2}$$

$$\mathscr{C}_{\alpha,\eta}(t,\mathbf{r}) = \log\left(\sum_{n=0}^{\infty} e^{tn} \mathscr{P}_\alpha(n,\mathbf{r})\right). \tag{5.3}$$

Equation 5.3 can be expressed using Equation 5.1 as:

$$\begin{aligned}\mathscr{C}_{\alpha,\eta}(t,\mathbf{r}) &= \log\left(\sum_{n=0}^{\infty} e^{tn} \sum_{m=n}^{\infty} P_\alpha(m) \binom{m}{n} \eta_\alpha^n(\mathbf{r})[1-\eta_\alpha(\mathbf{r})]^{(m-n)}\right) \\ &= \log\left(\sum_{m=0}^{\infty} P_\alpha(m)[1-\eta_\alpha(\mathbf{r})+\eta_\alpha(\mathbf{r})e^t]^m\right).\end{aligned} \tag{5.4}$$

The cumulants of any arbitrary order j can be obtained by taking the j-th time derivative of the cumulant generating function and evaluating it at $t=0$, as introduced in Section 2.2.2. Therefore, the j-th cumulant of the emitted and detected photon distribution are respectively:

$$c_\alpha^{(j)} = \frac{d^j \mathscr{C}_\alpha}{dt^j}(t)\Big|_{t=0}, \tag{5.5}$$

$$c_{\alpha,\eta}^{(j)}(\mathbf{r}) = \frac{d^j \mathscr{C}_{\alpha,\eta}}{dt^j}(t,\mathbf{r})\Big|_{t=0}. \tag{5.6}$$

The first three cumulants of both emitted and detected distributions are reported in Table 5.1.

To ensure that the signal from the α-th emitter is proportional only to the j-th power of the PSF we must compute the j-th cumulant of the detected photon distribution and combine it with lower-order cumulants to eliminate terms with lower powers of the PSF that will diminish the maximum achievable resolution enhancement. Specifically, for second and third orders, the linear combinations of cumulants yielding only terms proportional to the second and third power of the PSF are as follows:

	$c_\alpha^{(j)}$	$c_{\alpha,\eta}^{(j)}(\mathbf{r})$
$j=1$	$\langle m\rangle_\alpha$	$\eta_\alpha(\mathbf{r})c_\alpha^{(1)}$
$j=2$	$\langle m^2\rangle_\alpha - \langle m\rangle_\alpha^2$	$\eta_\alpha^2(\mathbf{r})[c_\alpha^{(2)} - c_\alpha^{(1)}] + \eta_\alpha(\mathbf{r})c_\alpha^{(1)}$
$j=3$	$\langle m^3\rangle_\alpha - 3\langle m\rangle_\alpha\langle m^2\rangle_\alpha + 2\langle m\rangle_\alpha^3$	$\eta_\alpha^3(\mathbf{r})[c_\alpha^{(3)} - 3c_\alpha^{(2)} + 2c_\alpha^{(1)}]$ $+3\eta_\alpha^2(\mathbf{r})[c_\alpha^{(2)} - c_\alpha^{(1)}] - 2\eta_\alpha(\mathbf{r})c_\alpha^{(1)}$

Table 5.1: First three cumulants of emitted and detected photon distributions.

$$c_{\alpha,\eta}^{(2)}(\mathbf{r}) - c_{\alpha,\eta}^{(1)}(\mathbf{r}) = \eta_\alpha^2(\mathbf{r})\left[c_\alpha^{(2)} - c_\alpha^{(1)}\right], \tag{5.7}$$

$$c_{\alpha,\eta}^{(3)}(\mathbf{r}) - 3c_{\alpha,\eta}^{(2)}(\mathbf{r}) + 2c_{\alpha,\eta}^{(1)}(\mathbf{r}) = \eta_\alpha^3\left[c_\alpha^{(3)} - 3c_\alpha^{(2)} + 2c_\alpha^{(1)}\right]. \tag{5.8}$$

Beginning with Equations 5.7 and 5.8, we can formulate a comprehensive expression to derive the j-th super-resolved signal from the α-th source ($QSIPS_\alpha^{(j)}$):

$$QSIPS_\alpha^{(j)}(\mathbf{r}) = \eta_\alpha^j(\mathbf{r})\sum_{i=1}^{j}\beta_{i,j}c_\alpha^{(i)} = \sum_{i=1}^{j}\beta_{i,j}c_{\alpha,\eta}^{(i)}(\mathbf{r}), \tag{5.9}$$

where:

$$\beta_{i,j} = \frac{1}{i!}\frac{d^i}{dx^i}\prod_{k=0}^{j-1}(x-k)|_{x=0}. \tag{5.10}$$

Equation 5.9 outlines how to combine cumulants of the detected photon distribution ($c_{\alpha,\eta}^{(i)}(\mathbf{r})$) up to the j-th order to yield a signal from the α-th emitter that is solely proportional to $\eta_\alpha^j(\mathbf{r})$. The coefficient multiplying the j-th power of the PSF, $\sum_{i=1}^{j}\beta_{i,j}c_\alpha^{(i)}$, corresponds precisely to the same combination of cumulants, albeit associated with the emitted photon distribution rather than the detected one. Consequently, each emitter exhibits a distinct scaling factor depending only on its intrinsic temporal fluctuations. Nonetheless, this super-resolution technique does not require any specific prior knowledge regarding the statistical distribution of the emitters; it consistently provides a super-resolved signal for any non-Poissonian emitter. In fact, examining, for instance, Equation 5.7, it becomes evident that the statistical coefficient on the right-hand side is identically zero exclusively for Poissonian light emitters; that is, when $\langle m^2\rangle - \langle m\rangle^2 = \langle m\rangle$.

The derivation of Equations 5.9 and 5.10, along with the demonstration that non-Poissonian statistics of the emitters are required for achieving super-resolution of order j, is detailed in Appendix A.1.

The super-resolution relations reported above pertain to a generic α-th emitter, but the signal detected at a position $\mathbf{r}$ on the detector plane has to be considered a convolution of signals originating from multiple emitters. Specifically, the probability of detecting N photons from N_c independent emitters can be expressed as follows:

$$\mathscr{P}(N,\mathbf{r}) = \prod_{\alpha=1}^{N_c} \sum_{n_\alpha=0}^{\infty} \mathscr{P}_\alpha(n_\alpha,\mathbf{r})\delta_{N,\sum_\alpha n_\alpha}. \tag{5.11}$$

The cumulant generating function of this distribution will be:

$$\begin{aligned}
\mathscr{C}_\eta(t,\mathbf{r}) &= \log\left(\sum_{N=0}^{\infty} e^{tN}\mathscr{P}(N,\mathbf{r})\right) \\
&= \log\left(\sum_{N=0}^{\infty}\prod_{\alpha=1}^{N_c}\sum_{n_\alpha=0}^{\infty} e^{tN}\mathscr{P}_\alpha(n_\alpha,\mathbf{r})\delta_{N,\sum_\alpha n_\alpha}\right) \\
&= \log\left(\prod_{\alpha=1}^{N_c}\sum_{n_\alpha=0}^{\infty} e^{tn_\alpha}\mathscr{P}_\alpha(n_\alpha,\mathbf{r})\right) \\
&= \sum_{\alpha=1}^{N_c}\mathscr{C}_{\alpha,\eta}(\mathbf{r}).
\end{aligned} \tag{5.12}$$

This peculiar property of cumulants implies that for independent emitters, the cumulant generating function of the probability distribution resulting from the convolution of N_c distinct emitters is equivalent to the sum of each individual cumulant generating function. As all cumulants are derived from differentiating the cumulant generating function, the cumulant of a generic order j of the overall system is equal to the sum of the j-th order cumulant of each independent emitter:

$$c_\eta^{(j)}(\mathbf{r}) := \frac{d^j\mathscr{C}_\eta}{dt^j}(t,\mathbf{r})\Big|_{t=0} = \sum_{\alpha=1}^{N_c} c_{\alpha,\eta}^{(j)}(\mathbf{r}). \tag{5.13}$$

As discussed in Section 2.2, a super resolved map of order j can be obtained by summing the j-th power PSF of each distinct emitter contributing to the signal. Equation 5.9 outlines the method for isolating the j-th power of the PSF for the α-th emitter, while Equation 5.13

verifies the complete independence of the cumulants associated with each emitter. This allows for the derivation of a formula for the general super-resolved map of order j ($QSIPS^{(j)}$):

$$QSIPS^{(j)}(\mathbf{r}) := \sum_{i=1}^{j} \beta_{i,j} c_{\eta}^{(i)}(\mathbf{r}) = \sum_{\alpha=1}^{N_c} \eta_{\alpha}^{j}(\mathbf{r}) \sum_{i=1}^{j} \beta_{i,j} c_{\alpha}^{(i)}. \tag{5.14}$$

The coefficient $\sum_{i=1}^{j} \beta_{i,j} c_{\alpha}^{(i)}$, which multiplies the j-th power of the PSF of the α-th emitter, is solely determined by the intrinsic photon statistics of the α-th photon source. This fundamental relationship secures the ability to achieve super-resolution, even when emitters possess different photon statistics. This diversity leads to varying weight factors for the PSF of each emitter, potentially affecting the image's dynamic range, but does not impact the actual super-resolution capability.

While cumulants are also utilized in SOFI, as discussed in Section 2.2.2, it obtains the super-resolved image of order j through the direct evaluation of the j-th order cumulant of the detected photon distribution. QSIPS, however, demonstrates that to effectively remove lower-power components of the PSF from the signal, it is essential to subtract lower-order cumulants using a specific linear combination, ensuring the consistent generation of a super-resolved signal. Moreover, the SOFI technique is applicable solely to photon sources that display super-Poissonian photon statistics, while QSIPS holds for all types of non-Poissonian statistical behaviors.

Albeit SOFI is a classical technique, it is a good approximation of our QSIPS model when the j-th detected cumulant dominates respect to lower order ones. This usually occurs in the presence of a high number of detected photons, which emphasize super-Poissonian signal characteristics.

Section 5.2 presents both simulations and experimental results that demonstrate the superiority of QSIPS over the classical SOFI technique, particularly in low-light conditions.

5.1.1 QSIPS in On-Off detectors

The theoretical framework presented introduces a model capable of detecting photons using a detector that discerns the quantity of photons at specific locations on the detection plane. As detailed in Section 3.2, certain detectors employed in imaging function primarily as On-Off detectors. This configuration precludes direct analysis of photon statistics distributions at particular spatial coordinates. Nonetheless, the super-resolved relationships expressed in terms of cumulants, can be reformulated using higher-order correlation functions.

For instance, the second order super-resolved relation in terms of second order correlation functions is:

$$\begin{aligned} QSIPS^{(2)}(\mathbf{r}) &= c_\eta^{(2)}(\mathbf{r}) - c_\eta^{(1)}(\mathbf{r}) = \langle N^2(\mathbf{r})\rangle - \langle N(\mathbf{r})\rangle^2 - \langle N(\mathbf{r})\rangle \\ &= -\langle N(\mathbf{r})\rangle^2 \left[1 - \frac{\langle N^2(\mathbf{r}) - N(\mathbf{r})\rangle}{\langle N(\mathbf{r})\rangle^2}\right] \\ &= -\langle N(\mathbf{r})\rangle^2 \left[1 - g^{(2)}(0,\mathbf{r})\right], \end{aligned} \tag{5.15}$$

where $N(\mathbf{r})$ refers to the number of the detected photons at a fixed position $\mathbf{r}$ in the detector plane. Following the same approach, we can write the third order super-resolved signal as:

$$\begin{aligned} QSIPS^{(3)}(\mathbf{r}) &= c_\eta^{(3)}(\mathbf{r}) - 3c_\eta^{(2)}(\mathbf{r}) + 2c_\eta^{(1)}(\mathbf{r}) \\ &= \langle N(\mathbf{r})\rangle^3 \left[1 - \frac{3}{2}g^{(2)}(0,\mathbf{r}) + \frac{1}{2}g^{(3)}(0,0,\mathbf{r})\right]. \end{aligned} \tag{5.16}$$

These relationships are the same as those detailed in Section 2.2.1, with the exception of a negative sign in Equation 5.15. This discrepancy arises from the fact that the relations in Section 2.2.1 were derived using sub-Poissonian emitters. However, because these relations can be derived from the QSIPS model, they remain valid even for super-Poissonian statistics.

The ability to represent super-resolved relationships using correlation functions allows for achieving super-resolution with click detectors. Specifically, in a system of j independent On-Off detectors, the j-th correlation function can be approximated based on the probabilities of simultaneous detection events across all j-th On-Off detectors. A comprehensive explanation of this approximation process is provided in Appendix B.1. For instance, the second-order correlation function, evaluated in a system containing two click detectors (A and B), can be approximated as follows [138, 139]:

$$g^{(2)}(0,\mathbf{r}) = \frac{\langle N^2(\mathbf{r}) - N(\mathbf{r})\rangle}{\langle N(\mathbf{r})\rangle^2} \simeq \frac{P_{AB}}{P_A P_B}, \tag{5.17}$$

where P_A and P_B denote the probabilities of click events in detectors A and B, respectively, while P_{AB} is the coincidence probability.

This concept can be generalized to a system comprising j-th detectors, labeled from 0 to $j-1$, as discussed in Appendix B.1. The j-th order correlation function can be approximated as:

$$g^{(j)}(\tau_1 = 0, \tau_2 = 0, \ldots, \tau_{j-1} = 0, \mathbf{r}) = \frac{\left\langle \prod_{i=1}^{j} N(\mathbf{r})\left[N(\mathbf{r}) - i\right] \right\rangle}{\langle N(\mathbf{r})\rangle^j} \simeq \frac{P_{012\ldots j-1}}{\prod_{i=0}^{j-1} P_i}. \tag{5.18}$$

We can write the super-resolved relation of second and third order in a system with On-Off detectors as:

$$QSIPS^{(2)}(\mathbf{r}) = -\langle N(\mathbf{r})\rangle^2 [1 - g^{(2)}(0,\mathbf{r})] \simeq P_A P_B - P_{AB} \tag{5.19}$$

$$\begin{aligned} QSIPS^{(3)}(\mathbf{r}) &= \langle N(\mathbf{r})\rangle^3 \left[1 - \frac{3}{2} g^{(2)}(0,\mathbf{r}) + \frac{1}{2} g^{(3)}(0,0,\mathbf{r})\right] \\ &\simeq \frac{1}{2}(P_{ABC} - (P_A P_{BC} + P_B P_{AC} + P_C P_{AB}) + 2P_A P_B P_C). \end{aligned} \tag{5.20}$$

In practice, the second and third order super-resolved signals can be evaluated by performing respectively the covariance and second-order covariance between the system of On-Off detectors. Generally, we expect that the j-th order super-resolved signal can be expressed in terms of the j-th cross-cumulant between all the On-Off detectors:

$$QSIPS^{(j)}(\mathbf{r}) \simeq k_\eta(C_1, C_2, \ldots, C_j), \tag{5.21}$$

with C_i ($i \in \{1, \ldots, j\}$) being the state of the i-th detector, that can be either 0 (Off) or 1 (On).

Cross-cumulants extend the concept of cumulants to measure joint statistical dependencies between two or more random variables, in this case the state of each of the j detectors. Similar to cumulants, cross-cumulants can be calculated from the cross-cumulant generating function:

$$G(t_1,\ldots,t_j) = \log\left(\left\langle e^{\sum_{i=1}^{j} t_i C_i}\right\rangle\right). \tag{5.22}$$

The cross-cumulant of order j is calculated by differentiating the cross-cumulant generating function with respect to the parameters t_i, for $i \in \{1,\ldots,j\}$ at $t_i = 0$:

$$k_\eta(C_1,C_2,\ldots,C_j) = \frac{d^j}{dt_1\cdots dt_j} G(t_1,\ldots,t_j)\bigg|_{t_1=\cdots=t_j=0}. \tag{5.23}$$

In general, the j-th order super-resolved signal in a system of j On-Off detectors will be a function of the click probabilities P_i of each detector, as well as on all coincidence probabilities from order 2 up to j:

$$QSIPS^{(j)} \simeq f(P_0,\ldots,P_{j-1},P_{01},\ldots,P_{0j-1},P_{012},\ldots,P_{01j-1},\ldots,P_{01\ldots j-1}). \tag{5.24}$$

We remind that each of these probabilities can be expressed in terms of the emitted photon distributions $P(m)$, before accounting for binomial losses, and are dependent on the detectors' detection probabilities η_i, as discussed in Appendix B.1.

5.2 QSIPS vs SOFI

The key disparity between QSIPS and the SOFI technique, described in Section 2.2.2, lies in its classical nature. The absence of consideration for shot noise in the SOFI renders it unsuitable under low light-level conditions. Specifically, the expressions for the j-th order super-resolved signal in SOFI considering N_c independent emitters is:

$$SOFI^{(j)}(\mathbf{r}) := c_\eta^{(j)} = \sum_{\alpha=1}^{N_c} c_{\alpha,\eta}^{(j)}(\mathbf{r}). \tag{5.25}$$

Due to the omission of subtracting lower order cumulants, terms proportional to lower power of the PSF emerge in the SOFI classical technique, thereby limiting the achievable super-resolution. To demonstrate this clearly, the first two orders of super-resolution in both the SOFI and QSIPS models are presented as follows:

$$SOFI^{(2)}(\mathbf{r}) = \sum_{\alpha=1}^{N_c} \left(\eta_\alpha^2(\mathbf{r})[c_\alpha^{(2)} - c_\alpha^{(1)}] + \eta_\alpha(\mathbf{r}) c_\alpha^{(1)} \right), \tag{5.26}$$

$$QSIPS^{(2)}(\mathbf{r}) = \sum_{\alpha=1}^{N_c} \eta_\alpha^2(\mathbf{r})[c_\alpha^{(2)} - c_\alpha^{(1)}], \tag{5.27}$$

$$SOFI^{(3)}(\mathbf{r}) = \sum_{\alpha=1}^{N_c} \left(\eta_\alpha^3(\mathbf{r})[c_\alpha^{(3)} - 3c_\alpha^{(2)} + 2c_\alpha^{(1)}] + 3\eta_\alpha^2(\mathbf{r})[c_\alpha^{(2)} - c_\alpha^{(1)}] - 2\eta_\alpha(\mathbf{r}) c_\alpha^{(1)} \right), \tag{5.28}$$

$$QSIPS^{(3)}(\mathbf{r}) = \sum_{\alpha=1}^{N_c} \eta_\alpha^3(\mathbf{r})[c_\alpha^{(3)} - 3c_\alpha^{(2)} + 2c_\alpha^{(1)}]. \tag{5.29}$$

From the case $j = 2$ in Equation 5.26, it is clear that only subtracting the shot noise term proportional to $\langle N \rangle = \sum_{\alpha=1}^{N_c} \eta_\alpha(\mathbf{r}) c_\alpha^{(1)}$, i.e. the first order cumulant of the detected photon distribution, allows to get rid of the first power of $\eta_\alpha(\mathbf{r})$ in the super-resolved signal.

An experimental demonstration of the robustness of QSIPS, in comparison to classical SOFI, was conducted using the optical setup described in Chapter 4. For each pixel in the collected data, temporal cumulants were calculated and utilized to generate both classical and quantum super-resolved images. Additionally, Fourier interpolation and filtering were applied to minimize pixelation effects. Figure 5.1 displays the mean intensity image along with the first four orders of super-resolved images using both the SOFI and the QSIPS techniques, showcasing a small cluster of blinking emitters.

It is evident the increase in resolution provided by QSIPS compared to the one obtained with SOFI, due to the presence in the classical model of lower orders of the PSF that reduce the maximum achievable resolution enhancement. In particular, the visibility of each one-dimensional plot shown in Figure 5.1c can be calculated using the following formula:

$$V = \frac{I_{\max} - I_{\min}}{I_{\max} + I_{\min}}, \tag{5.30}$$

where $I_{\max}$ represents the mean value of the peaks and $I_{\min}$ denotes the value of the minima. By averaging the visibility estimates from the three different measurements for both quantum and classical signals, we obtain the following results: $V_{QSIPS^{(4)}} = (40 \pm 1)\%$ and $V_{SOFI^{(4)}} = (12 \pm 1)\%$, confirming the resolution enhancement provided by the QSIPS model.

Furthermore, a simulated study over two close identical blinking quantum dots, whose PDF is detailed in Section 6.1, was performed in order to assess the dependence of the visibility from the mean number of detected photon, as reported in Figure 5.2. We considered a matrix of noiseless linear detectors in which the detection of photons by each pixel was modeled using a binomial distribution, where the number of trials corresponds to the emitted photons from

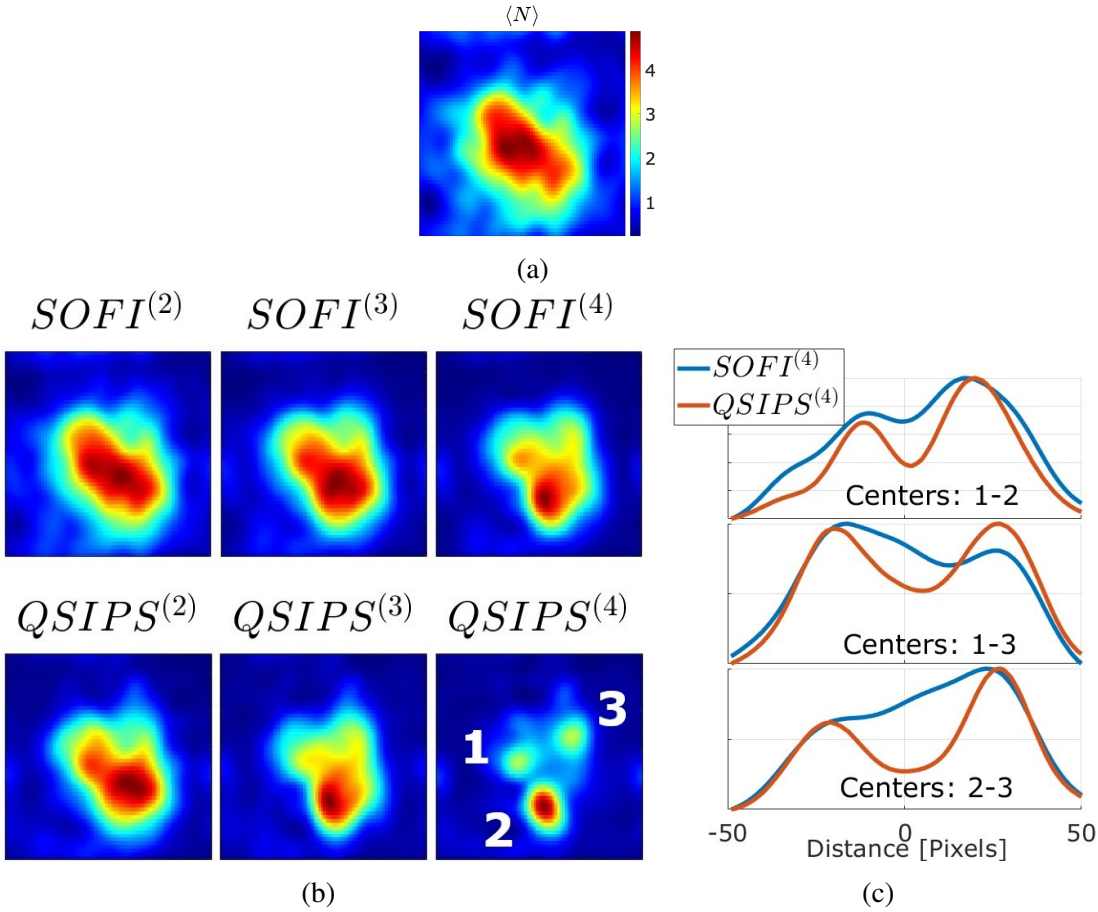

Figure 5.1: *Experimental comparison between the SOFI and the QSIPS methods under low light level conditions. Panel (a) displays the intensity image of a small cluster of quantum dots, captured with an exposure time of 20 ms, where the output power before the objective was 1.4 mW, and a total of* $53 \cdot 10^3$ *frames were acquired. Panel (b) illustrates the absolute value of the first four super-resolution orders, where the top part showcases classical SOFI, and the bottom part depicts QSIPS technique. Panel (c) presents a one-dimensional plot of the normalized fourth-order super-resolved signals measured along the conjunction of each pair among the three centers identified in panel (b), comparing the results from both techniques. The images were Fourier interpolated to minimize pixelation effects and Gaussian filtered to mitigate artifacts and manage noise.*

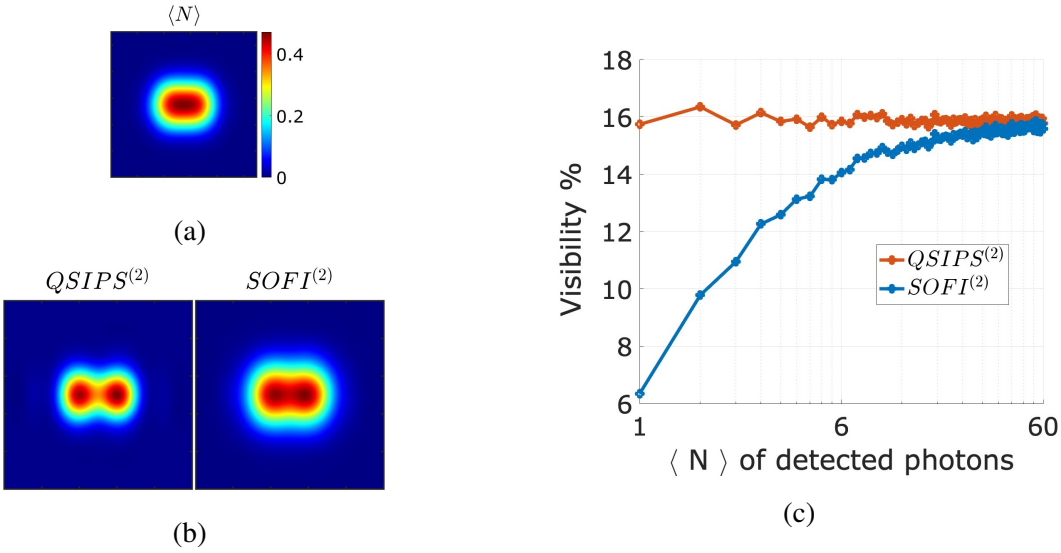

Figure 5.2: *Visibility vs number of detected photons for two simulated identical blinking quantum dots closer than the minimum resolvable distance. Panel (a) showcase the mean intensity map. Panel (b) displays the second order super resolved maps of both the classical SOFI and the QSIPS techniques in low light condition (i.e. mean number of detected photons in the conjunction between the emitters of $\langle N \rangle = 0.4$). Panel (c) displays the actual visibility of the region between the emitters as a function of the detected number of photons. The simulated PDF of the emitter was considered with a blinking probability b = 0.7 and the simulations were performed changing the number of excitation cycles K from 10^2 to 10^4 (see Section 6.1 for more details). The simulations considered an optical system with 95% optical losses, excluded the effect of the PSF, and involved stacking $100 \cdot 10^3$ frames. The images were Fourier interpolated to minimize pixelation effects.*

the source, and the success probability is determined by the product of the PSF and the total optical losses. These individual images were then compiled to create a composite classical intensity image. This is possible because we only consider independent and incoherent sources. Additionally, super-resolution maps were generated by independently applying the cumulant operation to each pixel, utilizing both the QSIPS and the SOFI techniques.

Specifically, it is observed that QSIPS maintains a consistent visibility value across all illumination conditions. In contrast, the visibility achieved by the classical SOFI technique increases with the number of detected photons, eventually converging to the value predicted by the QSIPS model.

Additionally, we can assess the dependence of the spatial standard deviation (σ) of the effective PSF on the detected light levels using both the classical and the quantum techniques. Consequently, an experimental analysis was conducted on a single quantum dot for two different exposure times of the detector, as shown in Figure 5.3a and 5.3b respectively. A two-dimensional Gaussian fit was applied to the effective PSF of each super-resolution order. From this fit, the standard deviation was determined by calculating the mean value of the

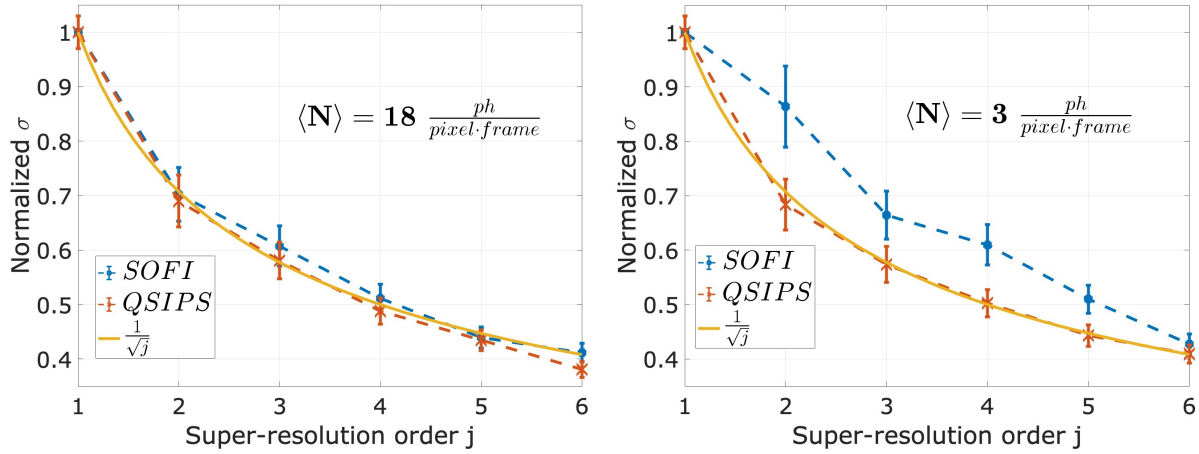

(a) (b)

Figure 5.3: *Effective PSF spatial standard deviation (σ) in function to the super-resolution order, for a single quantum dot under two light level conditions: (a) $\langle N \rangle = 18$ ph/pixel/frame obtained with a 200 ms exposure time, and (b) $\langle N \rangle = 3$ ph/pixel/frame with a 50 ms exposure time, utilizing both the SOFI and the QSIPS techniques. The theoretical behavior is also reported (continuous line), for comparison. The y-axis displays the spatial standard deviation of the effective PSF for different super-resolution orders (x-axis), each normalized to the one obtained in the intensity image.*

estimates along the two dimensions of the image. This value was subsequently normalized by the one obtained from the intensity map and compared with the theoretical prediction of $1/\sqrt{j}$.

The enhancement in super-resolution achieved through QSIPS, as compared to classical SOFI, is predominantly influenced by the relative magnitude of the j-th order cumulant within the linear combinations delineated in Equations 5.9 and 5.10. The significance of the j-th order cumulant, in that combination, is related to the specific photon distribution of the emitter. For that, it may occasionally happen that certain super-resolved images generated using SOFI might correspond closely with those produced by QSIPS, when the j-th cumulant magnitude dominates.

However, super-resolution in QSIPS is always optimized and predictable at the varying of the order j, demonstrating enhanced reliability in the produced images. This is again attributed to the fact that the effective PSF of each emitter is not dependent on the particular photon statistics of the source when QSIPS is used.

Furthermore, QSIPS retains its applicability even under quasi-Poissonian emission conditions. When multiple clusters of quantum dots are present, the aggregate emission from each cluster approximates Poissonian statistics. Under such circumstances, the magnitude of j-th order cumulant typically aligns with the one of the preceding cumulants. This similarity in orders makes it challenging for classical SOFI techniques to discriminate between different clusters of emitters effectively.

Another distinction between QSIPS and classical SOFI lies in the management of high dynamic range. In particular, it may happen that some emitters are almost suppressed in the super-resolved maps due to the characteristics of their emission probability distribution, and other emitters, that are barely visible in the intensity map can be drastically enhanced in magnitude. This variability significantly impacts the dynamic range of highly super-resolved images in SOFI, but it is mitigated in QSIPS.

Figure 5.4 presents an experimental acquisition of a cluster of quantum dots, depicting both the mean image value and the super-resolution up to the fourth order using both the SOFI and the QSIPS techniques. Notably, the high dynamic range characteristic of SOFI tends to obscure low-intensity blinking emitters, particularly evident in the emitter highlighted in Figure 5.4b. In contrast, our approach, which incorporates lower order cumulants, seems to compress the effective dynamic range of the super-resolved images, as can be noticed from the visibility enhancement of the circled emitter in the quantum super-resolved maps, compared to the classical ones.

A possible explanation of this phenomenon can be considered by examining a situation in which photons from two distinct emitters are collected at the position $\mathbf{r}$ on the detector plane. The j-th order cumulant of the overall detected photon distribution, that coincides with the j-th order SOFI, will be:

$$\begin{aligned} SOFI^{(j)}(\mathbf{r}) =& c^{(j)}_{1,\eta}(\mathbf{r}) + c^{(j)}_{2,\eta}(\mathbf{r}) = \\ & (a_j \eta_1^j(\mathbf{r}) + a_{j-1}\eta_1^{j-1}(\mathbf{r}) + ...) + (b_j \eta_2^j(\mathbf{r}) + b_{j-1}\eta_2^{j-1}(\mathbf{r}) + ...), \end{aligned} \tag{5.31}$$

where a_i and b_i, with $i \in \{1, \ldots, j\}$,are set of coefficients depending the emitter photon statistics distribution, deriving from the cumulant generating function reported in Equation 5.4. Instead, the j-th super-resolved signal from QSIPS assumes the simpler form:

$$QSIPS^{(j)}(\mathbf{r}) = a_j \eta_1^j(\mathbf{r}) + b_j \eta_2^j(\mathbf{r}). \tag{5.32}$$

Thus, QSIPS simplifies the scenario by retaining only the higher order of the effective PSFs, with the related coefficients a_j and b_j. This modification effectively reduce the dynamic range, enhancing the utility of the model in practical imaging applications where emitter statistics may vary. As support to this hypothesis, a study over a series of simulated images is reported in Figure 5.5, considering two blinking quantum dots with different photon statistics. The simulative approach is the same as the one described for the visibility analysis reported in Figure 5.2. Here, it is evident that the variability in the relative signal between the two emitters is reduced when considering QSIPS technique, in comparison to classical SOFI.

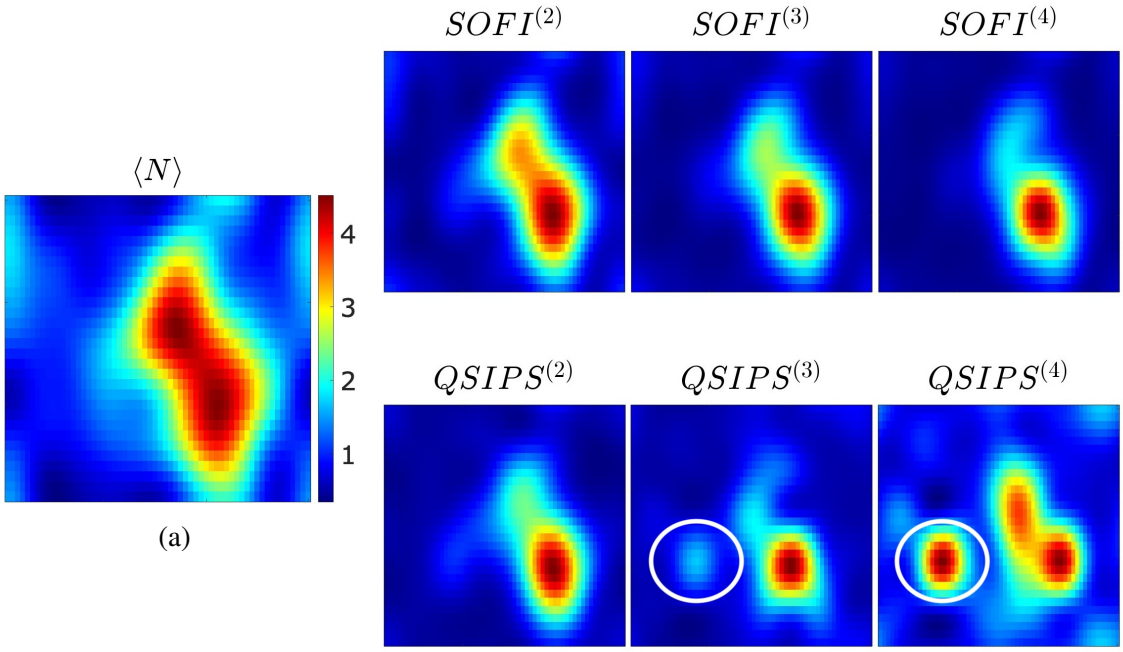

Figure 5.4: *Experimental comparison of dynamic range between SOFI and QSIPS under low light level conditions. Panel (a) displays the intensity image of a small cluster of quantum dots, captured with a 3 ms exposure time, where the output power before the objective was 1.1 mW, and a total of* $40 \cdot 10^3$ *frames were acquired. Panel (b) illustrates the absolute value of first four super-resolution orders; the upper part showcases the classical SOFI technique, while the lower part depicts the QSIPS method. The images underwent Fourier interpolation to reduce pixelation effects and were Gaussian filtered to manage noise and prevent artifacts.*

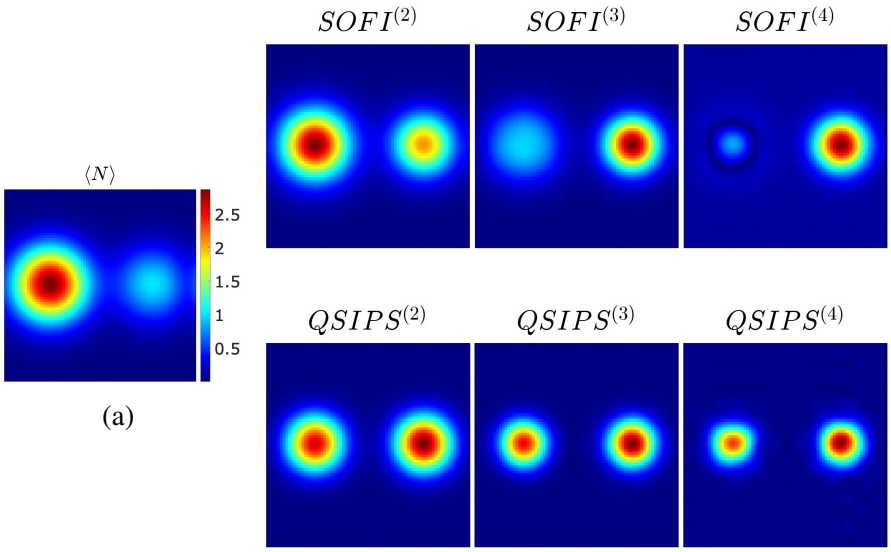

Figure 5.5: *Simulated comparison of dynamic range between SOFI and QSIPS under low light conditions. Panel (a) shows an intensity image of two quantum dots, each with different blinking probabilities: $b = 0.25$ for the left and $b = 0.75$ for the right emitter (see Section 6.1 for more details). The simulations considered an optical system with 95% optical losses, excluded the effect of the PSF, and involved stacking $50 \cdot 10^3$ frames. Panel (b) displays the absolute values of the first four super-resolution orders; the upper section features the classical SOFI technique, while the lower section depicts the QSIPS method. The images were Fourier interpolated to minimize pixelation effects.*

The theoretical analysis, the experimental results and simulations presented in this section affirm the effectiveness of our proposed technique under low-light conditions in which shot noise is not negligible, demonstrating superior performance in achieving super-resolution compared to the traditional SOFI technique.

While SOFI remains a viable approach for dealing with super-Poissonian emitters under high-brightness conditions, the model introduced in this chapter offers a more comprehensive solution. QSIPS accounts for shot noise and photon statistics more accurately, providing a reliable method for achieving super-resolution across all brightness conditions. It presents a detailed and systematic way to combine the cumulants of the detected distribution, maximizing resolution enhancement by any non-Poissonian statistics beyond the typical super-Poissonian statistics utilized by SOFI. Notably, the development of an extensive quantum model is crucial for super-resolution in low-light scenarios. In particular, our work is prompted by advancements in wide-field super-resolution detector technologies, which are increasingly yielding faster, lower-noise detectors crucial for non-invasive, low-light biological imaging.

Chapter 6

Extensive analysis of the Signal-to-Noise Ratio

In the previous chapter, we introduced the QSIPS model aimed at achieving super-resolution with any non-Poissonian emitters. However, this approach requires the evaluation of high-order cumulants in the detected photon distribution, typically leading to prolonged acquisition times.

In this chapter, we shift our focus to analyzing the SNR of the super-resolved signal originating from single photon emitters that can exhibit blinking behavior. This analysis is relevant to two distinct types of single-photon sources utilized in biological fluorescence imaging applications: color centers and blinking quantum dots. Our objective is to provide a guide to assess the best detection schemes, photon sources, and experimental parameters, aiming to reduce the overall data volume and acquisition time.

Specifically, the first part of this chapter presents a generalized model of the PDF of single photon emitters that can show blinking behavior. Subsequently, a general mathematical description to assess the SNR of the super-resolved signals from a single emitter is proposed. An extensive analysis of the SNR as a function of experimental parameters is then reported for detection schemes employing both linear and On-Off detectors, including simulations of super-resolved images.

The discussion presented here refers to a generic α-th photon source, whose emission is detected at position $\mathbf{r}$ on the detector plane, a dependence that will not be explicitly reiterated in the following sections. Additionally, the SNR under consideration is for a single acquisition; to obtain the actual experimental SNR, it must be scaled by $\sqrt{N_f}$, where N_f represents the number of independent images acquired.

6.1 Model of the PDF

In this section we will propose a general model of the detected PDF from a single photon emitter that possesses a certain probability b of emitting non-radiatively upon an excitation cycle, in order to take into account both blinking quantum dots and more stable emitters such as color centers in high band gap semiconductors.

The state $|\psi\rangle$ of an ideal single photon emitter undergoing K independent excitation cycles can be expressed as the tensor product of K single-photon temporal modes:

$$|\psi\rangle = \otimes_{t=1}^{K} |1\rangle_t, \tag{6.1}$$

where t represents the index temporal interval at which the single photon is emitted.

Since typical detection systems are not able to resolve all the temporal modes, the probability of m photons arriving at the detection plane will be:

$$P(m) = \delta_{m,K}. \tag{6.2}$$

We can take in account the fact that the emitter can possess a non-radiative state, a situation typically achieved in quantum dots. In particular, we can modify Equation 6.2 as:

$$P(m) = b\delta_{m,0} + (1-b)\delta_{m,K}. \tag{6.3}$$

However, the detected photon statistics is strongly determined by the integration time of the detector, in relation to the typical switching time τ_b of the blinking emitter between the On and Off states, and vice versa.

Let us consider that in the integration time of the detector T the blinking emitter performs M transitions between the two states, such that $M = T/\tau_b$.

The probability of having j of the M intervals in which the emitter is in the Off state follows a Binomial distribution, denoted as $\mathscr{B}(j/M,b)$, with M trials and probability of success b:

$$\mathscr{B}(j/M,b) = \binom{M}{j} b^j (1-b)^{(M-j)}. \tag{6.4}$$

We consider that within the total integration time T of the detector, the emitter undergoes K excitation cycles. Therefore, in each short interval time τ_b in which the emitter is in the On state, it will perform K/M excitation cycles.

The probability of having m photons emitted in the time T given j Off time windows is:

$$P(m/j,b,K) = \delta_{m,(M-j)\frac{K}{M}}. \tag{6.5}$$

The overall probability density function $P(m)$ is obtained by summing over all possible j:

$$P(m) = \sum_{j=0}^{M} \mathscr{B}(j/M, b)\delta_{m,(M-j)\frac{K}{M}}. \tag{6.6}$$

It can be noticed that by putting $b = 0$ in Equation 6.6 we return to Equation 6.2, while putting $M = 1$, i.e. the integration time of the detector is already fast enough to discern the On and Off states of the emitter, we return to Equation 6.3. Considering the system's non-unitary detection probability, denoted by η, the overall probability of detecting n photons is:

$$\begin{aligned}
\mathscr{P}(n) &= \sum_{m=0}^{\infty} P(m)\binom{m}{n}\eta^n(1-\eta)^{(m-n)} \\
&= \sum_{m=0}^{\infty}\sum_{j=0}^{M} \mathscr{B}(j/M, b)\binom{m}{n}\eta^n(1-\eta)^{(m-n)}\delta_{m,(M-j)\frac{K}{M}} \\
&= \sum_{j=0}^{M} \mathscr{B}(j/M, b)\binom{K\left(1-\frac{j}{M}\right)}{n}\eta^n(1-\eta)^{\left[K\left(1-\frac{j}{M}\right)-n\right]} \\
&= \sum_{j=0}^{M} \mathscr{B}(j/M, b)\mathscr{B}\left(n/K\left(1-\frac{j}{M}\right), \eta\right).
\end{aligned} \tag{6.7}$$

For $M = 1$, there are two possible outcomes: the emitter either emits K photons or none within a single exposure time of the detector. Additionally, if the emitter is in the On state, the detected probability distribution is broadened by the non-unitary detection efficiency of the system (Figure 6.1a). For $M = 2$, there are three possible outcomes within a single exposure time: firstly, the emitter is always in the On state (resulting in a peak centered at $K\eta$ in Figure 6.1b); secondly, the emitter is in the On state half the time and in the Off state the other half (peak centered at $K\eta/2$ in Figure 6.1b); thirdly, the emitter is always in the Off state (peak at 0 in Figure 6.1b). As M increases, the number of possible levels increases correspondingly. However, these levels become indistinguishable due to dispersion caused by the detection efficiency (Figures 6.1c and 6.1d).

In the slow detection limit where $M \to \infty$, i.e. $T \gg \tau_b$, the detected PDF converges to:

$$\lim_{M\to\infty} \mathscr{P}(n) = \lim_{M\to\infty}\left[\sum_{j=0}^{M} \mathscr{B}(j/M, b)\mathscr{B}\left(n/K\left(1-\frac{j}{M}\right), \eta\right)\right] = \mathscr{B}(n/K(1-b), \eta), \tag{6.8}$$

where we have used the following properties:

$$\sum_{j=0}^{\infty} \mathscr{B}(j/M, b) = 1, \tag{6.9}$$

$$b = \lim_{M\to\infty} \frac{j}{M}. \tag{6.10}$$

Equation 6.8 demonstrates that when observing blinking single-photon emitters with a slow detector (i.e., high exposure time respect to the switching time τ_b), the overall detected statistics resemble those of a binomial distribution, which shows sub-Poissonian fluctuations. The number of trials is $K(1-b)$, a fraction of the total excitation cycles, and the success probability is η.

The conditions under which the emitted photon distributions, as presented in Equation 6.6, exhibits super-Poissonian characteristics can be analyzed using the Fano factor. It is defined as the ratio of the variance of the distribution to its mean value:

$$F_{\text{emitted}} = \frac{\langle m^2\rangle - \langle m\rangle^2}{\langle m\rangle} = \frac{Kb}{M}. \tag{6.11}$$

Clearly, by definition, it is $F_{\text{emitted}} = 1$ for Poissonian photon statistics, while for super(sub)-Poissonian statistics it is $F_{\text{emitted}} > 1 (< 1)$. In particular, for the photon statistics in Equation 6.6 the super-poissonian condition is $K > M/b$. On the other side, it should be noted that for $b = 0$ we have $F_{\text{emitted}} = 0$ for every value of K . The case $b = 0$ represents a non-blinking emitter, resulting always in a sub-Poissonian detected photon statistics.

Nevertheless, the Fano factor of the detected photon distribution reported in Equation 6.7, denoted by F_{detected}, is expressed as follows:

$$F_{\text{detected}} = \frac{\langle n^2\rangle - \langle n\rangle^2}{\langle n\rangle} = 1 - \eta\left(1 - \frac{Kb}{M}\right). \tag{6.12}$$

Here, it should be noted that although F_{detected} is dependent on the detection efficiency η, the condition under which super-Poissonian behavior emerges, specifically when $F_{\text{detected}} > 1$, is given by $K > \frac{M}{b}$, which is identical to the condition for the emitted distribution.

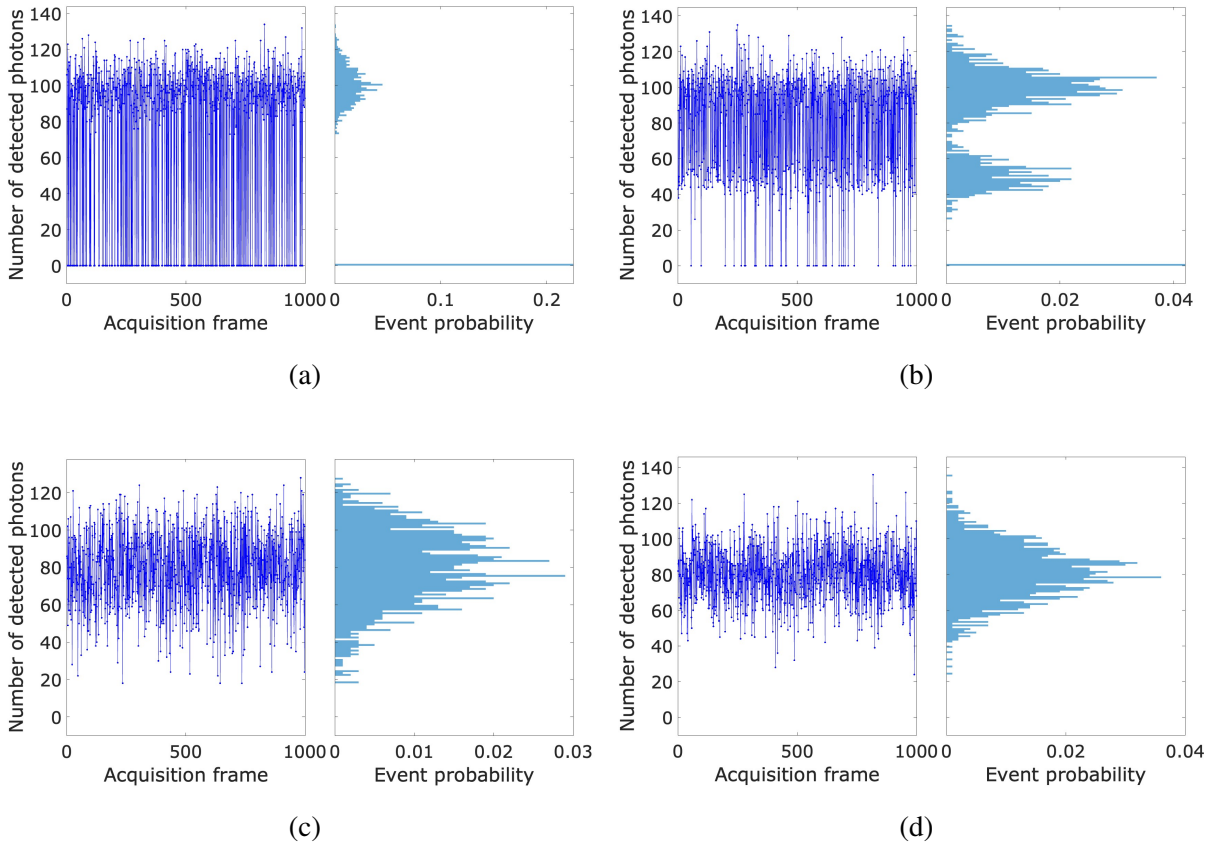

Figure 6.1: *Simulation of 1000 samples extracted from the detected photon distribution as described in Equation 6.7, and their histograms representation with varying values of the parameter M: (a)* $M = 1$*, (b)* $M = 2$*, (c)* $M = 5$*, and (d)* $M = 10$*. The simulation parameters are* $\eta = 0.01$*,* $b = 0.25$*, and* $K = 10^4$*.*

6.2 Evaluation of the SNR

To evaluate the SNR of the super-resolved signal, it is beneficial to express the cumulants of the detected photon distribution in terms of combinations of the raw moments $\mu'_k = \langle n^k \rangle$, utilizing partial Bell polynomials (described in Appendix A.1):

$$c_\eta^{(j)} = \sum_{i=1}^{j} (-1)^{(i-1)} (i-1)! B_{j,i}(\mu'_1, ..., \mu'_{j-i+1}). \tag{6.13}$$

Specifically, the expressions for the second and third order super-resolved signals in terms of raw moments are:

$$QSIPS^{(2)} = c_\eta^{(2)} - c_\eta^{(1)} = \langle n^2 \rangle - \langle n \rangle^2 - \langle n \rangle, \tag{6.14}$$

$$\begin{aligned} QSIPS^{(3)} &= c_\eta^{(3)} - 3c_\eta^{(2)} + 2c_\eta^{(1)} = \\ &= 2\langle n \rangle^3 + 3\langle n \rangle^2 + 2\langle n \rangle - 3\langle n \rangle \langle n^2 \rangle - 3\langle n^2 \rangle + \langle n^3 \rangle. \end{aligned} \tag{6.15}$$

The general expression for the SNR of the j-th order super resolved signal (labeled as $SNR^{(j)}$) is:

$$SNR^{(j)} = \frac{QSIPS^{(j)}}{\sqrt{\sum_{\alpha=1}^{j} \sum_{\beta=1}^{j} \frac{\partial QSIPS^{(j)}}{\partial \mu'_\alpha} \frac{\partial QSIPS^{(j)}}{\partial \mu'_\beta} Cov(n^\alpha, n^\beta)}}, \tag{6.16}$$

with:

$$Cov(n^\alpha, n^\beta) = \mu'_{\alpha+\beta} - \mu'_\alpha \mu'_\beta. \tag{6.17}$$

The derivative of the super-resolves signal respect to the α-th raw moment can be evaluated as:

$$\begin{aligned} \frac{\partial QSIPS^{(j)}}{\partial \mu'_\alpha} &= \sum_{i=0}^{j} \beta_{i,j} \frac{\partial c_\eta^{(i)}}{\partial \mu'_\alpha} = \sum_{i=0}^{j} \beta_{i,j} \sum_{k=1}^{i} (-1)^{(k-1)} (k-1)! \frac{\partial B_{i,k}(\mu'_1, ..., \mu'_{i-k+1})}{\partial \mu'_\alpha} \\ &= \sum_{i=0}^{j} \beta_{i,j} \sum_{k=1}^{i} (-1)^{(k-1)} (k-1)! \binom{i}{\alpha} B_{i-\alpha,k-1}(\mu'_1, ..., \mu'_{i-k-\alpha+2}), \end{aligned} \tag{6.18}$$

with $\beta_{i,j}$ being the coefficient reported in Equation 5.10 and where we have exploited the relation:

$$\frac{\partial B_{i,k}(\mu'_1,...,\mu'_{i-k+1})}{\partial \mu'_\alpha} = \binom{i}{\alpha} B_{i-\alpha,k-1}(\mu'_1,...,\mu'_{i-k-\alpha+2}). \tag{6.19}$$

The QSIPS model applies also to On-Off detectors, as discussed in Section 5.1.1, therefore we can also evaluate the SNR in this case. Specifically, as stated in Equation 5.21, the super-resolution of order j is approximated by the j-th cross-cumulant of click events across j detectors. Therefore, its SNR can be expressed as:

$$SNR^{(j)} = \frac{QSIPS^{(j)}}{\sqrt{\sum_{\mathscr{A}}\sum_{\mathscr{B}} \frac{\partial QSIPS^{(j)}}{\partial P_{\mathscr{A}}} \frac{\partial QSIPS^{(j)}}{\partial P_{\mathscr{B}}} Cov(C_{\mathscr{A}}, C_{\mathscr{B}})}}, \tag{6.20}$$

where $P_{\mathscr{A}}$ and $P_{\mathscr{B}}$ represent the indices of click probabilities and coincidences up to the j-th order as appearing in Equation 5.24, while $C_{\mathscr{A}}$ and $C_{\mathscr{B}}$ indicate the state of the detectors (On $= 1$, Off $= 0$). The term $Cov(C_{\mathscr{A}}, C_{\mathscr{B}})$ can be written, considering $C_i^2 = C_i$ due to $C_i \in \{0,1\}$, as:

$$Cov(C_{\mathscr{A}}, C_{\mathscr{B}}) = P_{\mathscr{A}\cup\mathscr{B}} - P_{\mathscr{A}} P_{\mathscr{B}}. \tag{6.21}$$

For instance, $Cov(C_{01}, C_2) = P_{012} - P_{01}P_2$, whereas $Cov(C_{01}, C_1) = P_{01} - P_{01}P_1$, since $C_1^2 = C_1$, with $C_{01} = C_0 C_1$.

6.3 SNR of super-resolved signals from not blinking single-photon emitters

Some classes of solid-state photon sources, such as the NV centers described in Section 1.2.2, are observed to behave like single photon emitters exhibiting non-blinking behavior, especially in the non-saturation regime [140, 141].

The distributions of emitted and detected photons of a single photon emitter are obtained by substituting $b = 0$ in Equations 6.6 and 6.7 respectively, yielding the following relationships:

$$P(m) = \delta_{m,K}, \tag{6.22}$$

$$\mathscr{P}(n) = \mathscr{B}(n/K, \eta). \tag{6.23}$$

We can calculate the cumulants of both distributions using Equation 5.2 and Equation 5.3, respectively. However, as suggested by Equation 5.4, knowing the emitted photon distribution and the detection probability η is sufficient to retrieve the cumulants of the detected photon

distribution. Subsequently, we can substitute the cumulants in Equation 5.9 and obtain the relation of the super-resolved signal of order j as:

$$QSIPS^{(j)} = \eta^j \sum_{i=1}^{j} \beta_{i,j} c^{(i)} = (j-1)!\eta^j K, \tag{6.24}$$

where we have used that:

$$c^{(i)} = K\delta_{i,1}, \tag{6.25}$$

$$\beta_{1,j} = (j-1)!. \tag{6.26}$$

Even though the super-resolved signal scales proportionally to the number of excitation cycles K executed during the detector's integration time for every order j, its SNR is influenced by a complex interaction between detection probability and the number of excitation cycles. Therefore a compact expression describing its dependence on K and η for an arbitrary super-resolution order j is not feasible. For simplicity, we report here explicitly the expression with $j = 2$:

$$SNR^{(2)} = \frac{\sqrt{K}\eta}{\sqrt{2(1-\eta)(3\eta - 1 + K(1-\eta))}}. \tag{6.27}$$

The $SNR^{(j)}$ with $j = 2, \ldots, 5$ are reported graphically in Figures 6.2a and 6.2b as a function of K and η, respectively. As one may appreciate from Figure 6.2a, the optimal SNR for any j is achieved when $K = 1$. In fact, it can be shown that the following simple expression holds for any order j:

$$SNR^{(j)}|_{K=1} = \frac{1}{j}\sqrt{\frac{\eta}{1-\eta}}. \tag{6.28}$$

Thus for single-photon emitters, it is advantageous to limit the number of excitations to only one cycle per integration period. Note that up to now we have not yet considered the noise of the detector (only its quantum efficiency included in η). In case of noisy detector the optimal number of cycles may be different.

Additionally, an interesting case arises in the limit as $K \to \infty$, a scenario typical in slow wide-field linear detectors, like CCDs and CMOSs cameras, where the characteristic lifetime of the emission is significantly shorter than the exposure time of the detector. In particular, we obtain:

$$\lim_{K\to\infty} SNR^{(2)} = \frac{1}{\sqrt{2}}\frac{\eta}{1-\eta}, \tag{6.29}$$

$$\lim_{K\to\infty} SNR^{(j)}\big|_{j>2} = 0. \tag{6.30}$$

This outcome indicates that a non-zero second-order super-resolution signal is achievable even with a high number of excitation cycles K. The expression in Equation 6.29 represents the value reached by the plateau of the light-blue curve in Figure 6.2a. Consequently, this makes it feasible to perform second-order super-resolved images even using single photon emitters employing linear detection schemes characterized by long exposure times. Conversely, for higher orders ($j > 2$), the SNR approaches zero, suggesting that a substantial increasing of statistical data are required to obtain reliable super-resolved signals.

This behavior is also shown in Figures 6.3b and 6.3c, where the images of three close emitters with different values of K are compared across the first five super-resolution orders. A meaningful super-resolved map is achieved for a large number of number excitation cycles ($K = 1000$) only for $j = 2$.

In the context of On-Off detectors, as specified in Equation 5.21, it remains feasible to approximate the super-resolved signal of order j and evaluate its SNR using Equation 6.20. In this framework, a system of j On-Off detectors arranged in a tree structure (illustrated in Figure B.1) is considered, where detectors are assumed with equal detection probability, $\eta_i = \eta$ ($i \in \{1,\dots,j\}$), accounting for optical losses and the effect of the PSF.

The SNR of the first five super-resolution orders as functions of K and η are reported in Figures 6.2c and 6.2d for an On-Off detector-tree configuration.

The SNR achieved using On-Off detectors is comparable to that obtained with linear detectors in the regime where the number of detected photons remains smaller than 1. However, as the number of excitation cycles K increases, saturation effects arise due to the detectors' inability to count more than a single photon per exposure time. This results in a degraded super-resolved signal and subsequently reduces its SNR.

This saturation effect is represented in the plots of Figures 6.3e, 6.3f, and 6.3h.

We can also introduce detection noise into our model and assess its impact. Specifically, for linear detectors, we considered the presence of a Gaussian readout noise at various levels convoluted with the distribution described in Equation 6.23. As shown in Figure 6.4a, the SNR of the second-order super-resolved signal is primarily affected when the number of excitation cycles is low so that the number of detected photons is lower than the readout noise RMS. However, as the number of excitation cycles increases, the SNR converges to the value observed in the noiseless case.

An illustrative simulation of the second order super-resolved map of three closely spaced single-photon emitters subjected to high readout noise under differing excitation regimes is shown in Figure 6.5b and Figure 6.5c. These simulations demonstrate that an increase in the number of detected photons can effectively mitigate the influence of uncorrelated readout noise, enabling the recovery of a super-resolved image.

Only the simulation for the second super-resolved order is presented here because overcoming noise necessitates operating at high illumination levels, which in turn requires an increased number of excitation cycles K. However, as indicated by Equation 6.30, this requirement significantly compromises the SNR of the super-resolved signal.

Moreover, we can introduce a general, uncorrelated noise into the system of On-Off detectors such that each detector possesses a click probability due to non-photon-related events from the source, denoted as B, as detailed in Appendix B.1.

Similarly as the linear case, this noise affects the system when the number of photons detected per pixel is comparable to the noise level. However, while it was possible in linear detectors (at least in the second-order case) to increase the number of excitation cycles, i.e. raising the mean number of detected photons, to overcome the noise level, this approach actually deteriorates the SNR of the super-resolved signal in systems employing On-Off detectors due to saturation effects. Figure 6.4b illustrates the SNR of the second-order super-resolved signal in a system of two On-Off detectors with varying levels of noise probability, B. From the compromise of reducing the noise effect while avoiding saturation it turns out that an optimal value of K exists that maximize the SNR. This optimal value depends on the noise level.

Additionally, for a visual representation of this phenomena, simulations of intensity and the second-order super-resolved signals of three spaced single-photon emitters in the presence of uncorrelated noise B are presented in Figures 6.5e, 6.5f, and 6.5g for varying values of K. The noise effect, which significantly degrades the SNR in Figure 6.5e, is mitigated in Figure 6.5f. However, further increasing the number of excitation cycles drives the system into a saturation regime. This phenomenon is particularly evident in the central part of Figure 6.5g, where the contributions of multiple emitters are present, thus degrading the SNR.

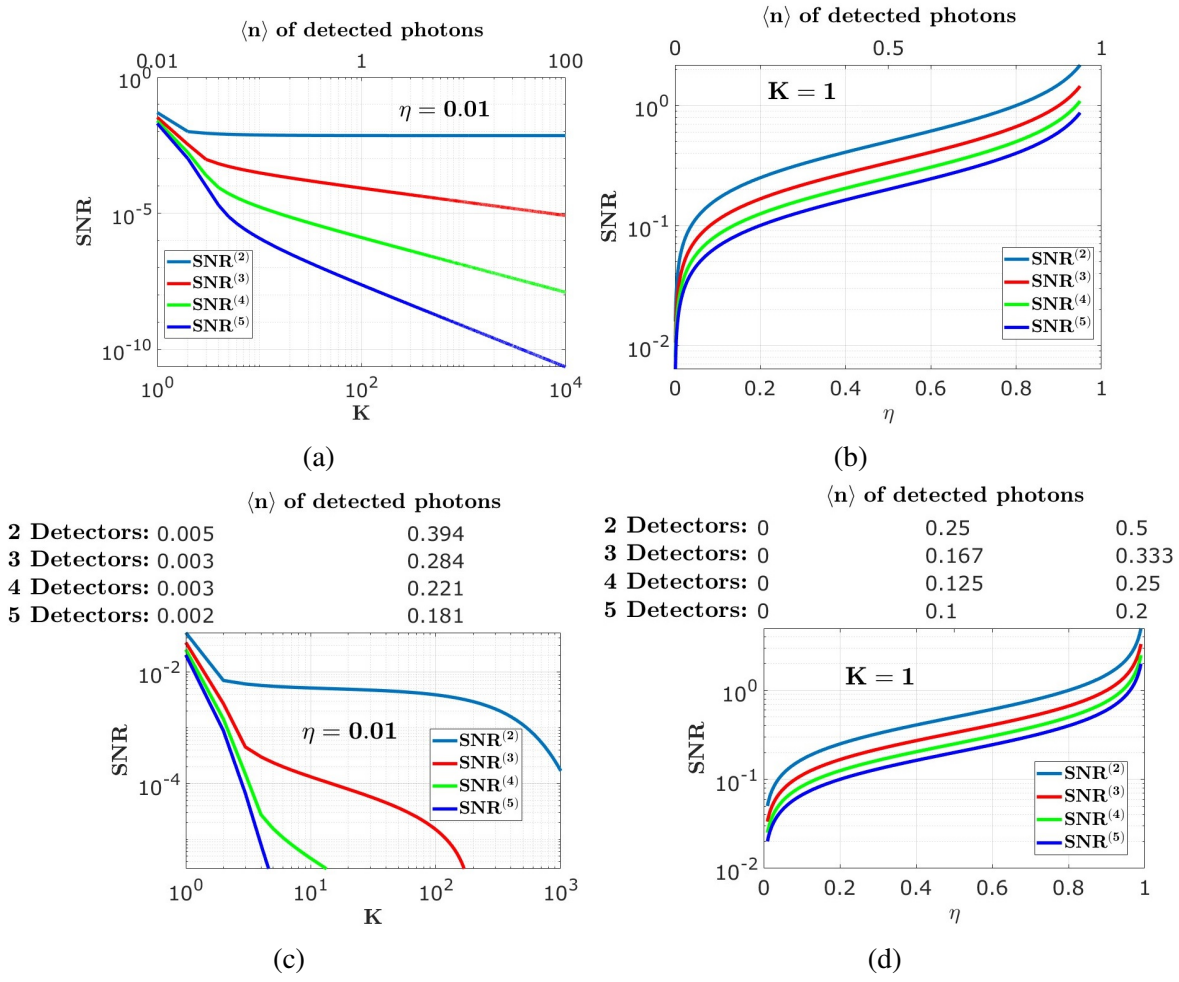

Figure 6.2: *SNR of the first five orders of super-resolved signals from a single photon emitter. Panel (a) shows the dependence of the SNR on the number of excitation cycles K at a fixed detection probability $\eta = 0.01$, while panel (b) shows the dependence on η with K = 1. The top axis indicates the mean number of detected photons. Panels (c) and (d) correspond to panels (a) and (b) respectively, but for a system of j On-Off detectors arranged in a tree-like structure, where j denotes the super-resolved order. The top axis in panels (c) and (d) refers to the mean number of detected photons per single detector.*

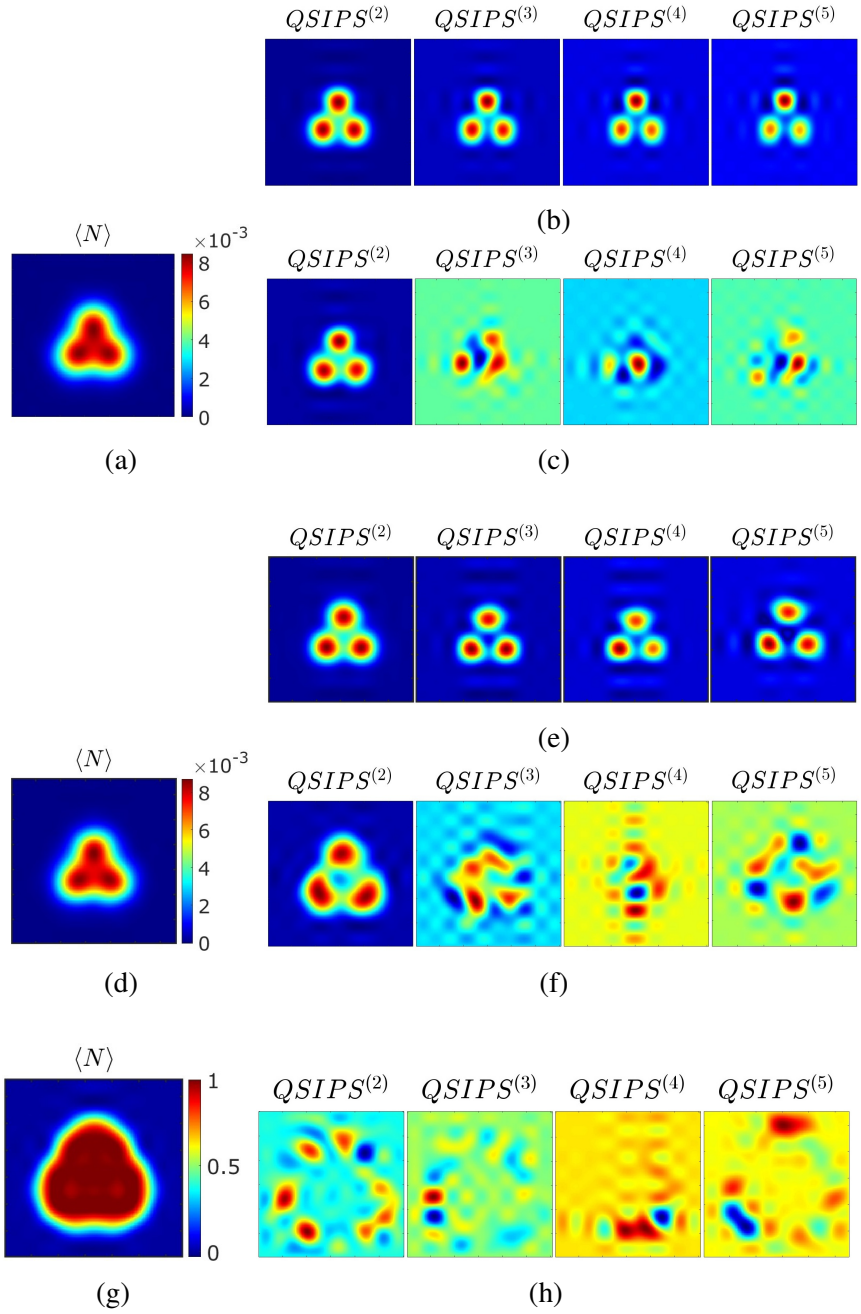

Figure 6.3: *Simulations of intensity images and the first five super-resolution orders of three independent single photon emitters. Panel (a) shows the mean number of detected photons using a linear detector in a noiseless case with K = 1. Panels (b) and (c) display the first five super-resolution orders with a number of excitation cycles K = 1 and K = 1000, respectively. Panels (d) and (g) show the mean number of detected photons in a matrix of noiseless On-Off detectors with K = 1 and K = 1000, respectively. Panels (e), (f), and (h) present the first five super-resolution orders in the same On-Off detector scheme for K = 1, K = 100, and K = 1000. All simulations consider 90% optical losses, excluding the effect of the PSF, and $5 \cdot 10^5$ independent acquisition frames. All images are Fourier interpolated and Gaussian filtered to reduce pixelation effects and avoid artifacts.*

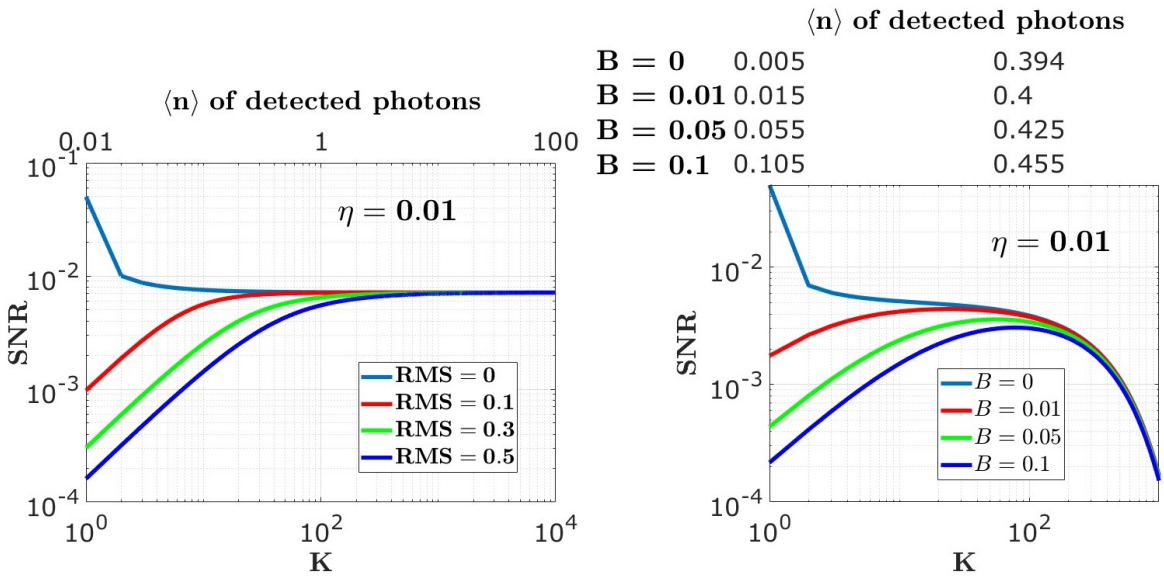

Figure 6.4: *SNR of the second-order super-resolved signals from a single photon emitter in the presence of uncorrelated noise. Panel (a) shows the dependence of the SNR on the number of excitation cycles K at a fixed detection probability of* $\eta = 0.01$ *for five different levels of Gaussian readout noise RMS: RMS = 0, RMS = 0.1, RMS = 0.3, and RMS = 0.5. The top axis indicates the mean number of detected photons. Panel (b) is the equivalent of panel (a), but employs a system of two On-Off detectors, each with a probability B of a click due to a noise event, respectively for: B = 0, B = 0.01, B = 0.05, and* $B = 0.1$*. The top axis refers to the mean number of detected photons per single detector for the different values of B.*

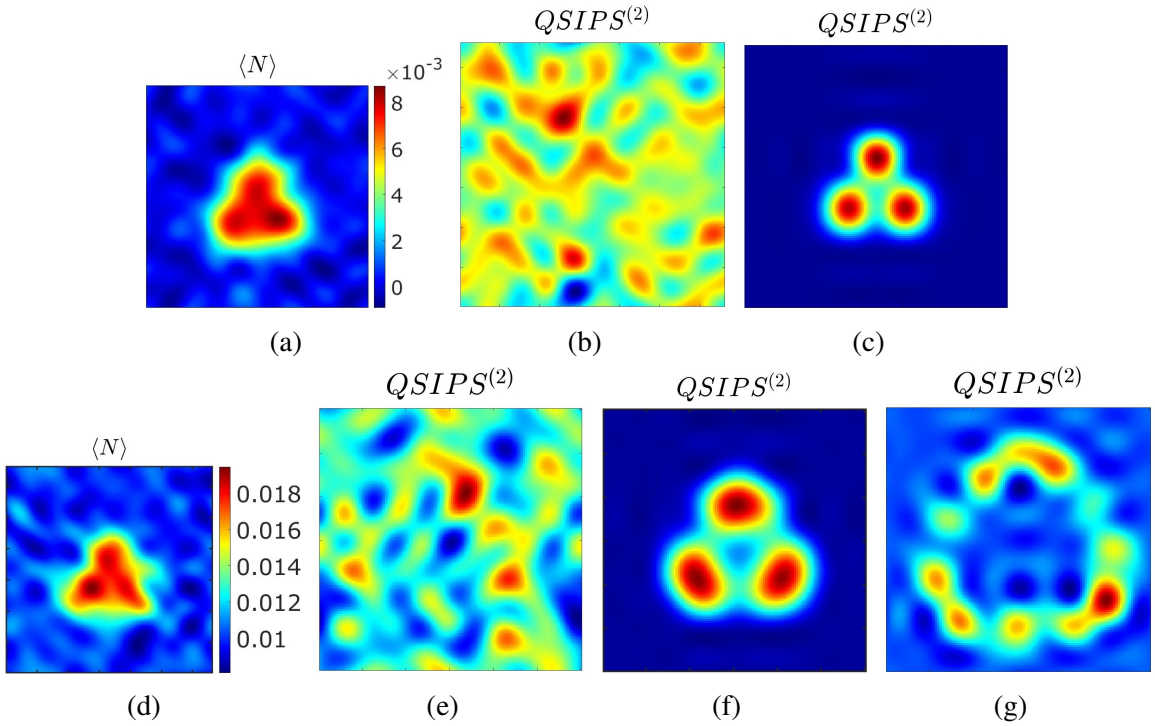

Figure 6.5: *Simulated intensity images and second-order super-resolution outputs for three independent single-photon emitters under a noisy detection scenario. Panel (a) illustrates the average number of photons detected using a linear detector characterized by Gaussian readout noise with an RMS value of 0.5 and K = 1. Panels (b) and (c) depict the second super-resolution order for K = 1 and K = 1000, respectively. Panel (d) displays the average photon counts using a matrix of On-Off detectors with K = 1 and B = 0.01. Panels (e), (f), and (g) show the second super-resolution orders in the same noise condition employing the On-Off detection method for K = 1, K = 100, and K = 1000, respectively. All simulations account for 90% optical losses, excluding the effect of the PSF, and $5 \cdot 10^5$ independent acquisition frames. Each image has undergone Fourier interpolation and Gaussian filtering to minimize pixelation and prevent artifacts.*

6.4 SNR of super-resolved signals from blinking single-photon emitters

As stated in Section 1.2.1, quantum dots can be seen as single photon emitters that possess a non-radiative state that prevents photon emission.

Therefore, we have to use the complete PDF reported in Equation 6.7 in which we take in account the blinking probability b and the ratio M between the integration time and the characteristic switching On-Off time of the detector.

As done for the non-blinking case, we can evaluate the cumulants of the emitted and detected photon distributions using Equation 5.2 and Equation 5.3, respectively, and exploit Equation 5.9 to obtain the relation for the super-resolved signal of order j:

$$QSIPS^{(j)} = \eta^j K(1-b) f(b,K,M). \tag{6.31}$$

$f(b,K,M)$ is a non-trivial polynomial in b, K, and M whose general form for an arbitrary order j cannot be expressed in a compact manner. Nevertheless, similar to what has been done to the non-blinking case we can analyze the SNR dependence on the number of excitation cycles K. In Figure 6.6, the first five super-resolved orders are shown for fixed values of b and η and for different values of M.

A peculiar behavior arises when dealing with low values of K, as shown both in Figure 6.6a and 6.6b. The SNR starts decreasing, reaches zero and it rises again, with increasing values of K. This behavior is closely related to the nature of the super-resolved signal. With low values of K, quantum dots behave mostly like single photon emitters, in particular $Kb < M$ results in a sub-Poissonian photon statistics as we have seen in Equation 6.11. However, as K increases, a gradual transition occurs from a fully sub-Poissonian photon distribution to a Poissonian one ($Kb = M$), bringing the magnitude of the super-resolved signal to zero. Conversely, continuing to increase K, super-Poissonian characteristics arise, reinstating the super-resolved signal.

In order to make the most of the super-Poissonian statistics, one should use fast detector, namely $M = 1$, able to follow the fluctuation of the emitter jumping from the On and Off states. As discussed in Section 6.1, the effect of slow detection schemes, i.e. high values of M, is to reduce the measured super-Poissonian fluctuations of the detected photons distribution. This is illustrated in Figures 6.6a, 6.6b, and 6.6c, where an increase in the parameter M increases the number of excitation cycles needed to achieve super-Poissonian behavior. Ultimately, with high values of M, the super-Poissonian behavior is completely eliminated.

In the high excitation regime, the maximum value of the SNR is independent of the detection probability η and is determined solely by the blinking probability b and the parameter M. While

deriving a compact expression for this limit for a generic order j is not feasible, for clarity, we present the limit for the second- and third-order SNR:

$$\lim_{K\to\infty} SNR^{(2)} = \sqrt{\frac{Mb(1-b)}{1+2b(M-3)-2b^2(M-3)}}, \tag{6.32}$$

$$\lim_{K\to\infty} SNR^{(3)} = \frac{2\sqrt{Mb(1-b)}(b-\frac{1}{2})}{g(M,b)}, \tag{6.33}$$

with:

$$\begin{aligned} g(M,b) &= \sqrt{1+b\alpha_1(M)+6b^2\alpha_2(M)-6b^3[2-b]\alpha_3(M)}, \\ \alpha_1(M) &= 18M-30, \\ \alpha_2(M) &= M^2-18M+25, \\ \alpha_3(M) &= M^2-15M+20. \end{aligned} \tag{6.34}$$

Another interesting behavior arises when studying the dependence of the SNR on the blinking probability. Figure 6.7 presents the behavior of the SNRs of the first five super-resolved signals in the high excitation cycle regime at a fixed value of η and for different values of M. We observe some sharp peaks of the SNR for certain specific values of the blinking probability, whose location changes for each super-resolution order. For example, the value $b = 0.5$ ensures a completely symmetric emitted photon distribution, yielding a maximum SNR for even orders, while for odd orders the SNR is zero. Notably, increasing the super-resolution order increases the number of nodes in the function, scaling with $j-2$. At each node, the sign of the super-resolved signal changes.

This not-trivial behavior makes it challenging to get stability of the super-resolved images through the different orders. It may occur that in a system of independent emitters, each with its own blinking probability, the SNR drastically changes from one emitter to the other while passing from even to odd orders of super-resolution. By comparing Figures 6.7a, 6.7b, and 6.7c one notes that the increasing value of the parameter M tends to mitigate the variability of the SNR, but at the expense to an overall reduction, ultimately reverting the situation to a sub-Poissonian one.

A visual representation of this behavior is reported in Figure 6.8 where a simulation of three blinking emitters possessing different blinking probabilities are analyzed up to the fifth super-resolution order, both in a fast detector situation ($M = 1$) and slow detector one ($M = 1000$).

Regarding the introduction of uncorrelated noise to the system, we can consider convoluting the detected PDF with a Gaussian distribution of the readout noise, as done for the sub-Poissonian case. As shown in Figure 6.9, adding this noise to the signal affects only the sub-Poissonian part of the graph, where the mean number of detected photons is comparable to the value of the readout noise. When the number of excitation cycles increases and the super-Poissonian nature arises, the effect of the readout noise is mitigated and no longer affects the SNR.

We can also study the SNR of blinking emitters exploiting systems of On-Off detectors. Particularly, these systems are often characterized by high acquisition speeds and very low exposure times. Therefore, in this analysis, we will consider the most common case of $M = 1$, meaning that the On-Off detectors can reliably discern between the radiative and non-radiative states of the emitter.

The SNR of the super-resolved signal from a blinking single-photon emitter employing On-Off detectors behaves exactly as the one obtained for the linear case, as shown in Figures 6.10a and 6.10b, due to the absence of saturation effects. In fact, the intrinsic blinking probability b ensures that each detector will reach a maximum mean value of detected photons $\langle n \rangle = 1 - b$. Even with high values of K, a fraction b of exposure times of the detector will consistently lack photon events, preventing saturation.

Even adding a probability B to the model of having a click related to noise events, as done for the sub-Poissonian case, saturation effects from a single emitter do not occur due to the fact that the noise affects only when the number of excitation cycles is low compared to the noise level. Particularly, Figure 6.10c reports the SNR of the second-order super-resolved signal of a blinking single-photon emitter in a scheme employing On-Off detectors for different values of B. Nevertheless, when considering the contribution of multiple emitters, the saturation of a single detector arises due to the uncorrelated nature of emissions across different emitters. This phenomenon is reported in the simulations provided in Figure 6.11, which shows the intensity and super-resolved signals up to the fifth order of three identical blinking single-photon emitters in a matrix of On-Off detectors with different values of K. Especially in the region in the middle of the three emitters, where the probability of having more than one photon in the same detection time window is higher, the saturation compromises the reliability of the super-resolved maps.

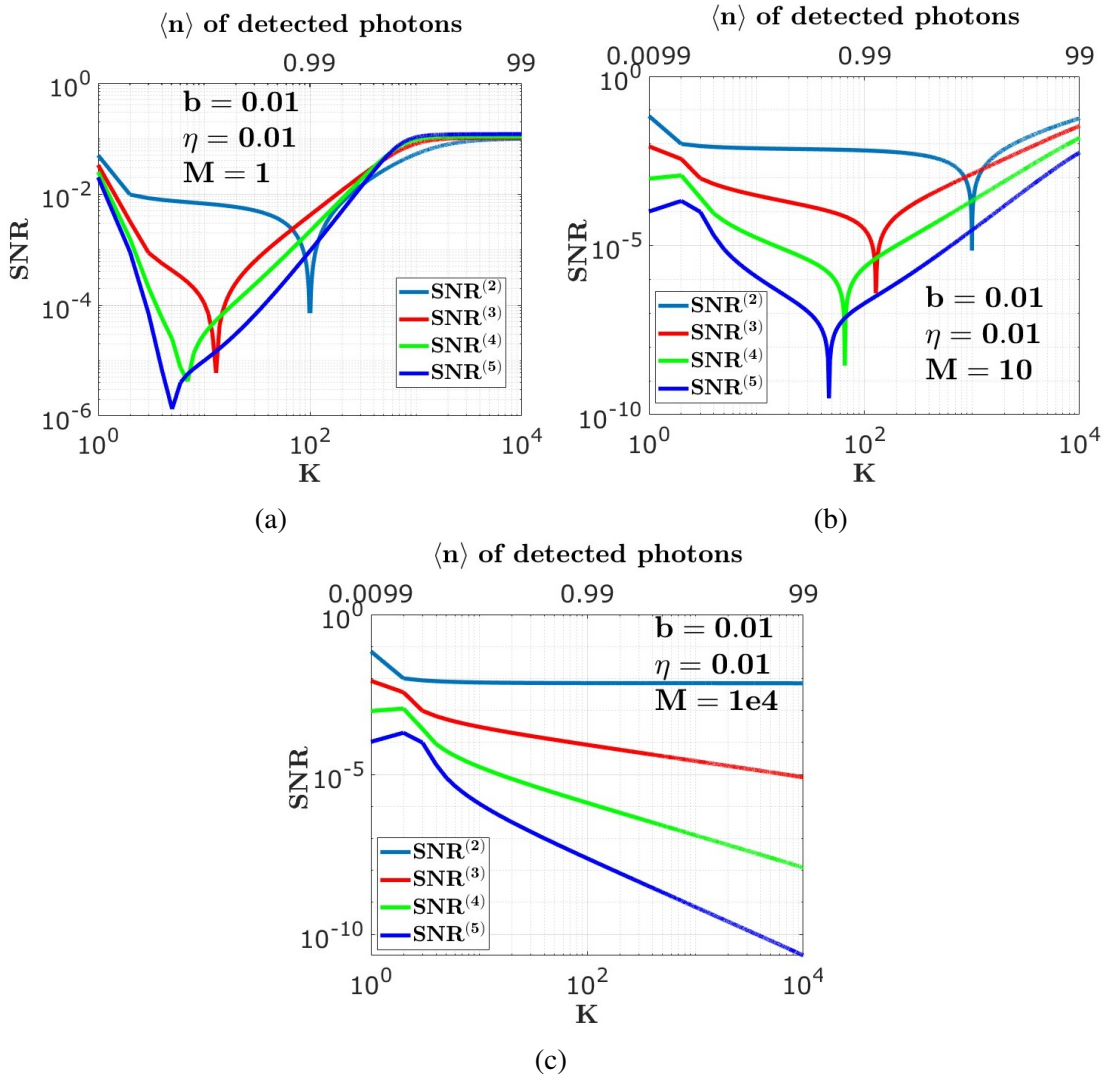

Figure 6.6: *SNR of the first five super-resolved signals from a blinking single photon emitter in a noiseless linear detection system as a function of the number of excitation cycles K , for: (a) M = 1, (b) M = 10, and (c) M = 10^4. All SNR values are evaluated considering a detection probability* $\eta = 0.01$ *and a blinking probability b = 0.01. The top axis indicates the mean number of detected photons.*

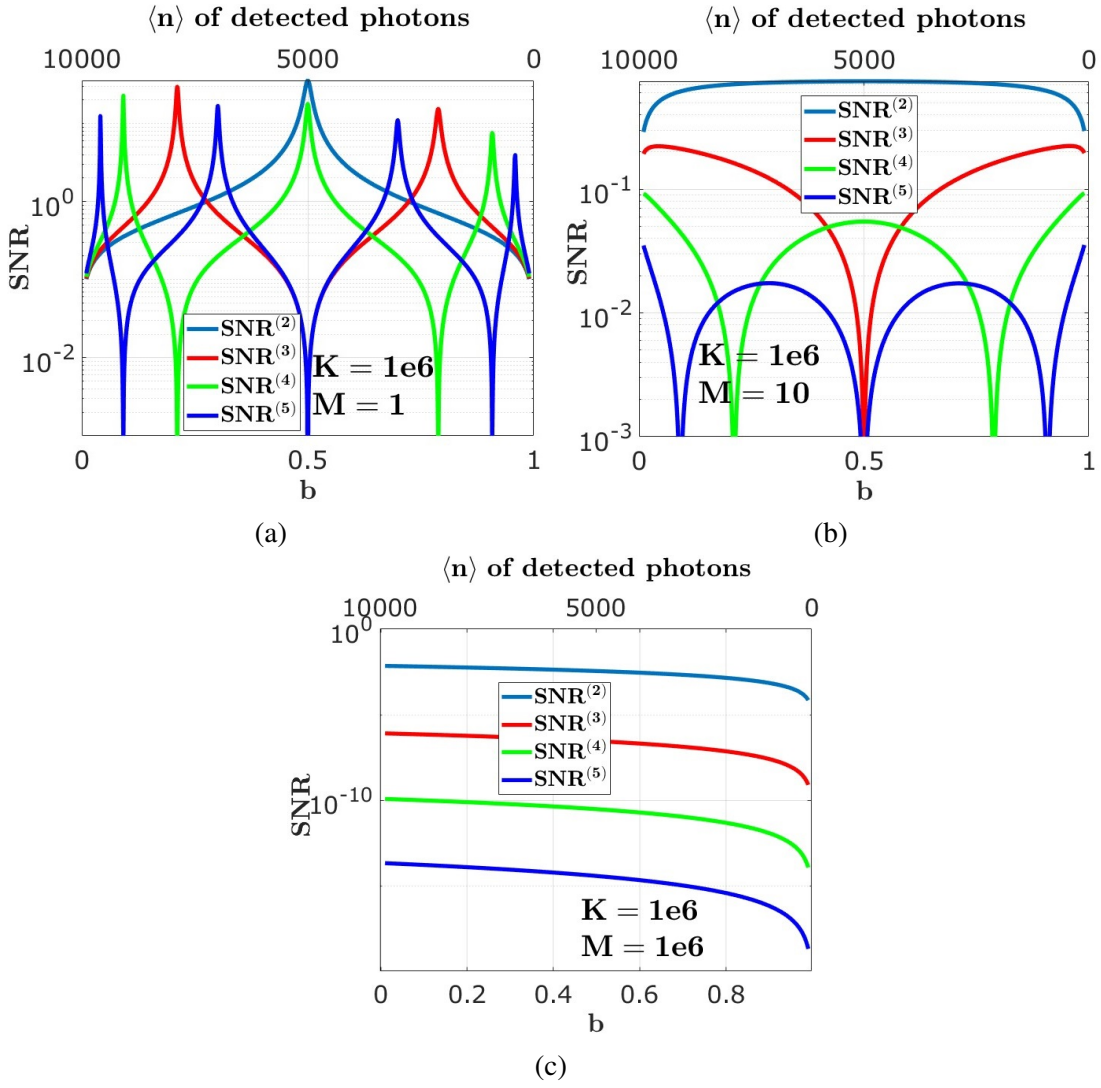

Figure 6.7: *SNR of the first five super-resolved signals from a blinking single photon emitter, displayed as a function of blinking probability b in a noiseless linear detection system. The panels represent different values of M: (a) M = 1, (b) M = 10, and (c) $M = 10^6$. Each SNR value is calculated considering a fixed detection probability $\eta = 0.01$ and $K = 10^6$. The top axis shows the mean number of detected photons for each blinking probability.*

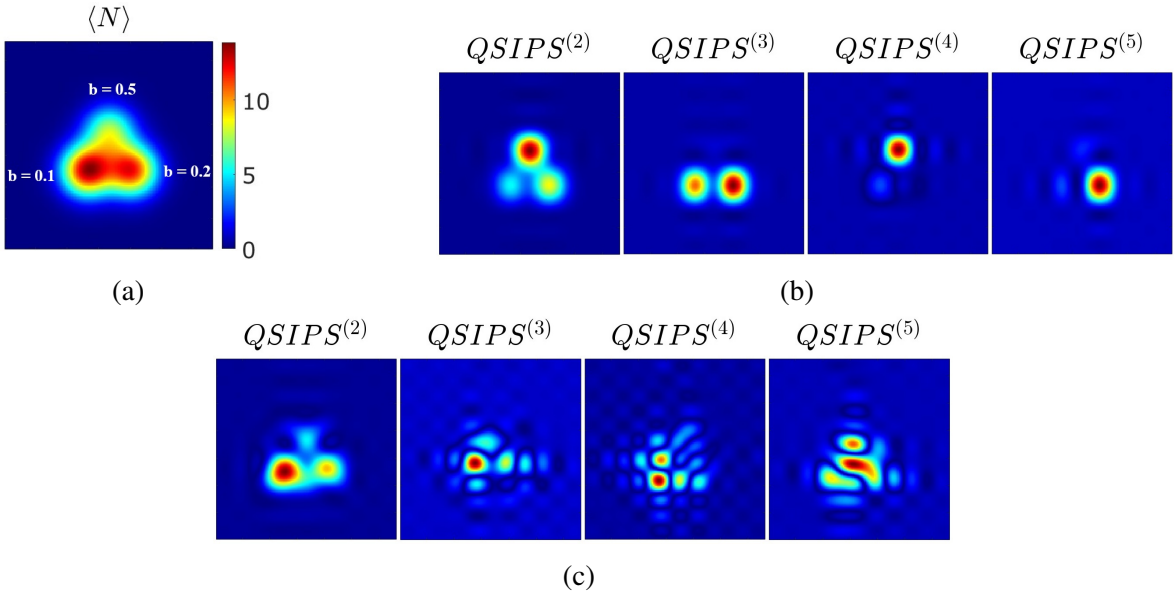

Figure 6.8: *Simulated intensity image and the first five super-resolution orders of three independent blinking single photon emitters, characterized by blinking probabilities of b = 0.1, b = 0.2, and b = 0.5. The simulations use K = 1000 excitation cycles with a linear detector in a noiseless environment. Panel (a) illustrates the mean number of detected photons with M = 1. Panels (b) and (c) present the first five super-resolution orders with M = 1 and M = 1000, respectively. The simulations account for 90% optical losses, excluding the effect of the PSF, with $2 \cdot 10^4$ independent acquisition frames for panels (a) and (b) and $1 \cdot 10^5$ for panel (c). All images have undergone Fourier interpolation and Gaussian filtering to mitigate pixelation and eliminate artifacts.*

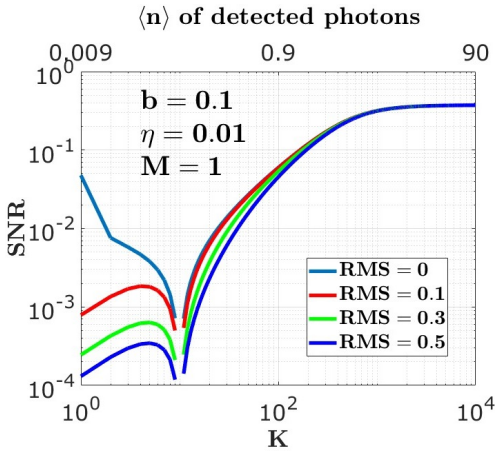

Figure 6.9: *SNR of second-order super-resolved signals from a blinking single photon emitter, analyzed as a function of the number of excitation cycles K. The simulation assumes a fixed detection probability $\eta = 0.01$, blinking probability b = 0.1, and M = 1. The graph illustrates SNR outcomes for five Gaussian readout noise levels: RMS = 0, RMS = 0.1, RMS = 0.3, and RMS = 0.5. The top axis indicates the mean number of detected photons for each set of conditions.*

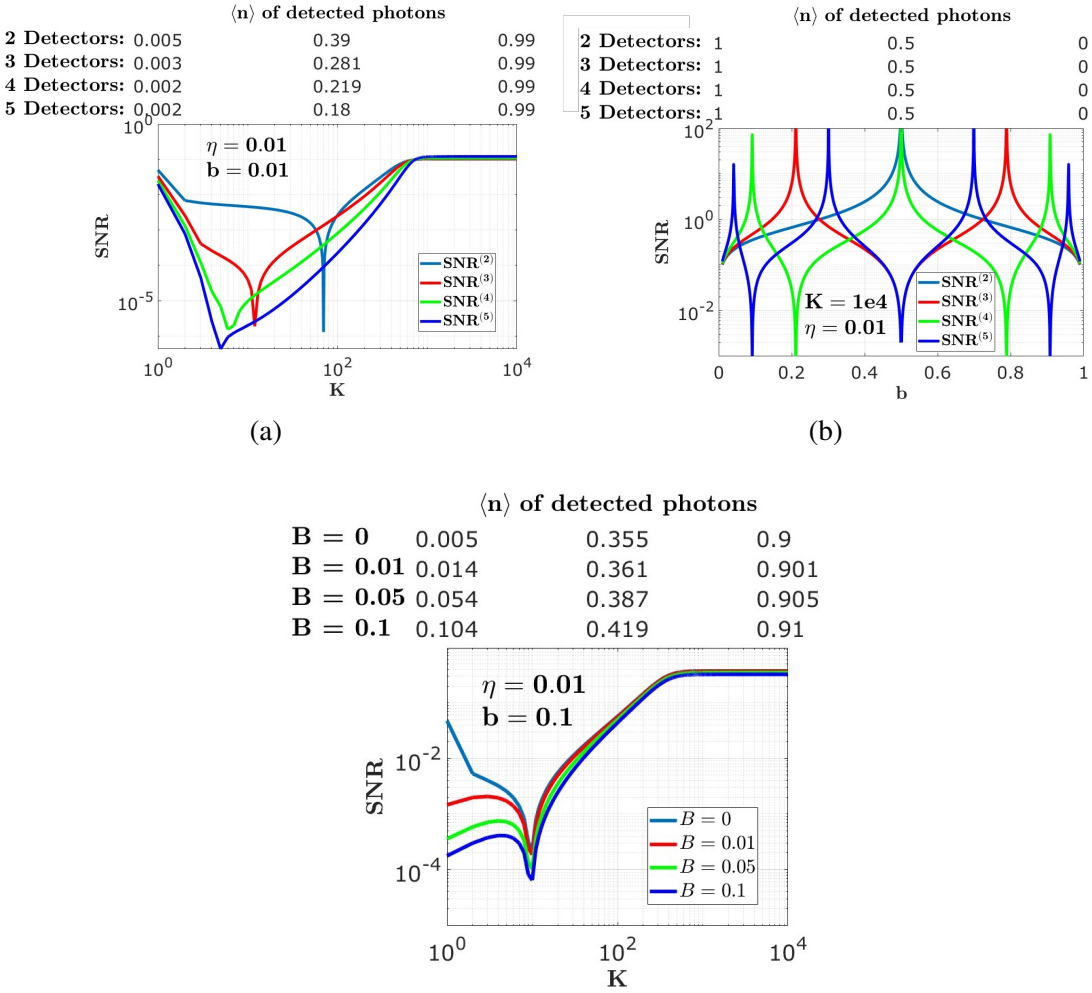

Figure 6.10: *SNR of the first five super-resolution orders from blinking single photon emitters in an On-Off detection scheme with M = 1. Panel (a) explores the SNR's dependency on the number of excitation cycles K, with a blinking probability b = 0.01 and detection probability* $\eta = 0.01$. *Panel (b) examines the SNR's dependence on blinking probability b, for* $K = 10^4$ *and* $\eta = 0.01$. *Panel (c) investigates how the SNR of the second order super-resolved signal varies with the number of excitation cycles K, under different probabilities B of a noise-induced click, set at B = 0, B = 0.01, B = 0.05, and* $B = 0.1$. *The top axis in panels (a) and (b) reports the mean value of detected photons per single detector, while the top axis in (c) denotes the mean number of detected photons per single detector for varying B values.*

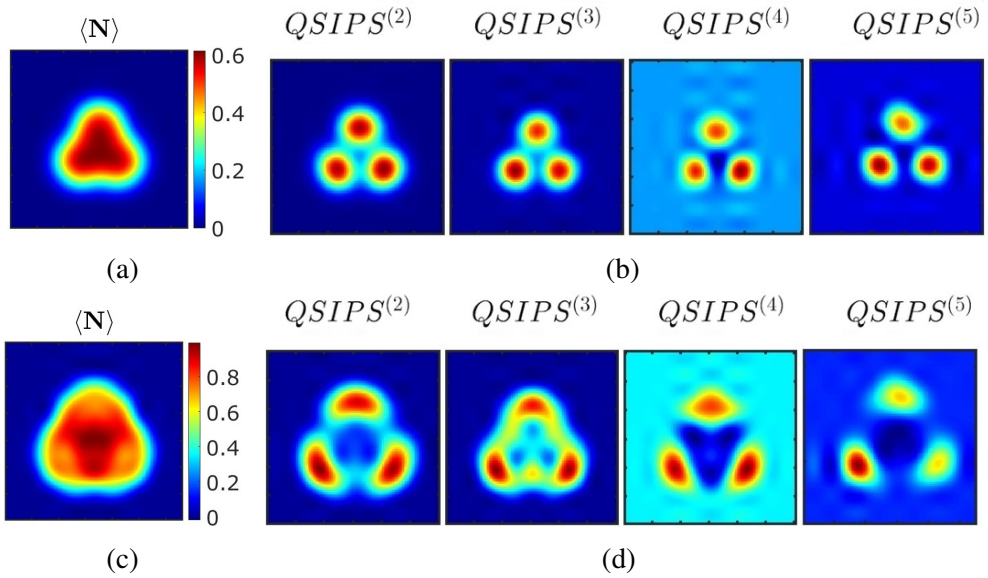

Figure 6.11: *Simulations of intensity image and the first five super-resolution orders of three independent blinking single photon emitters in a noiseless On-Off detection scheme, considering a blinking probability* $b = 0.3$ *for all the emitters. Panels (a) and (c) show the mean number of detected photons with* $K = 100$ *and* $K = 1000$*, respectively. Panels (b) and (d) display the first five super-resolution orders with* $K = 100$ *and* $K = 1000$*. All simulations are performed considering 90% optical losses, excluding the effect of the PSF, and* $2 \cdot 10^4$ *independent acquisition frames. The images are Fourier interpolated and Gaussian filtered to reduce pixelation effects and avoid artifacts.*

6.5 SNR analysis summary

In this section, we present a summary of the key outcomes derived from the analysis of the SNR of super-resolved signals originating from a single-photon emitter that can exhibit blinking behavior. The analysis includes both rapid and slow linear detection methods, as well as fast On-Off detection mechanisms.

In the initial analysis, we considered non-blinking single-photon emitters, such as color centers in crystals. It is found that the optimal SNR is attained when utilizing a single excitation cycle per detector integration period for all super-resolution orders, provided that detector noise is negligible. A significant finding is that specifically second-order super-resolution, accumulating a large number of photons in the detection time windows brings to a consistent value of the SNR solely dependent on the system's detection probability (refer to Figure 6.2a). This behavior is distinct from higher orders of super-resolution, where the SNR sharply declines. This property facilitates the retrieval of super-resolved when using slow and noisy detector, such as CCD or CMOS cameras (see Figure 6.4a). On the other hand, On-Off detectors, such as SPADs or EM-CCD cameras, generally exhibit lower noise levels. Additionally, SPADs have brief exposure times that reduce the susceptibility to other noise sources, such as ambient light. Thus, it is advantageous to utilize a minimal number of excitation cycles per integration period when operating these detectors, ideally one cycle per detection time window.

When examining blinking single-photon emitters, we have shown that it is determined that the SNR is maximized under high illumination conditions, namely when many photons are collected in the detection time, that is where the super-Poissonian character emerges. The maximum value depends solely on the blinking probability of the emitter and the detector's capability to discriminate the On and Off states within a single integration period, indicated by the value of the M parameter. Conversely, under low illumination, particularly $K < M/b$, blinking emitters manifest a sub-poisson behavior (see Figure 6.6). Although high illumination is generally desirable when working with blinking single-photon emitters, the blinking probability value in this regime significantly influences the achievable SNR, enhancing certain super-resolution orders while diminishing others, as shown in the analysis of the SNR reported in Figure 6.7a and the simulated super-resolved images in Figure 6.8b. Specifically, blinking probability is an experimental variable that can vary substantially among different quantum dots, influenced by their size and shape. This variability can significantly expand the dynamic range for specific super-resolution orders. Moreover, it is feasible to achieve super-resolution using On-Off detectors with super-Poissonian emitters; however, it is crucial to avoid high illumination levels that may induce saturation, particularly in scenarios where the signal is derived from the convolution of multiple emitters, as shown in Figure 6.11.

Chapter 7

QSIPS combined with Structured Light Illumination

In this chapter, we present the experimental and simulated work performed to integrate the QSIPS technique with the structured light illumination as described in Section 2.3.1.

In the first part of the chapter we present simulations of second-order super-resolved maps in combination with structured light utilizing blinking emitters in a noisy linear detection scheme. Subsequently, an experimental realization of structured light in combination with super-Poissonian statistics is reported, emphasizing the super-resolution enhancement achieved with QSIPS, in comparison to classical SOFI.

7.1 Simulations

In SIM, achieving maximum resolution enhancement necessitates the precise tailoring of the length of the illumination frequency vector $|\mathbf{p}_\theta|$ (refer to Equation 2.24) of the structured light pattern to achieve the highest possible resolution. As detailed in Section 2.3, the optical system acts as a low-pass filter, allowing only frequencies up to $k_{Abbe} = d_{Abbe}^{-1} = 2NA/\lambda$ to be retrieved. Consequently, also the length of the illumination frequency vector at the object plane must be $|\mathbf{p}_\theta| \leq k_{Abbe}$ to ensure proper visibility at the imaging plane of the signal. In principle, the maximum resolution improvement is achieved when the equality holds.

As described in Section 2.1, we can approximate the response function of the optical system as a Gaussian with variance σ^2. Particularly, the approximated Gaussian will be characterized by a standard deviation $\sigma \simeq 0.42 d_{Abbe}$ [78]. Therefore, the relation between the maximum frequency transmitted by the system and the standard deviation σ is: $k_{Abbe} = 0.42/\sigma$. In the framework of our simulated work, the modulus of the illumination frequency vector for each

orientation θ is set to $|\mathbf{p}_\theta| = k_{Abbe}$. The Optical Transfer Function, denoted as $\tilde{\eta}(\mathbf{k})$, used in the simulations, along with its one-dimensional plot showing the relative magnitude of the illumination frequency vector, are presented in Figure 7.1.

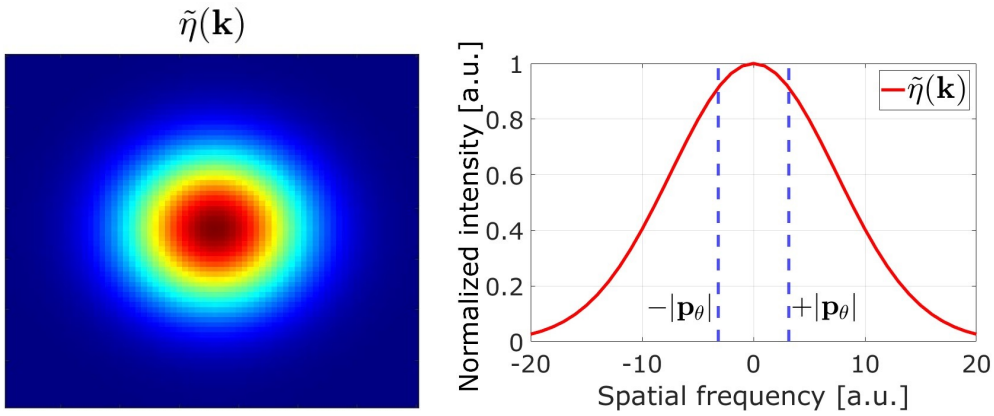

(a) (b)

Figure 7.1: *(a) Simulated Optical Transfer Function (OTF), denoted as $\tilde{\eta}(\mathbf{k})$. (b) One-dimensional plot of a section of the OTF (red line) alongside the relative magnitude of the illumination frequency vector used in the simulations (dashed blue lines).*

The simulated images are produced by distributing multiple independent emitters in the ideal conjugated object plane (unitary magnification) of the multipixel detection matrix, operating in linear regime and characterized by Gaussian readout noise.

Each emitter α, positioned at (x_α, y_α), has a probability $\xi_\alpha(k)$ of emitting k photons in the presence of structured illumination, described as:

$$\xi_\alpha(k) = \sum_{m=0}^{\infty} P(m)\mathscr{B}(k/m, I(x_\alpha, y_\alpha)), \tag{7.1}$$

where $P(m)$ is the emitted photon probability reported in Equation 6.3 and with $I(x,y)$:

$$I(x,y) = \frac{1}{2}[1 - \cos(2\pi(p\cos(\theta)x + p\sin(\theta)y) + \phi)], \tag{7.2}$$

derived from Equation 2.24 by setting $I_0 = 1$, $\mathbf{p}_\theta = [p\cos(\theta), p\sin(\theta)]$ and $|\mathbf{p}_\theta| = p$. In practice, the structured light act as a binomial filter with transmittance probability $I(x_\alpha, y_\alpha)$.

Subsequently, the signal undergoes processing through another binomial filter characterized by the transmittance probability $\eta_\alpha(x,y)$, which simulates the cumulative impact of optical losses and the PSF effects:

$$\mathscr{P}_\alpha(n) = \sum_{k=0}^{\infty} \xi_\alpha(k)\mathscr{B}(n/k, \eta_\alpha(x,y)). \tag{7.3}$$

This detected photon probability, apart from the effect of the structured illumination, corresponds to the expression in Equation 6.7 with the parameter set to $M = 1$.

As elaborated in Section 2.3.1, integrating structured illumination with non-Poissonian photon statistics necessitates conducting multiple acquisitions. This involves varying the angle θ of the sinusoidal illumination pattern to cover the frequency domain comprehensively. For each specific angle θ, multiple acquisitions must be performed by changing the phase ϕ to effectively resolve all frequency components. In the framework of these simulations, the following values were considered for θ and ϕ, respectively:

$$\phi = \left[0, \frac{2\pi}{5}, \frac{4\pi}{5}, \frac{6\pi}{5}, \frac{8\pi}{5}\right] + \frac{\pi}{8}, \tag{7.4}$$

$$\theta = \left[0, \frac{\pi}{4}, \frac{2\pi}{4}, \frac{3\pi}{4}\right] - \frac{3\pi}{8}. \tag{7.5}$$

These values of θ and ϕ are the same as those used in the experimental realization discussed in Section 7.2. The offset values of $\pi/8$ and $-3\pi/8$, for ϕ and θ respectively, are empirically selected to facilitate the generation of structured light and its experimental reconstruction.

A simulated study was conducted with independent emitters, all possessing equal blinking probability b (see Equation 6.3), focusing on a low-light scenario. When considering second-order super-resolved signals obtained with SOFI and QSIPS methods, as presented in Equations 5.26 and 5.27, we find that the classical SOFI technique approximates QSIPS under the following condition:

$$\eta_\alpha^2(\mathbf{r}) \left[c_\alpha^{(2)} - c_\alpha^{(1)}\right] \gg \eta_\alpha(\mathbf{r}) c_\alpha^{(1)}, \tag{7.6}$$

where α is the index of a generic emitter and $\eta_\alpha(\mathbf{r})$ is the probability of detecting a photon from the α-th emitter in the position $\mathbf{r}$ in the detector plane. Rearranging Equation 7.6 and using the definition of the Fano Factor of the emitted photon distribution from Equation 6.11, we derive:

$$\eta_\alpha(\mathbf{r}) \left[F_{\text{emitted}} - 1\right] \gg 1. \tag{7.7}$$

Experimentally, we typically measure the Fano factor of the detected photon distribution rather than the emitted one. Therefore, using Equation 6.12, we can express Equation 7.7 as:

$$F_{\text{detected}} \gg 2. \tag{7.8}$$

Equation 7.8 provides a straightforward criterion that serves as a rule of thumb to determine if the second-order super-resolved signal evaluated with the SOFI method can correctly approximate the QSIPS second-order signal. Consequently, we consider a high illumination regime when $F_{\text{detected}} \gg 2$, and a low-light scenario otherwise.

For each value of θ and ϕ, $\langle N(\theta,\phi)\rangle$, $SOFI^{(2)}(\theta,\phi)$ and $QSIPS^{(2)}(\theta,\phi)$ maps were reconstructed following the steps described in Section 2.3.1. The final super-resolved maps has been obtained by combining all maps for the different angles and phases, and are reported in Figures 7.2a, 7.2b and 7.2c, respectively. Subsequently, utilizing the algorithm described in Section 2.3.1, the frequency components of the images were shifted to their correct positions in the Fourier space. Consequently, an inverse Fourier transform of the merged frequencies components was then performed to retrieve both $SOFI^{(2)} - SIM$ and $QSIPS^{(2)} - SIM$, which are shown in Figures 7.2d and 7.2e, respectively.

The simulated images show that, in low photon number regime, the higher resolution enhancement provided by QSIPS, compared to classical SOFI, is maintained through integration with structured light.

To elucidate this point more effectively, a one-dimensional plot was generated following the dashed line shown in Figure 7.2e. Subsequently, the visibility, described in Equation 5.30, was assessed for both minima and averaged between them for both SOFI, $V = (20 \pm 1)\%$, and QSIPS, $V = (77 \pm 1)\%$, showing the better performance of QSIPS technique in low light conditions. However, we must notice that the visibility obtained with SOFI depends on the parameters used in our simulation. As described in Chapter 5.2, SOFI serves as an approximation of QSIPS, with its accuracy contingent on the considered statistics and the regime.

To evaluate the effective enhancement in resolution of the various super-resolution techniques, an analysis was conducted on an isolated blinking emitter under both low and high levels of illumination. Specifically, the spatial standard deviation of the effective PSF was determined by a two-dimensional Gaussian fit across the intensity image and the images obtained by classical SOFI, our QSIPS techniques, and their integration with structured illumination. The sections of the Gaussian fit, taken along one spatial axis are shown in Figure 7.3, where the case of low and high illumination are presented in the panels (a) and (b), respectively.

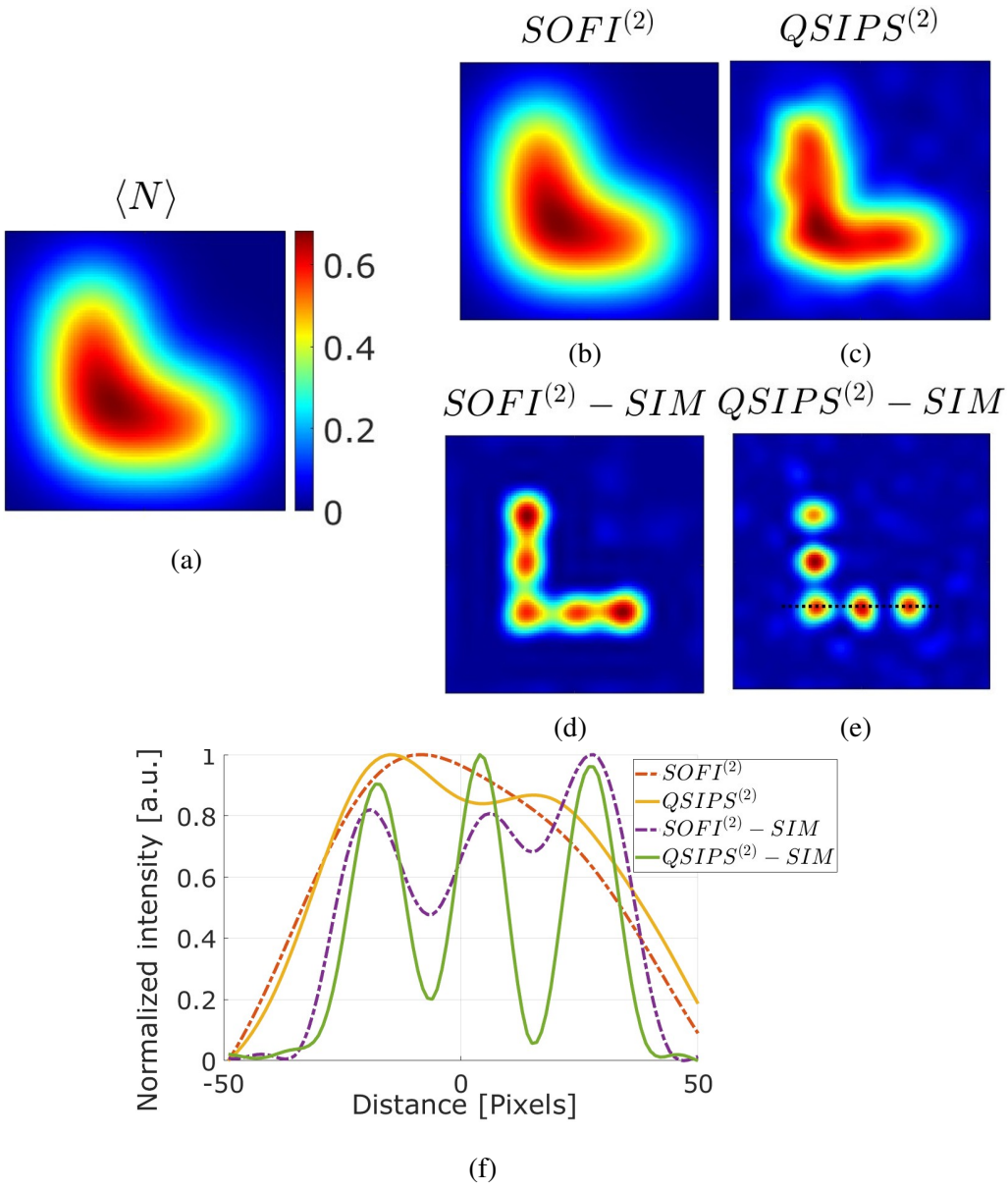

Figure 7.2: *Combinantion of the of second-order super-resolved signals with structured illumination for a L-shaped distributions of identical independent blinking emitters. Panels (a), (b), and (c) show the mean number of detected photons, the SOFI$^{(2)}$, and the QSIPS$^{(2)}$ images, respectively. Panels (d) and (e) present the integration of SIM with classical and quantum methods, labeled SOFI$^{(2)}$ – SIM and QSIPS$^{(2)}$ – SIM, respectively. Panel (f) displays the normalized one-dimensional plot along the dashed line shown in panel (e) for all the super-resolution methods. The simulations are performed considering 90% optical losses, excluding the effect of the PSF, blinking probability b = 0.1, K=100 excitation cycles per frame, a readout noise of RMS* $= 0.23$*, and* $5 \cdot 10^3$ *independent acquisition frames per single value of* θ *and* ϕ*. The images are Fourier interpolated and Gaussian filtered to reduce pixelation effects and avoid artifacts.*

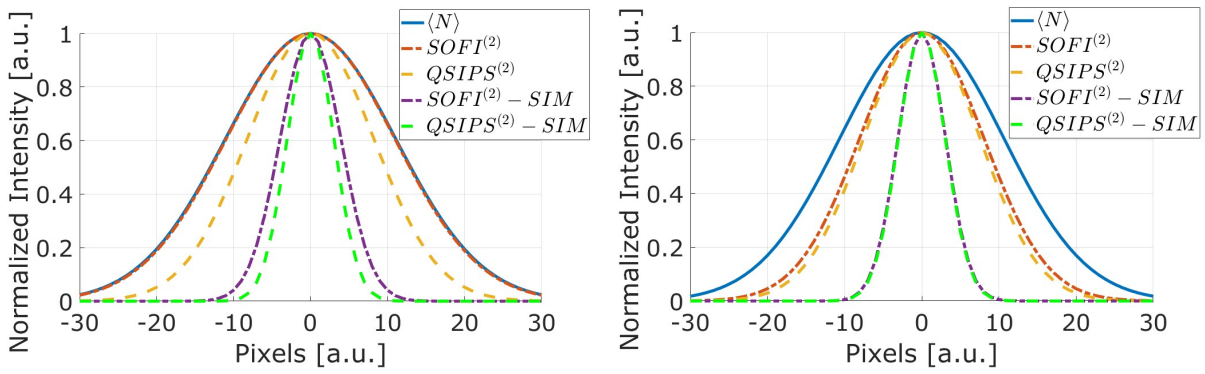

Figure 7.3: *One-dimensional projection of the Gaussian fit performed on the effective PSF of a simulated single emitter with blinking probability b = 0.1 across the super-resolution techniques. Panel (a) refers to a low light regime (mean number of detected photons $\langle N \rangle = 0.3$, $K = 10^2$) while panel (b) refers to a high level of illumination ($\langle N \rangle = 30$, $K = 10^4$).*

We can identify an effective super-resolution factor, labeled SRF, defined as the inverse of the standard deviation of the effective PSF, normalized by the one obtained from the intensity image, and compared it with the theoretical value $SRF_{th} = \sqrt{2}$ for both $QSIPS^{(2)}$ and $SOFI^{(2)}$ and $SRF_{th}^{(SIM)} = 2+\sqrt{2}$ for $QSIPS^{(2)} - SIM$ and $SOFI^{(2)} - SIM$ (see Section 2.3.1). A resume of the super-resolution factor obtained in low and high mean photon number simulations is reported in Table 7.1.

$\langle N \rangle$	F_{detected}	$SRF_{SOFI^{(2)}}$	$SRF_{QSIPS^{(2)}}$	$SRF_{SOFI^{(2)}-SIM}$	$SRF_{QSIPS^{(2)}-SIM}$
0.3	1.03 ± 0.02	1.01 ± 0.02	1.40 ± 0.02	2.63 ± 0.02	3.42 ± 0.02
30	4.33 ± 0.02	1.39 ± 0.02	1.42 ± 0.02	3.39 ± 0.02	3.40 ± 0.02
	Th	1.41	1.41	3.41	3.41

Table 7.1: Simulated super-resolution factors for the various super-resolution techniques both in low and high photon regime and their theoretical values.

In the low photon regime, the SOFI super-resolution factor is approximately 1, indicating that in the classical SOFI signal, reported in Equation 5.26 the contributions proportional to the first power of the optical PSF, becomes the dominant one. This is because, in the low light regime, the factor that multiplies the square of the PSF in the $SOFI^{(2)}$ signal (i.e. $Var(N) - \langle N \rangle$) is nearly zero. This occurs due to the minimal difference between the variance and the mean value of the detected photons, resulting in the dominance of the shot noise term. Consequently, in this regime, $SOFI^{(2)} - SIM$ will not provide a super-resolution enhancement compatible with the theoretical prediction. The super-resolution factors of $QSIPS^{(2)}$ and $QSIPS^{(2)} - SIM$ are both in agreement with their respective theoretical values of $\sqrt{2}$ and $2+\sqrt{2}$.

In high illumination condition, $SOFI^{(2)}$ approximates its quantum counterpart, as does its integration with structured light. In this regime, the super-resolution factors of all super-resolution methods align with their theoretical expectations.

7.2 Experimental results

An experimental realization of the comparison between $SOFI^{(2)} - SIM$ and $QSIPS^{(2)} - SIM$ was conducted using the setup described in Chapter 4.

The PSF of the system was assessed by focusing on an isolated emitter (Figure 7.4a), from which a two-dimensional Gaussian fit was conducted (Figure 7.4b). By performing the Fourier transform of the Gaussian fit, the OTF was evaluated (Figure 7.4c).

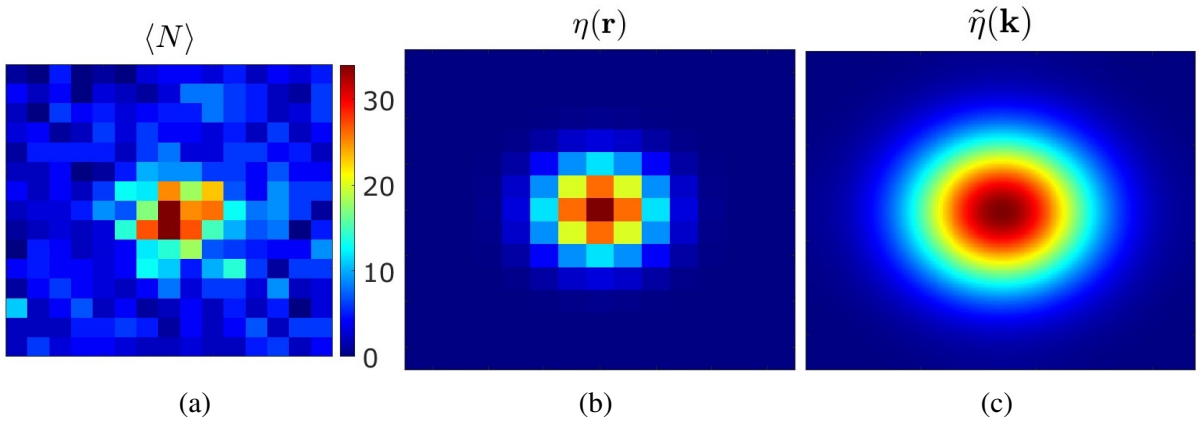

Figure 7.4: *Evaluation of the experimental PSF and OTF. Panel (a) shows an intensity image of an isolated blinking emitter used to assess the PSF of the system, acquired with an exposure time of 100 ms and an output power before the objective of 5 mW. Panel (b) represents the two-dimensional Gaussian fit applied to the emitter in panel (a). Panel (c) shows the OTF of the system, evaluated by performing the Fourier transform of panel (b).*

A series of images containing a two-dimensional cosinusoidal pattern, as described in Equation 7.2, were generated using a MATLAB script. These patterns were imposed on the pixels of the Spatial Light Modulator. The values of the phases ϕ and the angles θ of the illumination profiles used correspond to those reported in Equations 7.4 and 7.5, respectively.

To estimate the illumination frequency vector, a sample with a high concentration of quantum dots was used, from which the interference pattern was clearly visible. An intensity image acquired using $\theta = \pi/8$ and $\phi = \pi/8$ is presented in Figure 7.5a as an example. By performing the Fourier transform of the intensity image, shown in Figure 7.5b, a bright central region corresponding to the low frequencies transmitted by the optical system (circled in red) can be observed, along with two bright spots indicating the positions of the illumination

frequency vector scaled by a factor 2π (circled in white). Additionally, Figure 7.5c displays a one-dimensional plot of the OTF along with the magnitudes of the illumination frequency vectors used in the experiment.

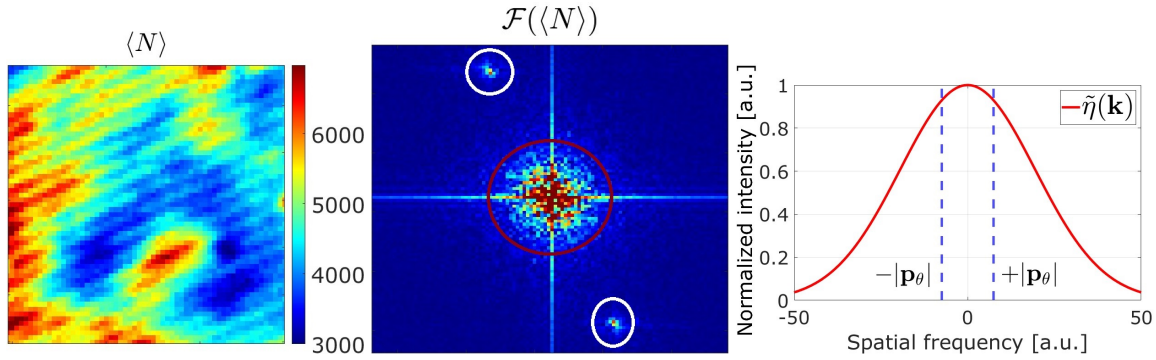

(a) (b) (c)

Figure 7.5: *Evaluation of the experimental illumination frequency vector. Panel (a) shows an intensity image of a quantum dot sample with a high density of emitters utilizing structured light with $\theta = \pi/8$ and $\phi = \pi/8$ acquired with 100 ms of exposure time and a laser power before the objective of 200 μW. Panel (b) presents the Fourier transform of panel (a), where two peaks circled in white correspond to $-2\pi\mathbf{p}_\theta$ and $+2\pi\mathbf{p}_\theta$, along with the red circled region representing the low frequency information retrieved by the system. Panel (c) shows the relative magnitude between the experimental OTF and the modulus of the illumination frequency vector.*

After assessing the illumination frequency vector, an analysis was performed on a cluster region of a different quantum dot sample with a lower density of emitters. Specifically, the mean value of all orientations of the cluster region is reported in Figure 7.6a.

Utilizing the previously obtained frequency vector, the $SOFI^{(2)}$, the $QSIPS^{(2)}$, and their integration with the SIM algorithm were evaluated following the same procedure described in Section 7.1 for the simulated case. The results are showcased in Figure 7.6. It can be observed that the increase in resolution provided by the QSIPS technique, compared to classical SOFI, is also maintained in their respective integration with structured light.

To highlight this, a one-dimensional plot along the black segment of the $QSIPS^{(2)} - SIM$ map (Figure 7.7a) is presented in Figure 7.7b, demonstrating the visibility enhancement achieved by the different super-resolution techniques.

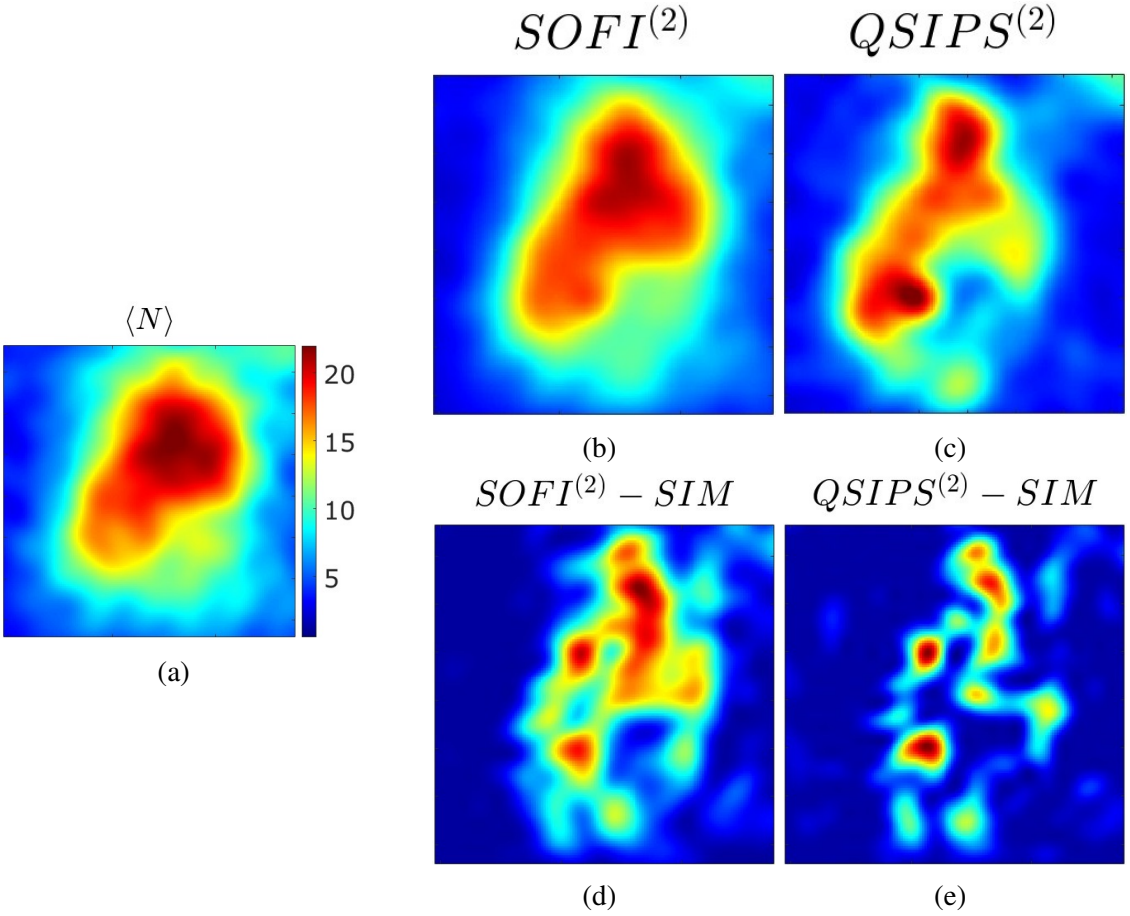

Figure 7.6: *Experimental realization of second-order super-resolved signals integrated with structured illumination. Panel (a) shows the mean number of detected photons, while panels (b) and (c) show the SOFI$^{(2)}$, and QSIPS$^{(2)}$ maps, respectively. Panels (d) and (e) present the integration of SIM with classical and quantum methods, labeled SOFI$^{(2)}$ – SIM and QSIPS$^{(2)}$ – SIM, respectively. The acquistions are performed setting a 200 ms exposure time, a laser power of 500 μW and $5 \cdot 10^2$ acquisition frames per single value of θ and ϕ. The images are Fourier interpolated and Gaussian filtered to reduce pixelation effects and avoid artifacts.*

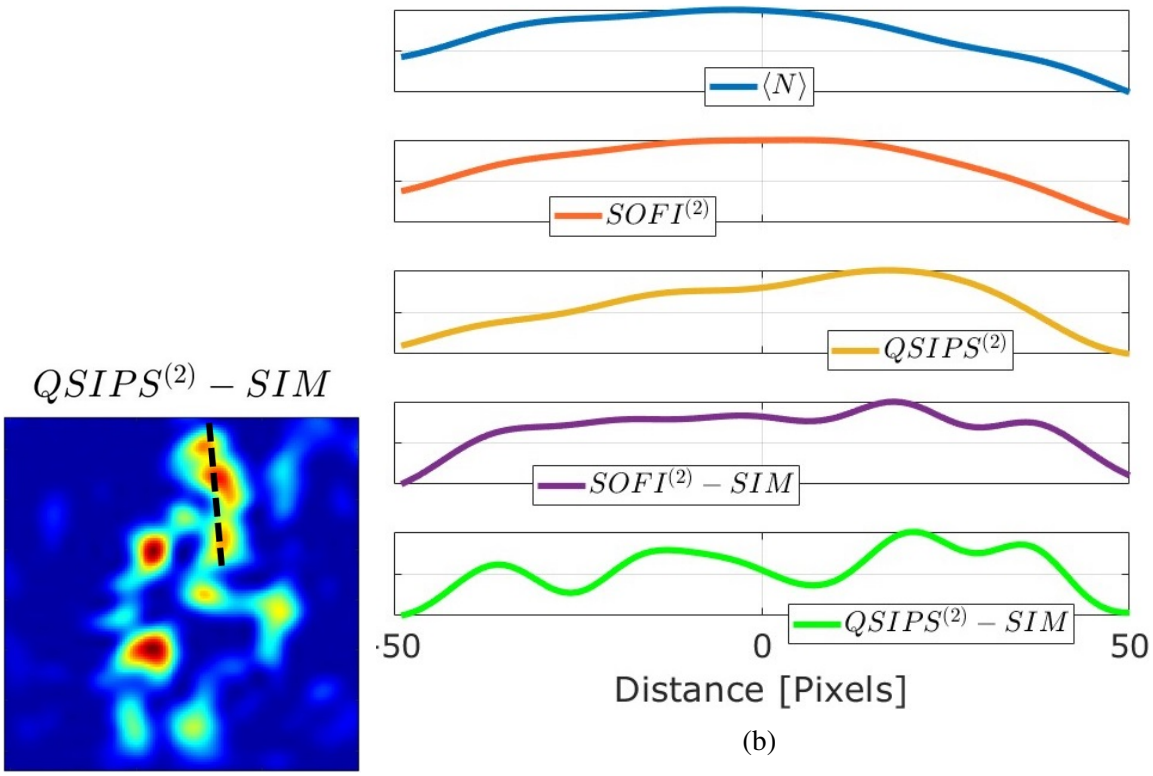

(a) (b)

Figure 7.7: *Showcase of the resolution enhancement of the different super-resolution techniques. Panel (a) shows the $QSIPS^{(2)} - SIM$ map with a black dashed line indicating the section where a one-dimensional plot is performed, which is reported in panel (b).*

As done for the simulative case, we can study the reduction of the effective PSF of an isolated emitter for the different resolution methods to assess the super-resolution factor. Particularly, we focused on an isolated emitter and performed a two-dimensional Gaussian fit of the effective PSFs for all the super-resolution methods estimating the standard deviation. Figure 7.8b reports the one-dimensional plot of the projection of the Gaussian fit for all the super-resolution methods. The super-resolution factors, obtained by the ratio of the Gaussian standard deviation of the intensity with that of super-resolved maps, are reported in Table 7.2.

	$SRF_{SOFI^{(2)}}$	$SRF_{QSIPS^{(2)}}$	$SRF_{SOFI^{(2)}-SIM}$	$SRF_{QSIPS^{(2)}-SIM}$
Exp	1.2 ± 0.1	1.4 ± 0.1	1.8 ± 0.1	2.3 ± 0.1
Th	1.4	1.4	3.4	3.4

Table 7.2: Experimental super-resolution factors for the various super-resolution techniques and their theoretical values.

The super-resolution factors of $QSIPS^{(2)}$ and $QSIPS^{(2)} - SIM$ are greater than their respective classical counterparts, proving the efficacy of our quantum method in low-light conditions.

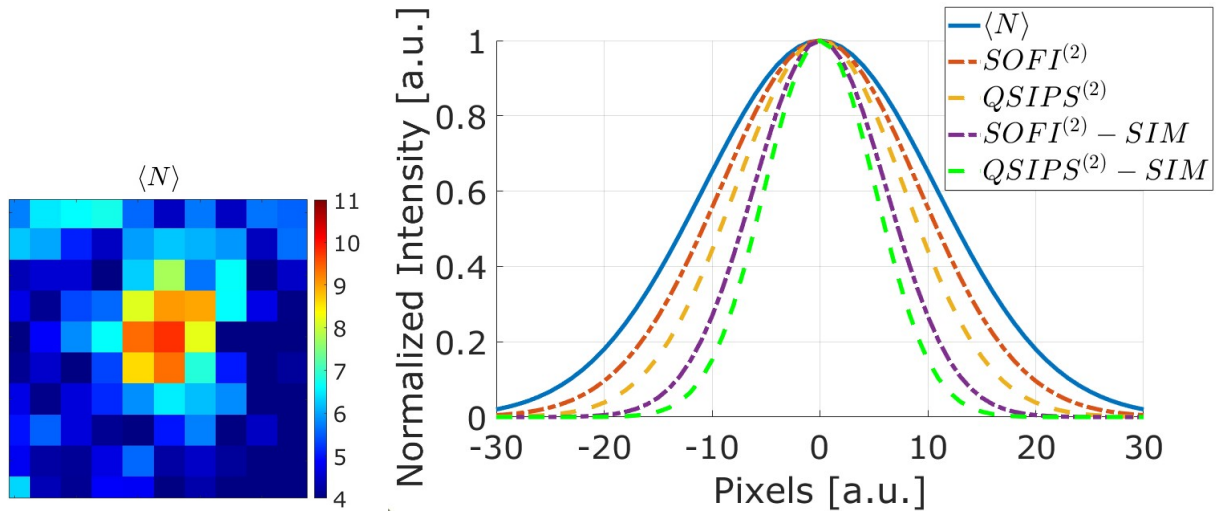

(a) (b)

Figure 7.8: *Analysis of the super-resolution factor. Panel (a) shows the mean intensity image of the emitter utilized for the study, while panel (b) presents the one-dimensional projection of the Gaussian fit performed on the effective PSF across the super-resolution techniques.*

It is important to note that, although there is an advantage, it is limited by the not particularly low light regime. We can assess the Fano factor of the detected photon distribution by calculating the ratio of the variance to the mean number of detected photons, averaging over the region encompassed within one standard deviation of the PSF. The estimated Fano factor for the isolated emitter is $F_{\text{detected}} = 1.8 \pm 0.1$. As stated in Equation 7.8, the high photon regime, where SOFI accurately approximates QSIPS, is achieved when $F_{\text{detected}} \gg 2$. In this context, the Fano factor of the detected photon distribution is near the threshold value, indicating that the classical SOFI technique begins to approximate the QSIPS method.

A compromise was made between achieving a sufficient SNR for quantitative data analysis and minimizing uncertainties on one hand, and on the other hand, demonstrating a clear advantage of QSIPS over SOFI. This approach ensures that the analysis remains robust while highlighting the benefits of QSIPS in comparison to SOFI.

Furthermore, only $QSIPS^{(2)}$ is compatible with the theoretical value of $\sqrt{2}$, while the resolution factor of $QSIPS^{(2)} - SIM$ is shown to be less than the expected value of $2+\sqrt{2}$. This discrepancy may arise from the magnitude of the frequency vector used in the experiment: the theoretical resolution is evaluated considering $|\mathbf{p}_\theta| = k_{Abbe}$. However, since the value of $|\mathbf{p}_\theta|$ is derived from an experimental image, working at that frequency is challenging due to the low transmission of the optical system at that spatial frequency. Selecting $|\mathbf{p}_\theta| < k_{Abbe}$ makes it easier to perform the SIM reconstruction algorithm, but at the expense of reducing the effective resolution enhancement. Another potential source of uncertainty is accurately determining the

length of the illumination frequency vector. In particular, as shown in Figure 7.5a, $\mathbf{p}_\theta$ was assessed by exploiting a different sample of the same classes of emitters but with a higher density of centers. This adjustment was necessary because the low density of centers present in the sample used in the analysis showcased in Figures 7.7 and 7.8 made direct estimation of $\mathbf{p}_\theta$ from the acquired images challenging, requiring a large amount of data per single value of θ and ϕ. However, it is possible that systematic errors arising from unequal conditions may have impacted the estimation of $\mathbf{p}_\theta$, thereby affecting the correct shifting of various frequency components in the Fourier domain, diminishing the actual resolution enhancement.

For future studies it will be crucial to estimate the frequency vector directly from the acquired image to avoid systematic errors. Additionally, employing an illumination vector closer to k_{Abbe} will require higher data volumes to compensate for the low transmission efficiency.

Conclusions

Reliable super-resolution methods in optical microscopy are crucial tools for contemporary applications, particularly in biology, where investigating small cellular structures with minimal photo-damage is essential. This thesis focused on a specific class of super-resolution techniques that exploit detected photon statistics to enhance spatial resolution by a factor of $\sqrt{j}$, where j is the highest detected moment evaluated, particularly suited in fluorescence microscopy. The most known is the Super-resolution Optical Fluctuation Imaging (SOFI), that was developed in classical optics framework.

In this work, we proposed a novel quantum model called Quantum Super-resolution Imaging by Photon Statistics (QSIPS), valid for both linear and On-Off detectors. QSIPS improves upon the classical SOFI approach by incorporating sub-Poissonian statistics through linear combinations of the cumulants of the detected photon distribution (see Equation 5.14). This model offers a robust super-resolution method that is applicable across any fluorescence intensity level and accommodates all non-Poissonian photon statistics as typical of different kind of emitters, from the super-Poissonian one of blinking quantum dots to the sub-Poissonian statistics of solid-state color centers such as Nitrogen Vacancy centers in nano-diamonds.

We have demonstrated the reliability of this model through both simulations and experimental validations, comparing the results with those obtained using the classical SOFI method (see Figures 5.1 and 5.2). Our findings highlight the superior performance of our QSIPS model, particularly in scenarios characterized by sub-Poissonian or weak super-Poissonian photon statistics, where the classical SOFI method fails to provide a reliable super-resolution enhancement. Furthermore, preliminary simulations and experimental studies suggest that QSIPS provides better local compression of the dynamic range across various super-resolution orders compared to the classical SOFI method (see Figures 5.4 and 5.5).

Additionally, this thesis analyzed the Signal-to-Noise Ratio (SNR) of the super-resolved signals provided by the QSIPS technique, considering both sub-Poissonian and super-Poissonian statistics for both linear and On-Off detectors in the presence of noise. Our analysis indicates that for sub-Poissonian emitters, maximizing the SNR requires limiting the number of excitation cycles performed by the emitter in the detector's integration time (see Figure 6.2a). However,

in real-world scenarios, when accounting for uncorrelated noise, it is essential to operate in a regime where the number of detected photons exceeds the noise level, as illustrated in Figure 6.4a. As it may be expected, low-noise and fast single photon detector become the most suited to collect large statistics of single-excitation signals.

However, a key finding from our analysis is that while high-order super-resolved signals experience SNR deterioration with an increasing number of detected photons in the integration time, second-order signals reach a constant SNR value that depends only on the system's detection probability (see Equations 6.29 and 6.30). This phenomenon enables second-order super-resolved imaging with single-photon emitters employing linear detectors, by compensating the presence of electronic noise with the accumulation of many photo-counts charges in the detector (see Figure 6.5). The experimental realization of this phenomenon is planned for future studies.

Furthermore, our study on the SNR of the super-resolved signals emitted from blinking quantum dots revealed significant insights into the nature of photon statistics. Specifically, the analysis of the Fano factor, as presented in Equation 6.11, suggests that parameters such as the blinking probability b, the number of excitation cycles K, and the ratio between the detector's integration time and the emitter's characteristic blinking time, denoted as M, are crucial in determining the nature of the photon statistics, accessing the performance of the super-resolution in the various configurations. This study has been instrumental in understanding the best experimental conditions to operate with, thus reducing the time needed and the amount of data to retrieve reliable super-resolved images.

In addition, our simulated analysis showed the feasibility of achieving super-resolved images using super-Poissonian emitters with On-Off detectors, provided that the operation conditions avoid saturation effects of the sensors (see Figures 6.10 and 6.11). This finding is significant because it paves the way for exploiting the high acquisition rate of On-Off detectors, such as SPADs, to obtain super-resolved images with super-Poissonian statistics in a fast and reliable way.

Furthermore, this thesis explored the integration of QSIPS, in the case of second order signal, with structured light illumination through both simulated and experimental work. This preliminary study compared our approach with the classical SOFI-SIM technique and found that the integration of structured light with the QSIPS method maintained its reliability and superior super-resolution enhancement even in low light conditions (see Figures 7.2 and 7.6). However, the experimental study of the effective super-resolution enhancement of the QSIPS-SIM technique with respect to the Abbe limit, reported in Figure 7.8 and Table 7.2, did not achieve the theoretical resolution enhancement of $2+\sqrt{2}$, likely due to inaccuracies in

the assessement of the frequency vector $\mathbf{p}_\theta$, performing nonetheless better than its classical counterpart.

Future studies will focus on the experimental realization of higher-order super-resolution images obtained with the QSIPS method integrated with structured light. Specifically, we aim to demonstrate the effective $j+\sqrt{j}$ resolution enhancement, employing both sub-Poissonian and super-Poissonian photon sources, overcoming the limitations of the present experiment. The super-resolution enhancement obtained with structured light, combined with the robustness of the QSIPS model under various light conditions, paves the way for a low-power and high-resolution imaging technique that can be valuable for future applications, particularly in biological contexts.

Appendix A

In the following section will be presented the proof of Equations 5.9 and 5.10 for a generic order j along with the intrinsic non-Poissonian nature of our quantum model.

A.1 Demonstration of super-resolution for a generic order j

Let us consider the cumulant generating function of the detected photon distribution for the α-th emitter, reported in Equation 5.4, and perform a change of variable $\xi_\alpha(t,\mathbf{r}) = 1-\eta_\alpha(\mathbf{r})+\eta_\alpha(\mathbf{r})e^t$:

$$\mathscr{C}_{\alpha,\eta}(\xi_\alpha(t,\mathbf{r})) = \log\left(\sum_{m=0}^{\infty}\xi_\alpha^m(t,\mathbf{r})P(m)\right). \tag{A.1}$$

We are interested in the derivative of order i of the cumulative generative function (i.e. the i-th order cumulant $c^{(i)}_{\alpha,\eta}(\mathbf{r})$) expressed in terms of $\xi_\alpha(t,\mathbf{r})$, therefore we can use the Faa di Bruno's formula [142] to assess the i-th order derivative of the composed function $\mathscr{C}_{\alpha,\eta}\left(\xi_\alpha(t,\mathbf{r})\right)$:

$$c^{(i)}_{\alpha,\eta}(\mathbf{r}) = \sum_{k=1}^{i}\frac{d^k\mathscr{C}_{\alpha,\eta}}{d\xi_\alpha^k}(\xi_\alpha(t,\mathbf{r}))|_{t=0}B_{i,k}\left(\xi_\alpha^{(1)}(0,\mathbf{r}),\ldots,\xi_\alpha^{(i-k+1)}(0,\mathbf{r})\right), \tag{A.2}$$

where $B_{i,k}\left(\xi_\alpha^{(1)}(0,\mathbf{r}),\ldots,\xi_\alpha^{(i-k+1)}(0,\mathbf{r})\right)$ represents the partial Bell polynomials [143]:

$$B_{i,k}(\xi_\alpha^{(1)}(0,\mathbf{r}),\ldots,\xi_\alpha^{(i-k+1)}(0,\mathbf{r})) = i!\sum_{j_1,j_2,\cdots,j_{i-k+1}}\prod_{l=1}^{i-k+1}\frac{\left[\xi_\alpha^{(i)}(0,\mathbf{r})\right]^{j_l}}{l!^{j_l}j_l!}, \tag{A.3}$$

with $j_1, j_2, \ldots, j_{i-k+1}$ being non negative integers satisfying:

$$j_1 + j_2 + \dots j_{i-k+1} = k, \tag{A.4}$$

$$j_1 + 2j_2 + \dots (i-k+1) j_{i-k+1} = i. \tag{A.5}$$

We observe that for every generic order of derivative i of $\xi_\alpha(t,\mathbf{r})$ respect to the parameter t and evaluated at $t = 0$, we have:

$$\xi_\alpha^{(i)}(0,\mathbf{r}) = \eta_\alpha(\mathbf{r}), \qquad i \in \mathbb{N}. \tag{A.6}$$

Substituting this result in Equation A.2 yields to:

$$c_{\alpha,\eta}^{(i)}(\mathbf{r}) = \sum_{k=1}^{i} \eta_\alpha^k(\mathbf{r}) \frac{d^k \mathscr{C}_{\alpha,\eta}}{d\xi_\alpha^k}(\xi_\alpha(t,\mathbf{r}))|_{t=0} S_{II}(i,k), \tag{A.7}$$

with $S_{II}(i,k)$ being the Stirling number of the second type:

$$S_{II}(i,k) = B_{i,k}(1,\dots,1) = \sum_{j=0}^{k} (-1)^{k-j} \frac{j^i}{(k-j)!\,j!}. \tag{A.8}$$

The coefficients $\beta_{i,j}$ in Equation 5.10 can be expressed in terms of the Stirling number of the first type:

$$\beta_{i,j} = \frac{1}{j!}\frac{d^j}{dx^j} \prod_{i=0}^{j-1} (x-i)|_{x=0} = \frac{1}{j!}\frac{d^j}{dx^j} \sum_{i=1}^{j} S_I(j,i) x^i|_{x=0} = S_I(i,j). \tag{A.9}$$

Performing a linear combination up to the order j of the cumulants reported in Equation A.7 with the coefficients $\beta_{i,j}$ of Equation A.9 we obtain:

$$\sum_{i=1}^{j} \beta_{i,j} c_{\alpha,\eta}^{(i)}(\mathbf{r}) = \sum_{i=1}^{j} S_I(i,j) \sum_{k=1}^{i} \eta_\alpha^k(\mathbf{r}) \frac{d^k \mathscr{C}_{\alpha,\eta}}{d\xi_\alpha^k}(\xi_\alpha(t,\mathbf{r}))|_{t=0} S_{II}(i,k). \tag{A.10}$$

Rearranging the summations, Equation A.10 becomes:

$$\sum_{i=1}^{j} \beta_{i,j} c_{\alpha,\eta}^{(i)}(\mathbf{r}) = \sum_{k=1}^{j} \eta_\alpha^k(\mathbf{r}) \frac{d^k \mathscr{C}_{\alpha,\eta}}{d\xi^k}(\xi_\alpha(t,\mathbf{r}))|_{t=0} \sum_{i=k}^{j} S_I(i,j) S_{II}(i,k). \tag{A.11}$$

Now, using the identity:

$$\sum_{i=k}^{j} S_I(i,j) S_{II}(i,k) = \delta_{j,k}, \tag{A.12}$$

Equation A.11 can be rewritten as:

$$\sum_{i=1}^{j} \beta_{i,j} c_{\alpha,\eta}^{(i)}(\mathbf{r}) = \eta_\alpha^j(\mathbf{r}) \frac{d^j \mathscr{C}_{\alpha,\eta}}{d\xi_\alpha^j} (\xi_\alpha(t,\mathbf{r}))\,|_{t=0}. \tag{A.13}$$

This relation demonstrates that a linear combination of cumulants up to order j, as described in Equation 5.9, results in terms solely proportional to the j-th power of the PSF ($\eta_\alpha^{(j)}(\mathbf{r})$). Specifically, the scaling factor $(d^j \mathscr{C}_{\alpha,\eta}/d\xi_\alpha^j)(\xi_\alpha(t,\mathbf{r}))\big|_{t=0}$ represents the same combination of cumulants but for the emitted photon distribution rather than the detected one.

To illustrate this, we can express the cumulant generating function of the emitted photon distribution $\mathscr{C}_\alpha(t)$, reported in Equation 5.2, performing a change of variable $\rho(t) = e^t$. This yields to the same generating function as reported in Equation A.1, but in this case, all the derivatives of $\rho(t)$ provides a factor of one instead of $\eta_\alpha(\mathbf{r})$ as in the detected photon distribution case (see Equation A.6):

$$\mathscr{C}_{\alpha,\eta}(\rho_\alpha(t)) = \log\left(\sum_{m=0}^{\infty} \rho_\alpha^m(t) P(m)\right), \tag{A.14}$$

$$\rho_\alpha^{(i)}(t) = 1, \qquad i \in \mathbb{N}. \tag{A.15}$$

Consequently, following the same calculations previously reported, we obtain:

$$\sum_{i=1}^{j} \beta_{i,j} c_\alpha^{(i)} = \frac{d^j \mathscr{C}_\alpha}{d\rho^j} (\rho(t))\,|_{t=0}. \tag{A.16}$$

Therefore, since:

$$\frac{d^j \mathscr{C}_{\alpha,\eta}}{d\xi_\alpha^j} (\xi_\alpha(t,\mathbf{r}))\,|_{t=0} = \frac{d^j \mathscr{C}_\alpha}{d\rho^j} (\rho(t))\,|_{t=0}, \tag{A.17}$$

as suggested by Equations A.1 and A.14, combining Equations A.13 and A.16 we obtain Equation 5.9.

Although the generating function of Equation A.1 is not a known generating function in the literature, it possesses specific properties. Particularly, to determine which combination

of cumulants is necessary to retrieve a super-resolved signal of order j, we can perform the j-th derivative of that generating function and evaluate it at $\xi = 1$ (or $t = 0$). This generating function can fully deconvolve the Binomial losses of optical systems and recover a pure combination of moments of the emitted photon distribution.

As mentioned in Section 5.1, the super-resolution formula presented here is applicable to every non-Poissonian emitter. The nature of this non-Poissonian behavior arises from the fact that considering Poissonian light sources, the scaling factor of the super-resolved signal (i.e. the factor multiplying $\eta_\alpha^j(\mathbf{r})$ in Equation A.13) is always zero for every $j > 1$.

We can demonstrate it by substituting the probability density function $P(m)$ of a Poissonian photon source such that $\langle m \rangle = \lambda$ into Equation A.1 for the emitted photon distribution, we have:

$$\mathscr{C}_{\alpha,\eta}(\xi_\alpha(t,\mathbf{r})) = \log\left(\sum_{m=0}^{\infty} \xi_\alpha^m(t,\mathbf{r})\frac{\lambda^m}{m!}e^{-\lambda}\right). \tag{A.18}$$

Taking the derivative with respect to $\xi_\alpha(t,\mathbf{r})$ of Equation A.18, we obtain:

$$\frac{d\mathscr{C}_{\alpha,\eta}}{d\xi_\alpha}(\xi_\alpha(t,\mathbf{r})) = \frac{1}{\sum_{m=0}^{\infty} \xi_\alpha^m(t,\mathbf{r})\frac{\lambda^m}{m!}e^{-\lambda}}\lambda \sum_{m=0}^{\infty} \xi_\alpha^m(t,\mathbf{r})\frac{\lambda^m}{m!}e^{-\lambda} = \lambda. \tag{A.19}$$

Since the first derivative has no dependence on the parameter t, all subsequent derivatives of this generating function will be zero, thereby preventing any super-resolved signal from a Poissonian source.

Appendix B

In Section 5.1.1, we discussed the feasibility of evaluating correlation functions using On-Off detectors. This appendix will elaborate on the methodology for performing such evaluations and delineate the experimental conditions under which this approach is valid. Moreover, we explore how to incorporate detection events unrelated to photons emitted by the source into the approximation of correlation functions.

B.1 Correlation functions in On-Off detectors

The general representation of the second-order correlation function in terms of the emitted photon probability distribution $P(m)$ at 0 time delay ($\tau = 0$) is:

$$g^{(2)}(0) = \frac{\langle m(m-1)\rangle}{\langle m\rangle^2} = \frac{\sum_{m=2}^{\infty} m(m-1)P(m)}{\left[\sum_{m=1}^{\infty} mP(m)\right]^2} = \frac{2P(2)+6P(3)+\ldots}{[P(1)+2P(2)+\ldots]^2}. \tag{B.1}$$

Now, let's consider a beam splitter with transmittance T and reflectance $R = 1-T$, with two outputs connected to two click detectors, A and B. Let ρ_A and ρ_B be the total efficiency (including losses in the optical path) of the two detectors.

The joint probability distribution of detecting κ_A photons in detector A and κ_B photons in detector B at zero time delay ($\tau = 0$) is:

$$\mathscr{P}(\kappa_A,\kappa_B)=\sum_{j_A=\kappa_A}^{\infty}\sum_{j_B=\kappa_B}^{\infty}\binom{j_A}{\kappa_A}\rho_A^{\kappa_A}(1-\rho_A)^{j_A-\kappa_A}\binom{j_B}{\kappa_B}\rho_B^{\kappa_B}(1-\rho_B)^{j_B-\kappa_B}\binom{j_A+j_B}{j_A}R^{j_A}T^{j_B}P(j_A+j_B). \tag{B.2}$$

We can define a quantity, $\varepsilon^{(2)}(\tau=0)$, as:

$$\varepsilon^{(2)}(0)=\frac{\sum_{\kappa_A=1}^{\infty}\sum_{\kappa_B=1}^{\infty}\mathscr{P}(\kappa_A,\kappa_B)}{\sum_{\kappa_A=1}^{\infty}\sum_{\kappa_B=0}^{\infty}\mathscr{P}(\kappa_A,\kappa_B)\sum_{\kappa_A=0}^{\infty}\sum_{\kappa_B=1}^{\infty}\mathscr{P}(\kappa_A,\kappa_B)}, \tag{B.3}$$

where the numerator indicates the probability of having at least one photon detected in detector A and one photon detected in detector B, known as the coincidence probability P_{AB}, while the denominator is the product of the probability of detecting at least one photon at each detector independently, respectively P_A and P_B. Therefore, $\varepsilon^{(2)}(0)$ can be written as:

$$\varepsilon^{(2)}(0)=\frac{P_{AB}}{P_AP_B}. \tag{B.4}$$

We can rewrite equation B.3 in terms of the efficiencies of the detectors and the reflectance and transmittance of the beamsplitter. In particular, we denote a generic probability $\eta_A=\rho_AR$ and $\eta_B=\rho_BT$ of detecting a photon, respectively, in detector A and B, which take into account all possible optical losses, including the effect of the beamsplitter and the PSF:

$$\varepsilon^{(2)}(0)=\frac{\sum_{m=2}^{\infty}[1-(1-\eta_A)^m-(1-\eta_B)^m+(1-\eta_A-\eta_B)^m]P(m)}{\sum_{m=1}^{\infty}[1-(1-\eta_A)^m]P(m)\sum_{l=1}^{\infty}[1-(1-\eta_B)^l]P(l)}. \tag{B.5}$$

Rearranging equation B.5 and considering the first terms of the series, we get:

$$\varepsilon^{(2)}(0)=\frac{2P(2)+6P(3)\left(1-\frac{1}{2}\eta_A-\frac{1}{2}\eta_B\right)+\ldots}{[P(1)+2P(2)\left(1-\frac{1}{2}\eta_A\right)+\ldots][P(1)+2P(2)\left(1-\frac{1}{2}\eta_B\right)+\ldots]}. \tag{B.6}$$

Comparing Equation B.1 with B.6, it becomes evident that the initial terms in the numerator and in each component of the denominator of $\varepsilon^{(2)}(0)$ precisely match those found in $g^{(2)}(0)$. As photon numbers increase, η_A and η_B emerge as corrective elements, signifying an inclination for the click detectors to underestimate higher-photon-number terms.

When detection efficiencies are extremely low, these corrections to terms associated with higher photon numbers become inconsequential, therefore we obtain:

$$\lim_{\eta_A,\eta_B\to 0} \varepsilon^{(2)}(0) = g^{(2)}(0). \tag{B.7}$$

Alternatively, if the source has very low multi-photon generation probabilities such that $P(1) \gg P(2) \gg P(m>2)$, then:

$$\varepsilon^{(2)}(0) \simeq \frac{2P(2)}{[P(1)]^2} \simeq g^{(2)}(0). \tag{B.8}$$

Similarly, we can express the third-order correlation evaluated $\tau_1 = 0$ and $\tau_2 = 0$ function as:

$$\begin{aligned} g^{(3)}(0,0) =& \frac{\langle m(m-1)(m-2)\rangle}{\langle m\rangle^3} = \frac{\sum_{m=3}^{\infty} m(m-1)(m-2)P(m)}{\left[\sum_{m=1}^{\infty} mP(m)\right]^3} \\ =& \frac{6P(3)+24P(4)+\ldots}{[P(1)+2P(2)+\ldots]^3}. \end{aligned} \tag{B.9}$$

By considering the joint probability distribution of detecting κ_A photons in detector A, κ_B in detector B, and κ_C in detector C at zero time delay between the detectors, we can express $\varepsilon^{(3)}(0,0)$ as:

$$\varepsilon^{(3)}(0,0) = \frac{\sum_{\kappa_A=1,\kappa_B=1,\kappa_C=1}^{\infty} \mathscr{P}(\kappa_A,\kappa_B,\kappa_C)}{\sum_{\substack{\kappa_A=1\\ \kappa_B=0\\ \kappa_C=0}}^{\infty} \mathscr{P}(\kappa_A,\kappa_B,\kappa_C) \sum_{\substack{\kappa_A=0\\ \kappa_B=1\\ \kappa_C=0}}^{\infty} \mathscr{P}(\kappa_A,\kappa_B,\kappa_C) \sum_{\substack{\kappa_A=0\\ \kappa_B=0\\ \kappa_C=1}} \mathscr{P}(\kappa_A,\kappa_B,\kappa_C)}. \tag{B.10}$$

Here, the numerator indicates the probability of having at least one photon detected in each of the detectors, known as three-photon coincidence P_{ABC}, and the denominator is the product of the probability of detecting one photon independently from the output of each detector, respectively P_A, P_B, P_C.

Expressing the joint probability function in terms of the detection probability η for each detector, we can write $\varepsilon^{(3)}(0,0)$ as:

$$\varepsilon^{(3)}(0,0) = \frac{P_{ABC}}{P_A P_B P_C}, \tag{B.11}$$

with:

$$\begin{aligned} P_{ABC} = \sum_{m=3}^{\infty} [1 - (1-\eta_A)^m - (1-\eta_B)^m - (1-\eta_C)^m \\ + (1-\eta_A-\eta_B)^m + (1-\eta_A-\eta_C)^m + (1-\eta_B-\eta_C)^m \\ - (1-\eta_A-\eta_B-\eta_C)^m] P(m), \end{aligned} \tag{B.12}$$

$$P_A = \sum_{m=1}^{\infty} [1 - (1-\eta_A)^m] P(m), \tag{B.13}$$

$$P_B = \sum_{m=1}^{\infty} [1 - (1-\eta_B)^m] P(m), \tag{B.14}$$

$$P_C = \sum_{m=1}^{\infty} [1 - (1-\eta_C)^m] P(m). \tag{B.15}$$

We can rearrange these factors in terms of detection probability and explicitly write the sums as:

$$P_{ABC} = 6P(3) + 24P(4)\left[1 - \frac{1}{2}\eta_A - \frac{1}{2}\eta_B - \frac{1}{2}\eta_C\right] + \dots \tag{B.16}$$

$$P_A = P(1) + 2P(2)\left[1 - \frac{1}{2}\eta_A\right] + \dots \tag{B.17}$$

$$P_B = P(1) + 2P(2)\left[1 - \frac{1}{2}\eta_B\right] + \dots \tag{B.18}$$

$$P_C = P(1) + 2P(2)\left[1 - \frac{1}{2}\eta_C\right] + \dots \tag{B.19}$$

Therefore:

$$\varepsilon^{(3)}(0,0) = \frac{6P(3) + 24P(4)\left[1 - \frac{1}{2}\eta_A - \frac{1}{2}\eta_B - \frac{1}{2}\eta_C\right] + \dots}{\prod_{i=A,B,C}\left(P(1) + 2P(2)[1 - \frac{1}{2}\eta_i] + \dots\right)}. \tag{B.20}$$

When considering the limit of low detection efficiency, $\varepsilon^{(3)}(0,0)$ approximates the third-order correlation function:

$$\lim_{\eta_A,\eta_B,\eta_C\to 0} \varepsilon^{(3)}(0,0) = g^{(3)}(0,0). \tag{B.21}$$

Similarly to the second-order case, when considering low multi-photon generation probabilities from the source ($P(1) \gg P(2) \gg P(3) \gg P(m>3)$), we have:

$$\varepsilon^{(3)}(0,0) \simeq \frac{6P(3)}{[P(1)]^3} \simeq g^{(3)}(0,0). \tag{B.22}$$

This reasoning can be extended to approximate the j-th order correlation function. Specifically, by considering a system consisting of j independent detectors, labeled from 0 to $j-1$ and represented in Figure B.1, we can evaluate the parameter $\varepsilon^{(j)}(\tau_1 = 0, \tau_2 = 0, \ldots, \tau_{j-1} = 0)$ as follows:

$$\varepsilon^{(j)}(\tau_1 = 0, \tau_2 = 0, \ldots, \tau_{j-1} = 0) = \frac{\sum_{\kappa_0=1,\ldots,\kappa_{j-1}=1}^{\infty} \mathscr{P}(\kappa_0, \kappa_1, \kappa_2, \ldots, \kappa_{j-1})}{\prod_{n=0}^{j-1} \sum_{\substack{\kappa_n=1 \\ \kappa_m=0 \\ n\neq m}}^{\infty} \mathscr{P}(\kappa_0, \kappa_1, \ldots, \kappa_{j-1})}, \tag{B.23}$$

which, under the same conditions as previously discussed, provides a good approximation of the j-th order correlation function. Consequently, it can be utilized to evaluate super-resolved signals up to order j.

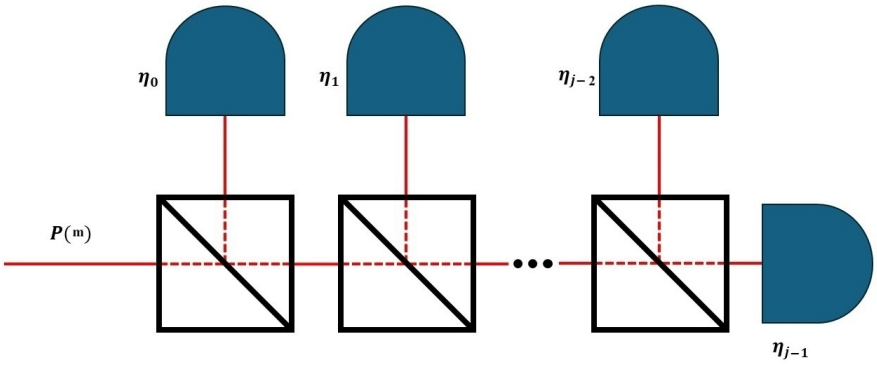

Figure B.1: *Detection scheme involving j independent On-Off detectors labeled from 0 to $j-1$. The photons emitted by a source, following the probability distribution function labeled as $P(m)$, pass through a series of $j-1$ beam splitters. By calculating the ratio between the coincidence events of all j detectors normalized by the product of all the independent detection probabilities, it is possible to evaluate an approximation of the j order correlation function.*

This general model can also be applied to wide-field On-Off sensors, such as SPAD arrays or EM-CCD cameras, as outlined in Section 3.2. Specifically, the concept involves substituting each detector in the beamsplitter configuration with a single pixel of the wide-field sensor. Generally, we can select a small area surrounding a fixed position and estimate the parameter $\varepsilon^{(j)}(\tau_1 = 0, \tau_2 = 0, \ldots, \tau_{j-1} = 0)$ between j pixels within that region.

Moreover, we can also incorporate a generic noise to the model. Specifically, we denote the probability of a click being due to a non-photon-related event as B. Therefore, the total probability of a click occurring in the i-th detector is expressed as:

$$P_i = P_i^{(S)}(1-B) + B. \tag{B.24}$$

Here, $P_i^{(S)}$ denotes the probability of a click resulting from a real signal event. Considering a system of independent detectors where the noise is uncorrelated and uniform in magnitude, we can express the probability of observing two or three coincidences as follows:

$$P_{ij} = P_{ij}^{(S)}(1-B)^2 + B(1-B)\left[P_i^{(S)} + P_j^{(S)}\right] + B^2, \tag{B.25}$$

$$\begin{aligned} P_{ijk} =& P_{ijk}^{(S)}(1-B)^3 + B(1-B)^2\left[P_{ij}^{(S)} + P_{ik}^{(S)} + P_{jk}^{(S)}\right] \\ &+ B^2(1-B)\left[P_i^{(S)} + P_j^{(S)} + P_k^{(S)}\right] + B^3, \end{aligned} \tag{B.26}$$

where $P_{ij}^{(S)}$ and $P_{ijk}^{(S)}$ denote the probabilities of detecting two and three coincidence events, respectively, due to real signal detection. The general formula for the coincidence probability involving j independent detectors, which display uncorrelated noise, is given by:

$$P_{01\ldots j-1} = \sum_{i=0}^{j} \gamma_{j,i} B^i (1-B)^{j-i}, \tag{B.27}$$

where $\gamma_{j,i}$ represent all possible combinations of simultaneous click events between $j-i$ detectors in a system comprising j detectors. For instance, in the case of third-order coincidences we have:

$$\begin{aligned} \gamma_{3,0} &= P_{ABC}^{(S)}, \\ \gamma_{3,1} &= P_{AB}^{(S)} + P_{BC}^{(S)} + P_{AC}^{(S)}, \\ \gamma_{3,2} &= P_A^{(S)} + P_B^{(S)} + P_C^{(S)}, \\ \gamma_{3,3} &= 1. \end{aligned} \tag{B.28}$$

Bibliography

[1] Stefan W Hell and Jan Wichmann. "Breaking the diffraction resolution limit by stimulated emission: stimulated-emission-depletion fluorescence microscopy". In: *Optics letters* 19.11 (1994), pp. 780–782. DOI: 10.1364/OL.19.000780.

[2] WE Moerner and David P Fromm. "Methods of single-molecule fluorescence spectroscopy and microscopy". In: *Review of Scientific instruments* 74.8 (2003), pp. 3597–3619. DOI: 10.1063/1.1589587.

[3] Eric Betzig et al. "Imaging intracellular fluorescent proteins at nanometer resolution". In: *science* 313.5793 (2006), pp. 1642–1645. DOI: 10.1126/science.1127344.

[4] Stefan W Hell. "Nanoscopy with focused light". In: *Annalen der Physik* 527.7-8 (2015), pp. 423–445. DOI: 10.1002/andp.201500805.

[5] Osip Schwartz et al. "Superresolution microscopy with quantum emitters". In: *Nano letters* 13.12 (2013), pp. 5832–5836. DOI: 10.1021/nl402552m.

[6] Thomas Dertinger et al. "Fast, background-free, 3D super-resolution optical fluctuation imaging (SOFI)". In: *Proceedings of the National Academy of Sciences* 106.52 (2009), pp. 22287–22292. DOI: 10.1073/pnas.0907866106.

[7] D Gatto Monticone et al. "Beating the Abbe diffraction limit in confocal microscopy via nonclassical photon statistics". In: *Physical review letters* 113.14 (2014), p. 143602. DOI: 10.1103/PhysRevLett.113.143602.

[8] Mats GL Gustafsson. "Surpassing the lateral resolution limit by a factor of two using structured illumination microscopy". In: *Journal of microscopy* 198.2 (2000), pp. 82–87. DOI: 10.1046/j.1365-2818.2000.00710.x.

[9] Giorgio Brida, Marco Genovese, and Ivano Ruo Berchera. "Experimental realization of sub-shot-noise quantum imaging". In: *Nature Photonics* 4.4 (2010), pp. 227–230. DOI: 10.1038/nphoton.2010.29.

[10] Morgan W Mitchell, Jeff S Lundeen, and Aephraem M Steinberg. "Super-resolving phase measurements with a multiphoton entangled state". In: *Nature* 429.6988 (2004), pp. 161–164. DOI: 10.1038/nature02493.

[11] Ömer Bayraktar et al. "Quantum-polarization state tomography". In: *Physical Review A* 94.2 (2016), p. 020105. DOI: 10.1103/PhysRevA.94.020105.

[12] Florian Dolde et al. "Electric-field sensing using single diamond spins". In: *Nature Physics* 7.6 (2011), pp. 459–463. DOI: 10.1038/nphys1969.

[13] Margaret E Robinson et al. "Optically detected magnetic resonance for selective imaging of diamond nanoparticles". In: *Analytical chemistry* 90.1 (2018), pp. 769–776. DOI: 10.1021/acs.analchem.7b03157.

[14] Wesley Wei-Wen Hsiao et al. “Fluorescent nanodiamond: a versatile tool for long-term cell tracking, super-resolution imaging, and nanoscale temperature sensing”. In: *Accounts of chemical research* 49.3 (2016), pp. 400–407. DOI: 10.1021/acs.accounts.5b00484.

[15] Matthew E Trusheim and Dirk Englund. “Wide-field strain imaging with preferentially aligned nitrogen-vacancy centers in polycrystalline diamond”. In: *New Journal of Physics* 18.12 (2016), p. 123023. DOI: 10.1088/1367-2630/aa5040.

[16] ED Lopaeva et al. “Experimental realization of quantum illumination”. In: *Physical review letters* 110.15 (2013), p. 153603. DOI: 10.1103/PhysRevLett.110.153603.

[17] Seth Lloyd. “Enhanced sensitivity of photodetection via quantum illumination”. In: *Science* 321.5895 (2008), pp. 1463–1465. DOI: 10.1126/science.1160627.

[18] Ernst Abbe. “Beiträge zur Theorie des Mikroskops und der mikroskopischen Wahrnehmung”. In: *Archiv für mikroskopische Anatomie* 9.1 (1873), pp. 413–468. DOI: 10.1007/BF02956173.

[19] Mickaël Lelek et al. “Single-molecule localization microscopy”. In: *Nature Reviews Methods Primers* 1.1 (2021), p. 39. DOI: 10.1038/s43586-021-00038-x.

[20] Adrien C Descloux et al. “Experimental combination of super-resolution optical fluctuation imaging with structured illumination microscopy for large fields-of-view”. In: *Acs Photonics* 8.8 (2021), pp. 2440–2449. DOI: 10.1021/acsphotonics.1c00668.

[21] Anton Classen et al. “Superresolution via structured illumination quantum correlation microscopy”. In: *Optica* 4.6 (2017), pp. 580–587. DOI: 10.1364/OPTICA.4.000580.

[22] Thomas Dertinger et al. “Advances in superresolution optical fluctuation imaging (SOFI)”. In: *Quarterly reviews of biophysics* 46.2 (2013), pp. 210–221. DOI: 10.1017/S0033583513000036.

[23] K Brunner et al. “Photoluminescence from a single GaAs/AlGaAs quantum dot”. In: *Physical review letters* 69.22 (1992), p. 3216. DOI: 10.1103/PhysRevLett.69.3216.

[24] Katja Beha et al. “Optimum photoluminescence excitation and recharging cycle of single nitrogen-vacancy centers in ultrapure diamond”. In: *Physical review letters* 109.9 (2012), p. 097404. DOI: 10.1103/PhysRevLett.109.097404.

[25] Zhiliang Yuan et al. “Electrically driven single-photon source”. In: *science* 295.5552 (2002), pp. 102–105. DOI: 10.1126/science.1066790.

[26] Jacopo Forneris et al. “Electrical control of deep NV centers in diamond by means of sub-superficial graphitic micro-electrodes”. In: *Carbon* 113 (2017), pp. 76–86. DOI: 10.1016/j.carbon.2016.11.031.

[27] Roy J Glauber. “The quantum theory of optical coherence”. In: *Physical Review* 130.6 (1963), p. 2529. DOI: 10.1103/PhysRev.130.2529.

[28] Pierre Meystre and Marlan O Scully. *Quantum optics*. Springer, 2021.

[29] Anthony Mark Fox. *Quantum optics: an introduction*. Vol. 15. Oxford University Press, USA, 2006.

[30] Weidong Zhou and James J Coleman. “Semiconductor quantum dots”. In: *Current Opinion in Solid State and Materials Science* 20.6 (2016), pp. 352–360. DOI: 10.1016/j.cossms.2016.06.006.

[31] Ron Gill, Maya Zayats, and Itamar Willner. “Semiconductor quantum dots for bioanalysis”. In: *Angewandte Chemie International Edition* 47.40 (2008), pp. 7602–7625. DOI: 10.1002/anie.200800169.

[32] Lijia Shao, Yanfang Gao, and Feng Yan. “Semiconductor quantum dots for biomedicial applications”. In: *Sensors* 11.12 (2011), pp. 11736–11751. DOI: 10.3390/s111211736.

[33] Catherine J Murphy. “Peer reviewed: optical sensing with quantum dots”. In: *Analytical Chemistry* 74.19 (2002), 520–A. DOI: 10.1021/ac022124v.

[34] Charles Kittel and Paul McEuen. *Introduction to solid state physics*. John Wiley & Sons, 2018.

[35] VG Reshma and PV Mohanan. “Quantum dots: Applications and safety consequences”. In: *Journal of Luminescence* 205 (2019), pp. 287–298. DOI: 10.1016/j.jlumin.2018.09.015.

[36] Efros, Alexander L., and David J. Nesbitt. “Origin and control of blinking in quantum dots”. In: *Nature nanotechnology* 11.8 (2016), pp. 661–671. DOI: 10.1038/nnano.2016.140.

[37] Ken T Shimizu et al. “Blinking statistics in single semiconductor nanocrystal quantum dots”. In: *Physical Review B* 63.20 (2001), p. 205316. DOI: 10.1103/PhysRevB.63.205316.

[38] Igor Sergeevich Osad’ko. “Blinking fluorescence of single semiconductor nanocrystals: basic experimental facts and theoretical models of blinking”. In: *Physics-Uspekhi* 59.5 (2016), p. 462. DOI: 10.3367/UFNe.2015.12.037672.

[39] S Lagomarsino et al. “Creation of silicon-vacancy color centers in diamond by ion implantation”. In: *Frontiers in Physics* 8 (2021), p. 601362. DOI: 10.3389/fphy.2020.601362.

[40] Elena Nieto Hernández et al. “Efficiency Optimization of Ge-V Quantum Emitters in Single-Crystal Diamond upon Ion Implantation and HPHT Annealing”. In: *Advanced Quantum Technologies* (2023), p. 2300010. DOI: 10.1002/qute.202300010.

[41] JO Orwa et al. “Engineering of nitrogen-vacancy color centers in high purity diamond by ion implantation and annealing”. In: *Journal of applied physics* 109.8 (2011). DOI: 10.1063/1.3573768.

[42] Romana Schirhagl et al. “Nitrogen-vacancy centers in diamond: nanoscale sensors for physics and biology”. In: *Annual review of physical chemistry* 65 (2014), pp. 83–105. DOI: 10.1146/annurev-physchem-040513-103659.

[43] Sviatoslav Ditalia Tchernij et al. “Spectral features of Pb-related color centers in diamond–a systematic photoluminescence characterization”. In: *New Journal of Physics* 23.6 (2021), p. 063032. DOI: 10.1088/1367-2630/ac038a.

[44] Stefania Castelletto and Alberto Boretti. “Silicon carbide color centers for quantum applications”. In: *Journal of Physics: Photonics* 2.2 (2020), p. 022001. DOI: 10.1088/2515-7647/ab77a2.

[45] Marina Radulaski et al. “Scalable quantum photonics with single color centers in silicon carbide”. In: *Nano letters* 17.3 (2017), pp. 1782–1786. DOI: 10.1021/acs.nanolett.6b05102.

[46] Alrik Durand et al. “Broad diversity of near-infrared single-photon emitters in silicon”. In: *Physical review letters* 126.8 (2021), p. 083602. DOI: 10.1103/PhysRevLett.126.083602.

[47] Yoann Baron et al. “Detection of single W-centers in silicon”. In: *ACS Photonics* 9.7 (2022), pp. 2337–2345. DOI: 10.1021/acsphotonics.2c00336.

[48] W Redjem et al. “Single artificial atoms in silicon emitting at telecom wavelengths”. In: *Nature Electronics* 3.12 (2020), pp. 738–743. DOI: 10.1038/s41928-020-00499-0.

[49] D Yu Fedyanin and Mario Agio. “Ultrabright single-photon source on diamond with electrical pumping at room and high temperatures”. In: *New Journal of Physics* 18.7 (2016), p. 073012. DOI: 10.1088/1367-2630/18/7/073012.

[50] Giulia Tomagra et al. “Diamond-based sensors for in vitro cellular radiobiology: Simultaneous detection of cell exocytic activity and ionizing radiation”. In: *Biosensors and Bioelectronics* 220 (2023), p. 114876. DOI: 10.1016/j.bios.2022.114876.

[51] Jana Svítková et al. “Chemical modification of boron-doped diamond electrodes for applications to biosensors and biosensing”. In: *Critical reviews in analytical chemistry* 46.3 (2016), pp. 248–256. DOI: 10.1080/10408347.2015.1082125.

[52] Xianfeng Chen and Wenjun Zhang. “Diamond nanostructures for drug delivery, bioimaging, and biosensing”. In: *Chemical Society Reviews* 46.3 (2017), pp. 734–760. DOI: 10.1039/C6CS00109B.

[53] Yuichiro Matsuzaki et al. “Optically detected magnetic resonance of high-density ensemble of NV- centers in diamond”. In: *Journal of Physics: Condensed Matter* 28.27 (2016), p. 275302. DOI: 10.1088/0953-8984/28/27/275302.

[54] Giulia Petrini et al. “Is a quantum biosensing revolution approaching? Perspectives in NV-assisted current and thermal biosensing in living cells”. In: *Advanced Quantum Technologies* 3.12 (2020), p. 2000066. DOI: 10.1002/qute.202000066.

[55] Giulia Petrini et al. “Nanodiamond–quantum sensors reveal temperature variation associated to hippocampal neurons firing”. In: *Advanced Science* 9.28 (2022), p. 2202014. DOI: 10.1002/advs.202202014.

[56] Adam Gali, Maria Fyta, and Efthimios Kaxiras. “Ab initio supercell calculations on nitrogen-vacancy center in diamond: Electronic structure and hyperfine tensors”. In: *Physical Review B* 77.15 (2008), p. 155206. DOI: 10.1103/PhysRevB.77.155206.

[57] NB Manson, JP Harrison, and MJ Sellars. “Nitrogen-vacancy center in diamond: Model of the electronic structure and associated dynamics”. In: *Physical Review B* 74.10 (2006), p. 104303. DOI: 10.1103/PhysRevB.74.104303.

[58] Marcus W Doherty et al. “The nitrogen-vacancy colour centre in diamond”. In: *Physics Reports* 528.1 (2013), pp. 1–45. DOI: 10.1016/j.physrep.2013.02.001.

[59] A Jarmola et al. “Temperature-and magnetic-field-dependent longitudinal spin relaxation in nitrogen-vacancy ensembles in diamond”. In: *Physical review letters* 108.19 (2012), p. 197601. DOI: 10.1103/PhysRevLett.108.197601.

[60] CL Degen. “Scanning magnetic field microscope with a diamond single-spin sensor”. In: *Applied Physics Letters* 92.24 (2008). DOI: 10.1063/1.2943282.

[61] Solveig Felton et al. “Electron paramagnetic resonance studies of the neutral nitrogen vacancy in diamond”. In: *Physical Review B* 77.8 (2008), p. 081201. DOI: 10.1103/PhysRevB.77.081201.

[62] T Meguro et al. “Creation of nanodiamonds by single impacts of highly charged ions upon graphite”. In: *Applied Physics Letters* 79.23 (2001), pp. 3866–3868. DOI: 10.1063/1.1424047.

[63] Nicholas Nunn et al. “Nanodiamond: a high impact nanomaterial”. In: *Current Opinion in Solid State and Materials Science* 21.1 (2017), pp. 1–9. DOI: 10.1016/j.cossms.2016.06.008.

[64] Carlo Bradac. “Nanoscale optical trapping: a review”. In: *Advanced Optical Materials* 6.12 (2018), p. 1800005. DOI: 10.1002/adom.201800005.

[65] Tobias Schaetz. “Trapping ions and atoms optically”. In: *Journal of Physics B: Atomic, Molecular and Optical Physics* 50.10 (2017), p. 102001. DOI: 10.1088/1361-6455/aa69b2.

[66] JD Weinstein and KG Libbrecht. “Microscopic magnetic traps for neutral atoms”. In: *Physical Review A* 52.5 (1995), p. 4004. DOI: 10.1103/PhysRevA.52.4004.

[67] Amira M Eltony et al. “Technologies for trapped-ion quantum information systems: Progress toward scalability with hybrid systems”. In: *Quantum information processing* 15 (2016), pp. 5351–5383. DOI: 10.1007/s11128-016-1298-8.

[68] David S Weiss and Mark Saffman. “Quantum computing with neutral atoms”. In: *Physics Today* 70.7 (2017), pp. 44–50. DOI: 10.1063/PT.3.3626.

[69] Helmut Ritsch et al. “Cold atoms in cavity-generated dynamical optical potentials”. In: *Reviews of Modern Physics* 85.2 (2013), pp. 553–601. DOI: 10.1103/RevModPhys.85.553.

[70] Christophe Couteau. “Spontaneous parametric down-conversion”. In: *Contemporary Physics* 59.3 (2018), pp. 291–304. DOI: 10.1080/00107514.2018.1488463.

[71] Lukas G Helt et al. “Spontaneous four-wave mixing in microring resonators”. In: *Optics letters* 35.18 (2010), pp. 3006–3008. DOI: doi.org/10.1364/OL.35.003006.

[72] Lijian Zhang et al. “Heralded generation of single photons in pure quantum states”. In: *Journal of Modern Optics* 59.17 (2012), pp. 1525–1537. DOI: 10.1080/09500340.2012.679707.

[73] Matthew J Collins et al. “Integrated spatial multiplexing of heralded single-photon sources”. In: *Nature communications* 4.1 (2013), p. 2582. DOI: 10.1038/ncomms3582.

[74] Galan Moody et al. “Chip-scale nonlinear photonics for quantum light generation”. In: *AVS Quantum Science* 2.4 (2020). DOI: 10.1116/5.0020684.

[75] Alessia Stefano, Luca Zatti, and Marco Liscidini. “Broadband Spontaneous Parametric Downconversion in Reconfigurable Poled Linearly-Uncoupled Resonators”. In: *arXiv preprint arXiv:2406.18196* (2024). DOI: 10.48550/arXiv.2406.18196.

[76] Aron Vanselow et al. “Ultra-broadband SPDC for spectrally far separated photon pairs”. In: *Optics letters* 44.19 (2019), pp. 4638–4641. DOI: 10.1364/OL.44.004638.

[77] Zhiyuan Zhou and Bao-Sen Shi. “Generation and Manipulation of Nonclassical Photon Sources in Nonlinear Processes”. In: Nov. 2019. ISBN: 978-1-83880-353-7. DOI: 10.5772/intechopen.90268.

[78] Bo Zhang, Josiane Zerubia, and Jean-Christophe Olivo-Marin. “Gaussian approximations of fluorescence microscope point-spread function models”. In: *Applied optics* 46.10 (2007), pp. 1819–1829. DOI: 10.1364/AO.46.001819.

[79] Jerome Mertz. *Introduction to optical microscopy*. Cambridge University Press, 2019.

[80] Max Born and Emil Wolf. *Principles of optics: electromagnetic theory of propagation, interference and diffraction of light*. Elsevier, 2013.

[81] Noah Gray. “Knowing the limit”. In: *Nature Cell Biology* 11.1 (2009), S8–S8. DOI: 10.1038/ncb1940.

[82] Shunsuke Yokozeki. “Moiré fringes”. In: *Optics and Lasers in Engineering* 3.1 (1982), pp. 15–27. DOI: 10.1016/0143-8166(82)90012-4.

[83] Amit Lal, Chunyan Shan, and Peng Xi. “Structured illumination microscopy image reconstruction algorithm”. In: *IEEE Journal of Selected Topics in Quantum Electronics* 22.4 (2016), pp. 50–63. DOI: 10.1109/JSTQE.2016.2521542.

[84] N. Waltham. “CCD and CMOS sensors”. In: 9 (2013), pp. 423–442. DOI: 10.1007/978-1-4614-7804-1_23.

[85] Oxford Instruments. *CCD Sensor Architectures*. 2023. URL: https://andor.oxinst.com/learning/view/article/ccd-sensor-architectures.

[86] DE Groom et al. “Quantum efficiency modeling for a thick back-illuminated astronomical CCD”. In: *Journal of Applied Physics* 122.5 (2017). DOI: 10.1063/1.4986506.

[87] Karsten Sperlich and Heinrich Stolz. “Quantum efficiency measurements of (EM) CCD cameras: high spectral resolution and temperature dependence”. In: *Measurement Science and Technology* 25.1 (2013), p. 015502. DOI: 10.1088/0957-0233/25/1/015502.

[88] Kenji Irie et al. “A model for measurement of noise in CCD digital-video cameras”. In: *Measurement Science and Technology* 19.4 (2008), p. 045207. DOI: 10.1088/0957-0233/19/4/045207.

[89] G. Prigozhin et al. “Latest results for a fast low noise CCD readout based on pJFET”. In: 12191 (2022), pp. 121911D - 121911D–8. DOI: 10.1117/12.2630166.

[90] P. Orel et al. “X-ray speed reading with the MCRC: a low noise CCD readout ASIC enabling readout speeds of 5 Mpixel/s/channel”. In: 12191 (2022), pp. 1219124 - 1219124–18. DOI: 10.1117/12.2629049.

[91] Yu-Bing Lv et al. “Optimization designed frame transfer area array sensor with vertical antiblooming structure by the CAD tools”. In: *International Symposium on Photoelectronic Detection and Imaging 2009: Advances in Imaging Detectors and Applications*. Vol. 7384. SPIE. 2009, pp. 534–540. DOI: https://doi.org/10.1117/12.835736.

[92] M. Bigas et al. “Review of CMOS image sensors”. In: *Microelectron. J.* 37 (2006), pp. 433–451. DOI: 10.1016/J.MEJO.2005.07.002.

[93] Ibrahima Djite et al. “Theoretical models of modulation transfer function, quantum efficiency, and crosstalk for CCD and CMOS image sensors”. In: *IEEE Transactions on Electron Devices* 59.3 (2012), pp. 729–737. DOI: 10.1109/TED.2011.2176493.

[94] Olli E Setälä et al. “CMOS Image Sensor for Broad Spectral Range with> 90% Quantum Efficiency”. In: *Small* 19.47 (2023), p. 2304001. DOI: 10.1002/smll.202304001.

[95] Shinichi Yoshimura et al. “A 48 kframe/s CMOS image sensor for real-time 3-D sensing and motion detection”. In: *2001 IEEE International Solid-State Circuits Conference. Digest of Technical Papers. ISSCC (Cat. No.01CH37177)* (2001), pp. 94–95. DOI: 10.1109/ISSCC.2001.912561.

[96] Wilson W. S. Chan, J. Sin, and S. Wong. “A novel crosstalk isolation structure for bulk CMOS power IC’s”. In: *IEEE Transactions on Electron Devices* 45 (1998), pp. 1580–1586. DOI: 10.1109/16.701492.

[97] Shoji Kawahito and Min-Woong Seo. “Noise reduction effect of multiple-sampling-based signal-readout circuits for ultra-low noise CMOS image sensors”. In: *Sensors* 16.11 (2016), p. 1867. DOI: 10.3390/s16111867.

[98] Min-Woong Seo et al. “A 0.27 e-rms read noise 220-μV/e-conversion gain reset-gateless CMOS image sensor with 0.11-μm CIS process”. In: *IEEE Electron Device Letters* 36.12 (2015), pp. 1344–1347. DOI: 10.1109/LED.2015.2496359.

[99] Edmund Optics. *Understanding Camera Sensors for Machine Vision Applications*. Accessed: 2023-09-28. 2023. URL: https://www.edmundoptics.com/knowledge-center/application-notes/imaging/understanding-camera-sensors-for-machine-vision-applications/.

[100] A. J. Miller et al. “Demonstration of a low-noise near-infrared photon counter with multiphoton discrimination”. In: *Applied Physics Letters* 83 (2003), pp. 791–793. DOI: 10.1063/1.1596723.

[101] Joel N Ullom and Douglas A Bennett. “Review of superconducting transition-edge sensors for x-ray and gamma-ray spectroscopy”. In: *Superconductor Science and Technology* 28.8 (2015), p. 084003. DOI: 10.1088/0953-2048/28/8/084003.

[102] Massachusetts Institute of Technology. *Transition Edge Sensors (TES)*. 2014. URL: https://web.mit.edu/figueroagroup/ucal/ucal_tes/.

[103] D. Rosenberg et al. “Noise-free high-efficiency photon-number-resolving detectors”. In: *Phys. Rev. A* 71 (2005), p. 061803. DOI: 10.1103/PhysRevA.71.061803.

[104] D Fukuda et al. “Photon number resolving detection with high speed and high quantum efficiency”. In: *Metrologia* 46.4 (2009), S288. DOI: 10.1088/0026-1394/46/4/S29.

[105] A. E. Lita, A. J. Miller, and S. W. Nam. “Counting near-infrared single-photons with 95% efficiency”. In: *Opt. Express* 16 (2008), pp. 3032–3040. DOI: 10.1364/OE.16.003032.

[106] D. Rosenberg et al. “Long-distance decoy-state quantum key distribution in optical fiber”. In: *Phys. Rev. Lett.* 98 (2007), p. 010503. DOI: 10.1103/PhysRevLett.98.010503.

[107] G. Di Giuseppe et al. “Direct observation of photon pairs at a single output port of a beam-splitter interferometer”. In: *Phys. Rev. A* 68 (2003), p. 063817. DOI: 10.1103/PhysRevA.68.063817.

[108] D Fukuda et al. “Confocal microscopy imaging with an optical transition edge sensor”. In: *Journal of Low Temperature Physics* 193 (2018), pp. 1228–1235. DOI: 10.1007/s10909-018-1938-8.

[109] Kazuki Niwa et al. “Few-photon color imaging using energy-dispersive superconducting transition-edge sensor spectrometry”. In: *Scientific Reports* 7.1 (2017), p. 45660. DOI: 10.1038/srep45660.

[110] K. Harpsoe, M. Andersen, and Per Kjaegaard. “Bayesian Photon Counting with EMCCDs”. In: (2011). DOI: 10.1051/0004-6361/201117089.

[111] Teledyne Princeton Instruments. *EMCCDs: The Basics*. https://www.princetoninstruments.com/learn/camera-fundamentals/emccds-the-basics. 2024.

[112] N. Bush et al. “Measurement and optimization of clock-induced charge in electron multiplying charge-coupled devices”. In: *Journal of Astronomical Telescopes, Instruments, and Systems* 7 (2021), pp. 016002–016002. DOI: 10.1117/1.JATIS.7.1.016002.

[113] Dejiang Wang et al. “Effects of electron multiplication on the CCD SNR in remote sensing application”. In: *Optik* 124 (2013), pp. 4832–4835. DOI: 10.1016/J.IJLEO.2013.02.037.

[114] A. Avella et al. “Absolute calibration of an EMCCD camera by quantum correlation, linking photon counting to the analog regime”. In: *Opt. Lett.* 41.8 (Apr. 2016), pp. 1841–1844. DOI: 10.1364/OL.41.001841.

[115] G. Acconcia et al. “Note: Fully integrated active quenching circuit achieving 100 MHz count rate with custom technology single photon avalanche diodes.” In: *The Review of scientific instruments* 88 2 (2017), p. 026103. DOI: 10.1063/1.4975598.

[116] National Institute of Standards and Technology. *Light fantastic: Counting single photons at unprecedented rates*. https://www.nist.gov/news-events/news/2021/04/light-fantastic-counting-single-photons-unprecedented-rates. Apr. 2021.

[117] Chen Wang et al. “Afterpulsing effects in SPAD-based photon-counting communication system”. In: *Optics Communications* (2019). DOI: 10.1016/J.OPTCOM.2019.03.039.

[118] A. Ziarkash et al. “Comparative study of afterpulsing behavior and models in single photon counting avalanche photo diode detectors”. In: *Scientific Reports* 8 (2017). DOI: 10.1038/s41598-018-23398-z.

[119] Charlotte Hopkinson et al. “A combined fluorescence lifetime and depth imaging system for medical imaging and surgical guidance”. In: 12368 (2023), pp. 1236808 - 1236808–9. DOI: 10.1117/12.2648431.

[120] Chao Zhang et al. “A 30-frames/s, 252 $\times$ 144 SPAD Flash LiDAR With 1728 Dual-Clock 48.8-ps TDCs, and Pixel-Wise Integrated Histogramming”. In: *IEEE Journal of Solid-State Circuits* 54.4 (2019), pp. 1137–1151. DOI: 10.1109/JSSC.2018.2883720.

[121] J. Bienfang et al. “Free-space quantum key distribution at GHz repetition rates”. In: 6476 (2007). DOI: 10.1117/12.713630.

[122] Mirko Sanzaro et al. “Single-photon avalanche diodes in a 0.16 μm BCD technology with sharp timing response and red-enhanced sensitivity”. In: *IEEE Journal of Selected Topics in Quantum Electronics* 24.2 (2017), pp. 1–9. DOI: 10.1109/JSTQE.2017.2762464.

[123] Francesco Ceccarelli et al. “152-dB dynamic range with a large-area custom-technology single-photon avalanche diode”. In: *IEEE Photonics Technology Letters* 30.4 (2018), pp. 391–394. DOI: 10.1109/LPT.2018.2792781.

[124] Risheng Cheng et al. “Epitaxial niobium nitride superconducting nanowire single-photon detectors”. In: *Applied Physics Letters* 117.13 (2020). DOI: 10.1063/5.0018818.

[125] Archan Banerjee et al. “Characterisation of amorphous molybdenum silicide (MoSi) superconducting thin films and nanowires”. In: *Superconductor Science and Technology* 30.8 (2017), p. 084010. DOI: 10.1088/1361-6668/aa76d8.

[126] Emma E Wollman et al. “UV superconducting nanowire single-photon detectors with high efficiency, low noise, and 4 K operating temperature”. In: *Optics express* 25.22 (2017), pp. 26792–26801. DOI: 10.1364/OE.25.026792.

[127] Hiroyuki Shibata et al. “SNSPD with ultimate low system dark count rate using various cold filters”. In: *IEEE Transactions on Applied Superconductivity* 27.4 (2016), pp. 1–4. DOI: 10.1109/TASC.2016.2631947.

[128] Boris Korzh et al. “Demonstration of sub-3 ps temporal resolution with a superconducting nanowire single-photon detector”. In: *Nature Photonics* 14.4 (2020), pp. 250–255. DOI: 10.1038/s41566-020-0589-x.

[129] Jin Chang et al. “Efficient mid-infrared single-photon detection using superconducting NbTiN nanowires with high time resolution in a Gifford-McMahon cryocooler”. In: *Photonics Research* 10.4 (2022), pp. 1063–1070. DOI: 10.1364/PRJ.437834.

[130] Jascha A Lau et al. “Superconducting single-photon detectors in the mid-infrared for physical chemistry and spectroscopy”. In: *Chemical Society Reviews* 52.3 (2023), pp. 921–941. DOI: 10.1039/D1CS00434D.

[131] Bakhrom G Oripov et al. “A superconducting nanowire single-photon camera with 400,000 pixels”. In: *Nature* 622.7984 (2023), pp. 730–734. DOI: 10.1038/s41586-023-06550-2.

[132] Jason P Allmaras et al. “Demonstration of a thermally coupled row-column snspd imaging array”. In: *Nano letters* 20.3 (2020), pp. 2163–2168. DOI: 10.1021/acs.nanolett.0c00246.

[133] Emma E Wollman et al. “Recent advances in superconducting nanowire single-photon detector technology for exoplanet transit spectroscopy in the mid-infrared”. In: *Journal of Astronomical Telescopes, Instruments, and Systems* 7.1 (2021), pp. 011004–011004. DOI: 10.1117/1.JATIS.7.1.011004.

[134] Hamamatsu Photonics. *High-speed 2-dimensional Optical Line Sensor C15550-22UP*. 2024. URL: https://www.hamamatsu.com/content/dam/hamamatsu-photonics/sites/documents/99_SALES_LIBRARY/sys/SCAS0166E_C15550-22UP.pdf.

[135] Sarah E Bohndiek et al. “Comparison of methods for estimating the conversion gain of CMOS active pixel sensors”. In: *IEEE Sensors Journal* 8.10 (2008), pp. 1734–1744. DOI: 10.1109/JSEN.2008.2004296.

[136] D Timmerman et al. “Space-separated quantum cutting with silicon nanocrystals for photovoltaic applications”. In: *Nature Photonics* 2.2 (2008), pp. 105–109. DOI: 10.1038/nphoton.2007.279.

[137] Donald L Snyder et al. “Compensation for readout noise in CCD images”. In: *JOSA A* 12.2 (1995), pp. 272–283. DOI: 10.1364/JOSAA.12.000272.

[138] Martin J Stevens et al. “Third-order antibunching from an imperfect single-photon source”. In: *Optics express* 22.3 (2014), pp. 3244–3260. DOI: 10.1364/OE.22.003244.

[139] Laura T Knoll et al. “Photon Statistics Modal Reconstruction by Detected and Undetected Light”. In: *Advanced Quantum Technologies* 6.8 (2023), p. 2300062. DOI: 10.1002/qute.202300062.

[140] C Bradac et al. “Observation and control of blinking nitrogen-vacancy centres in discrete nanodiamonds”. In: *Nature nanotechnology* 5.5 (2010), pp. 345–349. DOI: 10.1038/nnano.2010.56.

[141] Faraz A Inam et al. “Tracking emission rate dynamics of nitrogen vacancy centers in nanodiamonds”. In: *Applied Physics Letters* 102.25 (2013). DOI: 10.1063/1.4812711.

[142] Eugene Lukacs. “Applications of Faà di Bruno’s formula in mathematical statistics”. In: *The American Mathematical Monthly* 62.5 (1955), pp. 340–348. DOI: 10.1016/S0893-9659(03)90026-7.

[143] Djurdje Cvijović. “New identities for the partial Bell polynomials”. In: *Applied mathematics letters* 24.9 (2011), pp. 1544–1547. DOI: 10.1016/j.aml.2011.03.043.